

Portland State University

PDXScholar

Dissertations and Theses

Dissertations and Theses

8-6-2008

Nanostructured Aminophenylporphyrin Films for Use in Bulk Heterojunction and Inverse Dye-Sensitized TiO₂ Solar Cells

Michael George Walter
Portland State University

Follow this and additional works at: https://pdxscholar.library.pdx.edu/open_access_etds

 Part of the [Chemistry Commons](#)

Let us know how access to this document benefits you.

Recommended Citation

Walter, Michael George, "Nanostructured Aminophenylporphyrin Films for Use in Bulk Heterojunction and Inverse Dye-Sensitized TiO₂ Solar Cells" (2008). *Dissertations and Theses*. Paper 6032.
<https://doi.org/10.15760/etd.7875>

This Dissertation is brought to you for free and open access. It has been accepted for inclusion in Dissertations and Theses by an authorized administrator of PDXScholar. Please contact us if we can make this document more accessible: pdxscholar@pdx.edu.

NANOSTRUCTURED AMINOPHENYLPORPHYRIN FILMS FOR USE IN BULK
HETEROJUNCTION AND INVERSE DYE-SENSITIZED TiO₂ SOLAR CELLS

by

MICHAEL GEORGE WALTER

A dissertation submitted in partial fulfillment of the
requirements for the degree of

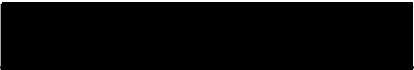
DOCTOR OF PHILOSOPHY
in
CHEMISTRY

Portland State University
2008

DISSERTATION APPROVAL

The abstract and dissertation of Michael George Walter for the Doctor of Philosophy in Chemistry were presented August 6, 2008, and accepted by the dissertation committee and the doctoral program.

COMMITTEE APPROVALS:



Carl C. Wamser, Chair




Mingdi Yan



Shankar B. Rananavare



Robert M. Strongin




Rolf Könenkamp



Erik Sanchez
Representative of the Office of Graduate Studies

DOCTORAL PROGRAM APPROVAL:



Kevin A. Reynolds, Director
Chemistry Ph.D. Program

ABSTRACT

An abstract of the dissertation of Michael George Walter for the Doctor of Philosophy in Chemistry presented August 6, 2008.

Title: Nanostructured Aminophenylporphyrin Films for Use in Bulk Heterojunction and Inverse Dye-sensitized TiO₂ Solar Cells

Conductive nanostructured films of poly-tetrakis-5,10,15,20-(4-aminophenyl)porphyrin (TAPP) can be grown electrochemically or through interfacial oxidative polymerization. The poly-TAPP nanomorphology is sensitive to the electrochemical solvent, potentiometric method, and the aminophenyl porphyrin monomer utilized. To elucidate the molecular structure of poly-TAPP and to correlate structures with proposed polymerization and conductivity mechanisms, reflectance FT-IR and spectroelectrochemistry were used to detect the presence and electroactivity of dihydrophenazine and phenazine polymer linkages formed during the polymerization.

Poly-TAPP nanofiber films were evaluated for use in a bulk heterojunction solar cell (with PCBM) and in an inverse dye-sensitized TiO₂ solar cell using the poly-TAPP nanoporous scaffold to control the interfacial contact region between donor (poly-TAPP) and acceptor (PCBM or TiO₂) phases. Poly-TAPP/PCBM cells exhibited short-circuit current densities of 140 $\mu\text{A}/\text{cm}^2$ and open-circuit potential

values up to 500 mV under simulated full-sun illumination. An inverse dye-sensitized solar cell was developed by incorporating TiO_2 into a dye-coated nanoporous poly-TAPP electrode. These cells demonstrated short-circuit current densities up to $46 \mu\text{A}/\text{cm}^2$ and open-circuit potential values of 232 mV under AM 1.5 solar illumination.

ACKNOWLEDGEMENTS

I would like to thank my thesis advisor, Dr. Carl C. Wamser for all his help, guidance, and direction with my research over the past six years. I'm very grateful for his relentless encouragement of all my research ideas and endeavors.

I want to thank past and present members of the Wamser group; Brian Kim, Keith James, Ian Hesselsweet, Kat Mazzio, and Alex Rudine, for all their help with this research, for good suggestions, hot coffee, and lots of laughs.

I would like to thank the members of my thesis committee, Dr. Mingdi Yan, Dr. Rolf Könenkamp, Dr. Eric Sanchez, Dr. Shankar Rananavare, and Dr. Robert Strongin for reading this thesis and for their helpful comments and suggestions.

I would like to thank the Portland State University Department of Chemistry for their support of my research and overall commitment to chemistry students at all levels.

My special thanks goes to Vanessa, Matilda, Mom & Dad, Beth, Sarah, and many others for their encouragement, support, and love during these years of my PhD work. I could not have done this without them!

TABLE OF CONTENTS

ACKNOWLEDGEMENTS.....	i
LIST OF TABLES.....	iv
LIST OF FIGURES.....	v
CHAPTER 1. INTRODUCTION.....	1
1.1 Introduction and Motivation.....	1
1.2 Types of Solar Cells.....	2
1.3 Operating Solar Cell Principles.....	4
1.4 Excitonic Solar Cells: Dye-sensitized TiO ₂ Solar Cells.....	13
1.5 Excitonic Solar Cells: Conjugated Polymer Solar Cells.....	17
1.6 The Use of Porphyrins for Optoelectronic Devices.....	19
1.7 The Electropolymerization of Tetraphenylporphyrins.....	22
1.8 Discovery of Nanostructured Poly-TAPP Films – Preliminary Results....	27
1.9 Nanostructured Poly-TAPP in Bulk Heterojunction and Inverse Dye- Sensitized Solar Cells – Basic Concepts.....	30
CHAPTER 2. EXPERIMENTAL.....	32
2.1 Materials Used.....	32
2.2 Electrochemically prepared Poly-TAPP Films.....	34
2.3 Chemically Prepared (Interfacial Oxidation) Poly-TAPP	35
2.4 Triaminophenyl monocarboxy TA ₃ CMPP and cis/trans-TA ₂ CM ₂ PP	36
2.5 Poly-TAPP – Excitonic Solar Cell Construction	40

CHAPTER 3. RESULTS AND DISCUSSION.....	44
3.1 Poly-TAPP Electrochemical Syntheses.....	44
3.2 Poly-TAPP Deposited from Pyridine:CH ₂ Cl ₂ Solutions	53
3.3 Surface Morphology of Poly-TAPP	58
3.4 The Effects of Dissolved Water on Poly-TAPP Films	65
3.5 The effects of porphyrin derivative on film growth	70
3.6 Chemically Interfacially Polymerized Poly-TAPP	73
3.7 Poly-TAPP Structure and Mechanisms for Growth and Conductivity.....	75
3.8 Conductivity in Poly-TAPP	82
3.9 Poly-TAPP Liquid Junction I ⁻ /I ₃ ⁻ Solar Cell	90
3.10 PCBM Incorporated Poly-TAPP Excitonic Solar Cell.....	96
3.11 Poly-TAPP Inverse TiO ₂ DSSC.....	108
CHAPTER 4. CONCLUSIONS.....	120
REFERENCES.....	124

LIST OF TABLES

Table I.	Infrared Frequencies (cm^{-1}) of poly-TAPP (both conductive and nonconductive forms) and TAPP monomer (solid) from reflectance FT-IR measurements.....	81
Table II.	Poly-TAPP films tested (*average data of 3 devices for each condition) under 100 mW/cm^2 using (I^-/I_3^-) liquid redox shuttle with all films synthesized from 15 electrochemical CV cycles with $\sim 5 \mu\text{M}$ device thickness from heat treated Surlyn film spacers.....	95
Table III.	Poly-TAPP - organic solar cell devices tested under 100 mW/cm^2 using PCBM incorporated from 2% chlorobenzene solutions and Al/LiF top electrode (*average data for three runs under each condition).....	104
Table IV.	Summary of inverse DSSC cells tested under AM 1.5 conditions (FTO poly-TAPP TCPP TiO_2 (Tyzor LA) TiO_2 nanoparticles Al).....	118

LIST OF FIGURES

Figure 1	P-N Junction crystalline silicon solar cell.....	5
Figure 2	Excitonic solar cell – (HOMO) – Highest occupied molecular orbital, (LUMO) – Lowest unoccupied molecular orbital.....	7
Figure 3	I/V Curve with energy level correlations at (a) short circuit conditions (I_{sc}), (b) at open circuit voltage conditions (V_{oc}), (c) reverse bias conditions with current flowing in the same direction as the photogenerated current, and (d) forward bias conditions where current is forced in the opposite direction.....	10
Figure 4	Dye-sensitized TiO_2 solar cell with (a) tetraphenylporphyrin, (b) indoline, (c) ruthenium bipyridyl dyes and efficiencies in DSSCs.....	14
Figure 5	Tetra[aryl]porphyrin structures used in oxidative electropolymerizations.....	23
Figure 6	Polyaniline conductive and nonconductive forms.....	25
Figure 7	Proposed oxidative polymerization of TAPP with diphenylamine, dihydrophenazine, and phenazine porphyrin linkages	26
Figure 8	SEM and AFM images of poly-TAPP electrochemically deposited from solution containing 15% pyridine in dichloromethane	28
Figure 9	Meso-substituted tetraphenylporphyrins investigated.....	31
Figure 10	(a) Poly-TAPP bulk heterojunction solar cell device with either PCBM or TiO_2 incorporated into the nanostructured polymer film, (b) Inverse DSSC with a TCPP coating and larger TiO_2 particle infiltration	41
Figure 11	(a) Cyclic voltammograms of the first 8 cycles of TAPP electropolymerization in CH_2Cl_2 with TBAP supporting electrolyte and cycling the electrode from 0 to 1.0 V vs. Ag/AgCl, (b) QCA measurements for the adsorbed mass for the first 8 CV cycles including blank scans in electrolyte solution with no TAPP added (baseline)....	44

Figure 12	(a) Poly-TAPP film from 3 CV scans cycled in 0.01 M TBAP/acetonitrile solution at 50 mV/s, (b) scan rate dependence of peak current (I_p) and peak potential separations (ΔE_p) on oxidation of poly-TAPP film silica TLC and centrifugal chromatography separation.....	47
Figure 13	(a) Surface coverage calculated from absorbance at 428 nm vs. cycle number for poly-TAPP films deposited from 1 – 15 electrochemical cycles with linear fit, (b) absorption spectra for 1 and 15 CV cycles....	51
Figure 14	(a) EQCM – chronocoulometry of poly-TAPP deposition at 0.4 V vs. Ag/AgNO ₃ from 0.15 mM TAPP, 0.01 M TBAP, (b) UV-vis spectra of deposited film after 50 & 75 s of fixed potentiometry electropolymerization 3-2 cis-TC ₂ N ₂ PP spectra in EtOH and extinction coefficient (Soret band).....	52
Figure 15	(a) Cyclic voltammogram of the first three cycles of TAPP electropolymerization under conditions using 95:5 (v:v) dichloromethane and pyridine, (b) combined CV (current, solid line) and EQCM (mass, dotted line) data for the first two cycles of electropolymerization of TAPP under standard conditions; the solid vertical lines show the 30 s constant potential delay at +0.7 V; the dashed vertical line shows the end of the first scan.....	54
Figure 16	CV cycles for the 1 st and 15 th electrochemical cycle for poly-TAPP electropolymerization using 95:5 (v:v) pyridine: dichloromethane	55
Figure 17	(a) EQCM data for 15 electrochemical cycles for poly-TAPP electropolymerization with 30 s vertex delay, (b) Data for 30 cycles with no vertex delay.....	56
Figure 18	(a) Electronic absorption spectra of poly-TAPP deposited on FTO from 1-15 cycles from pyridine-containing solution, (b) Surface coverage (Γ) vs. CV cycle number for poly-TAPP deposited from solutions with and without pyridine.....	58
Figure 19	SEM images of poly-TAPP films electropolymerized on FTO electrodes using cyclic voltammetry in a solution of 95:5 (v:v) dichloromethane:pyridine, (a) 3 CV scans, 0% pyridine, (b) 3 CV scans, 5% pyridine, (c) 3 CV scans, 15% pyridine, (d) 15 CV scans, 5% pyridine, (inset) film thickness measurement (528 nm) from cross section of poly-TAPP film.....	59

Figure 20	Poly-TAPP film deposited with 15 scans under conditions identical to Figure 19 b, d: (a) cross-section, (b) mechanically scraped section, (c) 15 CV scans, 5% pyridine where film has grown over a nonconductive surface scratch, (d) films deposited using 3 cyclic voltammetry scans at higher magnification.....	62
Figure 21	AFM images of poly-TAPP film deposited from (a) dichloromethane without pyridine, (b) 95:5 (v:v) dichloromethane:pyridine, with (c) cross-sectional analysis.....	63
Figure 22	Poly-TAPP from fresh solution (a) after 1 hour, (b) film deposited after 24 hours, (c) poly-TAPP from solution with lutidine after 1 hour, (d) after 24 hours.....	64
Figure 23	EQCM for poly-TAPP depositions with trace amounts of dissolved water: 1%, < 0.1%, and anhydrous (rigorously dried).....	66
Figure 24	SEM images of poly-TAPP films electrochemically deposited after 15 CV cycles in 95:5 dichloromethane:pyridine, (a) anhydrous conditions, (b) < 0.1% H ₂ O, (c) ~1% H ₂ O.....	66
Figure 25	Poly-TAPP films deposited from 15 CV cycles with water saturated dichloromethane ~1%.....	68
Figure 26	Poly-TAPP film deposited from 15 CV cycles in CH ₂ Cl ₂ with: (a) 5% acetonitrile, (b) ≤ 0.1% water.....	69
Figure 27	Poly-TAPP grown from dichloromethane solutions containing ≤ 0.1% dissolved water and anhydrous conditions.....	70
Figure 28	Surface features observed for electropolymerized films obtained from TA ₃ CMPP and trans-TA ₂ CM ₂ PP. The cis-TA ₂ CM ₂ PP derivative did not deposit any substantial film and exhibited one irreversible oxidation which was not repeated after the first CV cycle. All images from films were produced from CH ₂ Cl ₂ with ≤ 0.1% H ₂ O.....	72
Figure 29	(a) Interfacial poly-TAPP polymerization over 12 hrs reaction time, (b) SEM image of nanofibrous poly-TAPP film, (c) larger “clumps” of harvested porphyrin polymer films within which nanofibrous features were discovered, (d) concentration of TAPP in solution over time with first order decay fit (dotted line).....	74
Figure 30	(a) Dihydrophenazine linked dimer, (b) phenazine linked dimer.....	76

Figure 31 (a)	Reflectance FT-IR spectra for evaporated TAPP onto FTO electrode and poly-TAPP from 100% dichloromethane electrochemical solutions (<i>o</i> – peaks attributable to dihydrophenazine).....	77
Figure 31 (b)	Figure 31. (b) Reflectance FT-IR spectra for evaporated TAPP and poly-TAPP from 95:5 dichloromethane and pyridine, (c) comparisons of both types of poly-TAPP films <i>x</i> – peaks attributable to phenazine <i>o</i> – peaks attributable to dihydrophenazine.....	78
Figure 32	Polyaniline bipolaron conduction mechanism.....	82
Figure 33	(a) Neutral dihydrophenazine TAPP dimer, (b) oxidized dimer ($2 e^-$) depicting new protonated phenazine linkage, (c) dimer resonance form with quinoid bipolaron form (highlighted bonds) and neutral diaminophenyl form, (d) bipolaron movement within dimer depicting the electron transfer and exchange.....	83
Figure 34	(a) Dihydrophenazine linked dimer with (CHARMM) minimized structure, (b) phenazine linked dimer, (c) fully oxidized ($-4 e^-$) dihydrophenazine dimer.....	86
Figure 35	(a) TAPP, neutral, mix of neutral and diprotonated, and diprotonated in CH_2Cl_2 , (b) structure of the charge transfer excited state diprotonated TAPP.....	87
Figure 36	(a) Reversible spectroelectrochemistry of poly-TAPP film at potentials -0.3 V to $+0.7$ V vs. $Ag/AgNO_3$, (b) UV-vis spectra of TAPP oxidized in DMSO with APS, (c) Cis and trans quinone structures of oxidized TAPP $^{+2}$	89
Figure 37	(a) Current-voltage characteristics of the poly-TAPP (15 CV scans, using 95:5 CH_2Cl_2 :pyridine) nanoporous electrochemical cell in the dark and under 100 mW/cm^2 illumination. Inset - log plot of data, (b) Energy diagram for the nanoporous solar cell with work function values for the contact FTO electrodes [151], I^-/I_3^- redox couple [152], and the HOMO/LUMO energy levels for the poly-TAPP film (estimated from those reported for TAPP [86]).....	91
Figure 38	(a) On/off photocurrent response of the poly-TAPP electrochemical solar cell under 100 mW/cm^2 illumination. (b) Current-voltage comparison of solar cells using electrochemically deposited poly-TAPP films (15 cycles) obtained from solutions with and without 5% pyridine in the electropolymerization solution.....	93

Figure 39	(a) Potential energy diagram of poly-TAPP incorporated with, (b) 1-(3-methoxycarbonyl)propyl-1-phenyl[6,6]C ₆₁ (PCBM), (c) Poly-TAPP – PCBM or TiO ₂ device geometry with (d) interfacial nanofibrous photoactive layer schematic, yellow poly-TAPP nanofibers with brown PCBM incorporation.....98
Figure 40	(a) AFM images of poly-TAPP deposited from 3 CV cycles onto an ITO electrode using 5% pyridine. Also shown is the AFM images of PCBM applied from a 2% wt. chlorobenzene solution to a blank ITO and to the top surface of a poly-TAPP electrode (both scale bars are 3 nm), (b) SEM cross-section of the poly-TAPP/PCBM organic solar cell with each layer identified99
Figure 41	(a) UV-vis spectra of poly-TAPP film, PCBM, and incorporated poly-TAPP/PCBM (b) Photoluminescence spectra of poly-TAPP film and poly-TAPP with PCBM.....101
Figure 42	(a) Poly-TAPP – PCBM film using a poly-TAPP film deposited from 3 CV cycles using solutions containing no pyridine in the electrochemical solvent, (b) film thickness variations, (c) poly-TAPP (3 CV cycles) using 5% pyridine in the electrochemical deposition, (d) photocurrent comparison between conditions from (a) and (c).....103
Figure 43	(a) Poly-TAPP, PCBM, and combination poly-TAPP – PCBM solar cells, (b) Current – voltage log plot curves in the dark and under illumination.....105
Figure 44	Incident to photon current efficiencies (IPCE %) for a poly-TAPP – PCBM solar cell constructed with electrochemically deposited poly-TAPP (3 CV cycles) and a drop cast film of PCBM ~ 200 nm. Also shown are the absorption spectra of PCBM and poly-TAPP.....107
Figure 45	(a) Steps involved in the photoinduced charge separation, using a TCCPP dye layer with holes migrating in the poly-TAPP layer and electrons migrating through the TiO ₂ layer, (b) Energy level diagram with the relative band energies of the various components of a porphyrin inverse DSSC.....108
Figure 46	Preparation of TCCPP and surface reaction with poly-TAPP.....110
Figure 47	Poly-TAPP film absorbance spectra for the surface derivatization of poly-TAPP (synthesized from three electrochemical cycles) with TCCPP after 6 hr reaction.....111

Figure 48	(a) Hydrolyzed TiO_2 coating from two $\text{Ti}(\text{O-Pr})_4$ precursor solution coatings, (b) ten precursor solution coatings.....	112
Figure 49	(a) Hydrolysis of Tyzor LA on a poly-TAPP electrode using a 0.05 M Tyzor LA solution at pH 2.1 after five minutes (onset of solution turning cloudy), (b) same conditions, higher magnification, (c) poly-TAPP electrode soaked for 15 minutes, (d) 30 minutes (~500 nm thick film – cracks reveal FTO confirmed by EDX).....	114
Figure 50	(a) Thin TiO_2 coated poly-TAPP from Tyzor LA solution, (b) after coating with Solaronix paste, drying, and rinsing with water to remove excess TiO_2 particles, (c) XRD showing the films after Tyzor LA treatment and after TiO_2 nanoparticulate paste incorporation.....	116
Figure 51	(a) Current-voltage curve of inverse DSSC under illumination 100 mW/cm^2 , (b) photocurrent vs. time, (c) photocurrent vs. light intensity – measurements taken after 30 min of irradiation.....	117

Chapter 1. INTRODUCTION

1.1 Introduction and Motivation

The development and implementation of renewable, non-fossil fuel based energy sources has become a critical technological hurdle for the twenty-first century. Providing for the increasing energy demand, while at the same time reducing the CO₂ output burdening the environment requires new materials, and new ways of thinking about how energy is harvested and stored. In 2005, global energy usage rate totaled approximately 15 TW (1.5×10^{13} W, 5×10^{20} J/yr) with 87% being provided for through the use of fossil fuels [1]. It has been projected that global fossil fuel usage will increase the atmospheric CO₂ from the current concentration of 385 ppm (the highest it has been in the last 650,000 years) to 550 ppm by 2050 [2]. Although there remains some disagreement concerning the effects of an increasing atmospheric CO₂ concentration, our “experiment” with the global health of our environment will continue until non-carbon emitting sources of energy are established.

Energy harvested directly from sunlight using photovoltaic (PV) technology offers a very desirable approach to fulfill the need for clean energy with minimal environmental impact. Solar energy is a decentralized and inexhaustible natural resource with the magnitude of available solar energy striking the earth’s surface at any one instant equal to 400,000,000 power plants (500 MW plants) [3]. Our current global electricity demands could be met if this enormous energy source could be efficiently harvested and stored with as little as 0.1% of earth’s surface covered with

10% efficient solar cells. There are, no doubt, additional sustainable technologies besides photovoltaic electricity to help reduce reliance on fossil fuels including hydroelectric, wind, biomass, and geothermal. However, even these sources developed at maximum potential do not have the output capacity to provide the 28 terawatts of energy estimated to be required globally by 2050 [4]. Therefore, solar energy collection/conversion is the only long term solution for our energy needs.

Recently, there is evidence that the transformation to a solar energy powered society has begun with new commercial and academic efforts developing alternative, potentially inexpensive photovoltaic materials, processes, and devices. Current polycrystalline silicon solar cells, solar concentrators, and thin film technologies have furthered the growth of affordable solar cells while the creative incorporation of plastic substrates for traditional solar cells has driven costs down below the \$1/watt benchmark [3]. Academic efforts to develop more readily available and cheaply processable solar cells using concepts derived from natural photosynthesis have also contributed to the expansion of available PV technologies [5]. In order to make solar energy collection a truly viable, realistic, and environmentally friendly solution to global energy demands, furthering these developments and stimulating new technologies is paramount.

1.2 Types of Solar Cells

Solar cells composed of inorganic crystalline silicon have been the standard photovoltaic (PV) technology commercially available and used worldwide for almost

five decades accounting for 85% of the world's PV technology [6]. Silicon solar cells have a long history of research and development with the first PV devices having been fabricated at Bell Laboratories in 1953. Since then, new materials and manufacturing processes have slowly evolved with "generations" [7] of photovoltaic devices introduced to either reduce production cost or increase solar-to-power conversion efficiency.

The first generation of PV technologies is based on single or polycrystalline silicon devices manufactured using wafer technology. Although manufacturing costs associated with silicon solar cells have remained high, increased production rate has allowed current technology costs to become significantly reduced from \$22/W in 1980 to \$4/W in 2000 [7]. This still falls short of the U.S. Department of Energy's photovoltaic cost goal of \$0.33/W by the year 2015 [8]. The second generation of solar cells comprises thin film technologies which use materials such as amorphous Si, CdS/CdTe, and Cu(In,Ga)Se₂; these have allowed researchers to build efficient devices without the need of costly silicon wafer substrates. Materials used in the second generation can be fabricated using sputtering and physical/plasma-enhanced chemical vapor deposition techniques which are relatively inexpensive compared to the costly and wasteful milling techniques used for silicon solar cells. One commercial venture which has brought the manufacturing cost down to ~\$1.00/watt is Nanosolar which began full scale manufacturing and shipping in the fall of 2007. Nanosolar has developed a printable Cu(In,Ga)Se₂ nanocrystalline ink which can produce devices with 14.6% efficiency [9].

Third generation solar cells encompass a relatively new field of photovoltaics which use a wide range of materials and device architectures. This generation includes dye-sensitized solar cells, organic polymer/small molecule solar cells, and hybrid nanocrystalline solar cells. Most notable is the dye-sensitized TiO_2 solar cell introduced by Michael Grätzel and Brian O'Regan at the École Polytechnique Fédérale de Lausanne in Switzerland [10], and the organic bulk-heterojunction solar cell first introduced by Heeger et al. [11] and further developed by Sariciftci's group in Linz, Austria [12]. Third generation devices seek to achieve moderate efficiencies (10-15%) but with lowered production costs using well-established techniques for printing thin films on organic substrates, roll to roll processing, or nanostructuring the device to precise dimensions. Organic and hybrid organic/inorganic solar cells benefit from the material's high light absorptivity allowing devices to be less than 1 μm thick. Dye-sensitized TiO_2 solar cells are thicker ($\sim 12 \mu\text{m}$), but require only a monolayer of dye coated onto a high surface area nanocrystalline surface. These devices offer the possibilities of devices with up to 11% efficiency with production costs one fifth that of conventional silicon based PV technologies [7].

1.3 Operating Solar Cell Principles

The primary differences between the first/second generation conventional PV devices and the third generation organic/hybrid nanocrystalline PV devices are the photoinduced charge transport mechanisms operating within each device. The widely used conventional inorganic crystalline silicon PV devices are based upon the silicon

p-n junction whereby two crystalline silicon materials with different chemical dopants are brought together to form an energetically unstable junction. One side of the silicon junction is p-doped with a material like boron that introduces electron deficiency while the other side is n-doped with a material like phosphorous which introduces excess electrons. (Figure 1) At the interface of these two materials is a depletion region formed when free electrons of the n-doped side migrate to the p-doped side. This depletion region at the interface forms an internal electric field responsible for the charge directionality and movement within the PV device. Upon illumination,

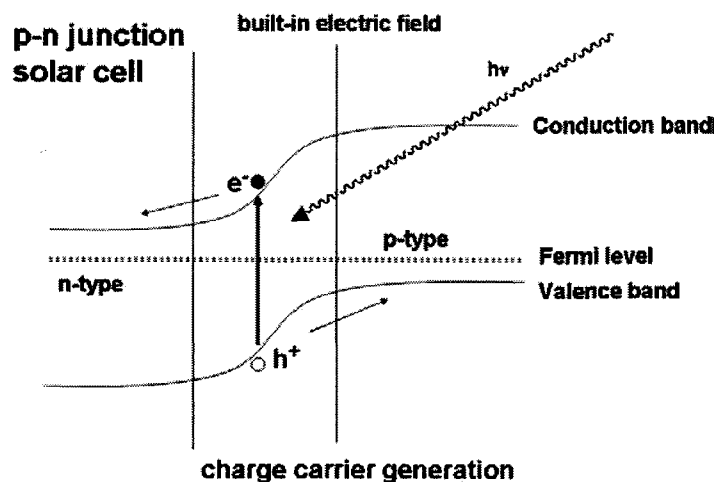


Figure 1. P-N junction crystalline silicon solar cell

excited states dissociate into electrons and holes, each of which move freely within the crystalline silicon lattice. The internal electric field created by the depletion region directs electrons in the p-doped side and holes in the n-doped side towards the

interface and then into the opposite side of the junction. An electric field is necessary for efficient charge carrier separation and the observed photovoltage, while current densities are a result of both drift due to the electric field and diffusion due to the carrier concentration [13]. An important principle separating conventional solar cells from organic or hybrid inorganic/organic devices is that the photogeneration is distributed throughout the device (within the photoactive region). As will be seen with third generation excitonic solar cells, localized photogenerated charge carrier concentration is greatest closer to the interface of the p-type/n-type materials.

In third generation devices (organic/dye-sensitized solar cells), a different photogenerated charge carrier mechanism has been observed. Because of the low dielectric of the organic/inorganic materials used, electrons and holes generated under illumination are bound together by coulombic attraction. These electron/hole pairs are called excitons and although mobile, have limited diffusion lengths before they recombine. Excitons typically have binding energies of $\sim 0.3 - 0.4$ eV and can only be dissociated at the interface of two materials whose energy level offset is greater than the binding energy of the electron/hole exciton [14]. These devices have been coined as “excitonic” solar cells because the excitons generated and dissociated give rise to the observed photovoltaic characteristics [15].

In excitonic solar cells two semiconducting materials with offset energy levels are brought together to form a donor (p-type)/acceptor (n-type) interface where dissociation and hence electron transfer can occur (neglecting interfacial band bending

and assuming ohmic metallic contacts). (Figure 2) Upon light absorption, an exciton

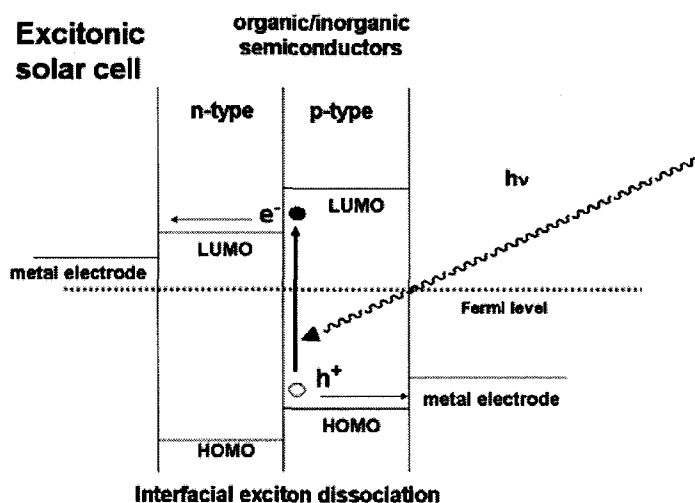


Figure 2. Excitonic solar cell – (HOMO) – Highest occupied molecular orbital, (LUMO) – Lowest unoccupied molecular orbital

is formed consisting of a bound electron/hole pair capable of moving within the n-type or p-type semiconductor phase. Depending on the nature of the excitonic solar cell device, the optical absorbance, and energy levels, excitons can be formed in either phase; however, dissociation occurs primarily at an interface of the two materials. Unfortunately, because of the high degree of disorder present in many organic solids, excitons and free charge carriers are limited by low mobility associated with hopping mechanisms between disordered localized states. This transport significantly differs from that observed in conventional silicon materials where greater charge transport occurs within the band structure of a highly crystalline silicon material. The highest hole (μ_h) and electron (μ_e) mobilities reported for organic materials are typically on the

order of $15 \text{ cm}^2\text{V}^{-1}\text{s}^{-1}$ and $0.1 \text{ cm}^2\text{V}^{-1}\text{s}^{-1}$ respectively while crystalline silicon exhibits free charge carrier mobility of $\mu_h = 450 \text{ cm}^2\text{V}^{-1}\text{s}^{-1}$ and $\mu_e = 1400 \text{ cm}^2\text{V}^{-1}\text{s}^{-1}$ [16].

There are other factors which can limit the overall efficiency of an excitonic solar cell device. Firstly, excitons are neutral (therefore unaffected by electric fields) and have a limited lifetime because of their low mobility within organic semiconductors. Exciton recombination typically occurs within a diffusion length between 5 - 15 nm in most organic semiconductors [15]. Therefore, excitons with the highest probability of contributing to the concentration of free charge carriers (and hence photocurrent) will be those generated closest to the n-type/p-type material interface. In addition, because dissociation occurs primarily at an interface, the highest concentration of free charge carriers (electrons in the n-type electron accepting phase and holes in the p-type electron donating phase) will be located in close proximity to the interface where excitons dissociate. It is therefore crucial that the interfacial characteristics of the materials used in excitonic devices are engineered to shorten the path an exciton needs to diffuse to an interface and then move the separated charges in opposite directions before they can recombine. An enormous amount of effort in designing nanostructured interfaces has commenced in recent years taking advantage of nanostructured metal oxide films [17], nanofibers of conjugated p-type polymeric materials [18], and methods to bring together the nanomaterials to form a nanoscale binary interpenetrating network.

To facilitate free charge carrier (electron/hole) movement away from the interface after exciton dissociation, typical devices use electrodes with offset work

functions. This does not limit the photovoltages observed from devices constructed with offset work function electrodes. It is the chemical potential of the two materials (electron donating and electron accepting) used in the device that give rise to the observed photopotential. Field effect drift and free charge carrier diffusion is the primary mechanism for charge movement within the device and is responsible for the observed photocurrent [19].

The changing energy levels of an excitonic solar cell containing donor and acceptor phases with offset HOMO/LUMO can be modeled by examining exciton movement with respect to the changing applied electric field. Device geometries typically are based on the metal-insulator-metal diode configuration where the photoactive materials (organic or a hybrid inorganic/organic) are sandwiched between two metal electrodes. Figure 3 depicts a simple model for these types of devices using Al and fluorine-doped tin oxide (FTO) contact electrodes which have differing work functions. Each stage in this model is then correlated to the representative current/voltage (I/V) curve of a bilayer organic solar cell device shown in the center. The standard (I/V) curve is used to measure the efficiency of a solar cell's ability to convert light energy into useful electrical work.

Figure 3a shows the short circuit conditions when no external potential is applied to the device. Due the asymmetrical work functions of the contact electrodes, the solar cell experiences an evenly distributed electric field across the device tilting the HOMO/LUMO levels towards the lower work function Al contact. In the dark, no current is flowing under these conditions due to the insulating properties of the

semiconductive materials. The dark I/V curve should therefore exhibit no current under zero applied voltage indicating a device whose materials contain no intrinsic charge carriers. However, under illumination excitons generated

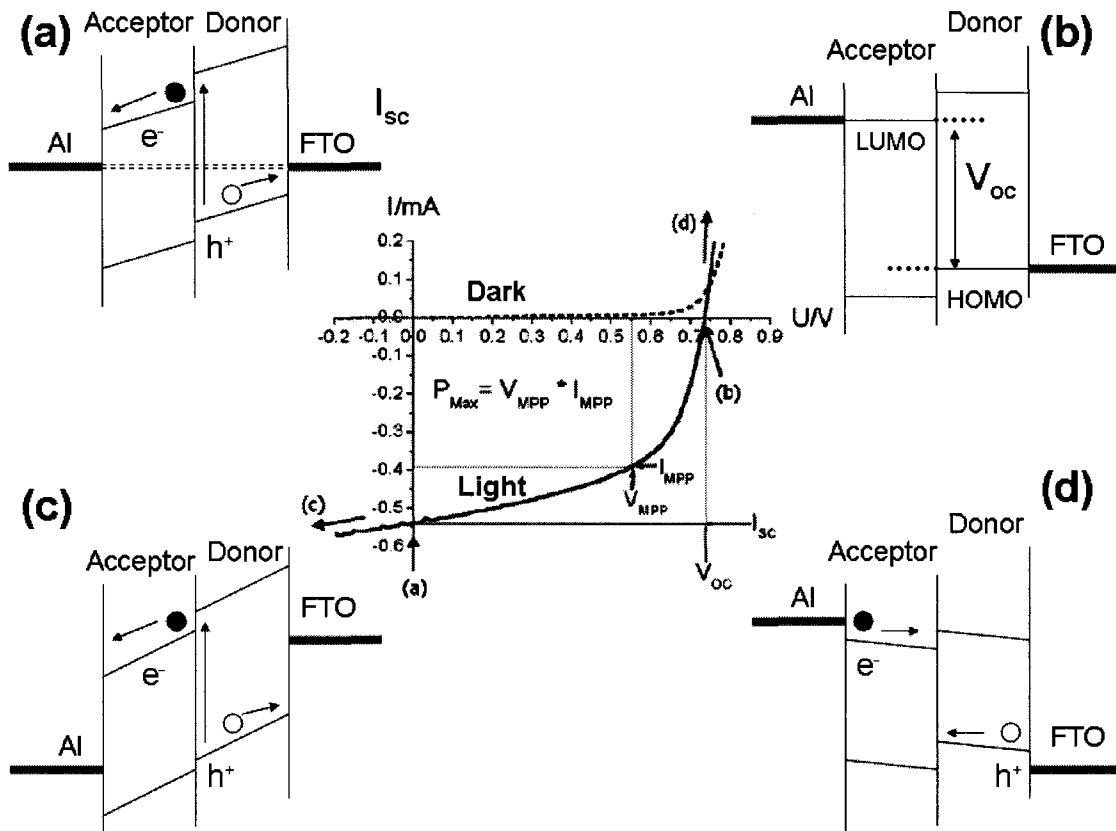


Figure 3. I/V Curve with energy level correlations at (a) short circuit conditions (I_{sc}), (b) at open circuit voltage conditions (V_{oc}), (c) reverse bias conditions with current flowing in the same direction as the photogenerated current, and (d) forward bias conditions where current is forced in the opposite direction

dissociate at the interface of the two materials and the electric field directs free charge carriers (holes and electrons) towards the Al (electrons) and FTO (holes) electrodes.

The HOMO/LUMO levels of the donor phase are lower in energy than the levels of acceptor phase encouraging exciton dissociation at the interface of two materials.

Figure 3b depicts conditions which mimic open circuit voltage conditions (V_{oc}) where the potential applied across the cell is cancelled by the internal electric field created/represented by the difference between the HOMO level of the donor material and LUMO of the acceptor material. In the dark, minimal current is flowing between the scenarios in Figure 3a and Figure 3b as a result of the applied forward bias. Under illumination however, current is flowing opposite the applied field until the electric potential created by the dissociation of excitons at the interface of the donor and acceptor phases is cancelled by the applied field. At this point, because free charge carriers experience no directional forces from an external electric field, excitons recombine and the net current is zero (V_{oc} conditions).

Figure 3c depicts a reverse bias applied past the short circuit conditions (under illumination) encouraging free charge carriers to move in the preferred direction of the photogenerated current. Figure 3d depicts a forward bias applied to the solar cell causing current to rapidly increase in magnitude opposing the normal operating solar cell direction. The large current increase is due to the asymmetric work functions of the metal electrodes causing electron injection from the lower work function material (Al) and hole injection into the device from the higher work function material (FTO). The main source of current is therefore electron/hole recombination and in some instances can result in a radiative recombination at the device interface. This can be

observed as electroluminescence in which case the device is responding as a light emitting diode.

To calculate the measured efficiencies from the various currents and voltages observed in I/V curves of the device under illumination, several factors are considered for determining solar cell device efficiencies. The product of the measured values of I_{sc} and V_{oc} represent the maximum theoretical power that the device can produce under illumination. The actual power produced is the maximum power point on the current/voltage curve representing the power output that has been reduced by internal series and parallel resistances in the solar cell. The maximum power (product of I_{mp} and V_{mp}) that can be delivered to an external load is compared to the I_{sc}/V_{oc} values through the ratio of their products called a “fill factor” which can quickly assess how well a device responds to a changing applied potential. (Equation 1)

$$FF = (P_{max}) / (I_{sc} \times V_{oc}) \quad (1)$$

A fill factor close to one indicates a device which has low resistive losses due to transport and recombination inherent both in the materials used, and cumulative engineering defects in the device. To measure the overall power conversion efficiency of the device ($\eta\%$), the maximum power output of the device is divided by the solar input irradiating the cell. (Equation 2)

$$\eta = P_{out}/P_{in} = (I_{sc} \times V_{oc} \times FF) / P_{light} \quad (2)$$

The solar irradiance used to irradiate PV devices frequently is measured and reported as having been illuminated under AM 1.5 “one sun” irradiance which

corresponds to approximately 100 mW/cm^2 . This is an average irradiance experienced through an air mass of 1.5 (the equivalent of 1.5 atmospheres in thickness), where the zenith angle of the sun is approximately 48.2° from being directly overhead [20]. The efficiencies of many excitonic solar cell devices have been certified at the National Renewable Energy Lab solar testing center in Golden, Colorado. Excitonic solar cell efficiencies have a wide range of reported values between 4% - 6% efficiency for organic/inorganic solar cells and up to 11% efficiency reported with the ruthenium dye-sensitized TiO_2 solar cell [13].

1.4 Excitonic Solar Cells: Dye-sensitized TiO_2 Solar Cells

The dye-sensitized solar cell, DSSC, also known as the “Grätzel” cell, was developed by Swiss scientist Michael Grätzel in the early 1990’s and is effective at producing large photocurrents (up to 20 mA/cm^2) and photopotentials (0.5-0.9 V) by using organic/organometallic synthetic dyes adsorbed onto highly porous titanium dioxide nanoparticles [21]. Taking advantage of the high surface area and wide bandgap of the titanium dioxide particles, electrical energy can be produced by the excitation of dye molecules and their subsequent donation of electrons into the conduction band of the TiO_2 . Dyes that give the highest short circuit photocurrents and open circuit photovoltages have typically been the bis(2,2’-bipyridyl-4,4’-dicarboxylate) ruthenium(II) dyes. These dyes absorb a broad range of visible light and when used in the TiO_2 system convert 11% of AM 1.5 solar radiation into electrical energy [22]. Ruthenium DSSC’s systems have approached the efficiencies

seen with conventional polycrystalline silicon photovoltaic cells. Figure 4 shows the operating features of a DSSC with dye adsorbed onto the surface of the TiO_2 particle and the incorporation of the redox I^-/I_3^- couple used to deliver electrons back to the oxidized dye. Several dye structures evaluated in DSSC's including their efficiencies are shown in Figure 4 [23].

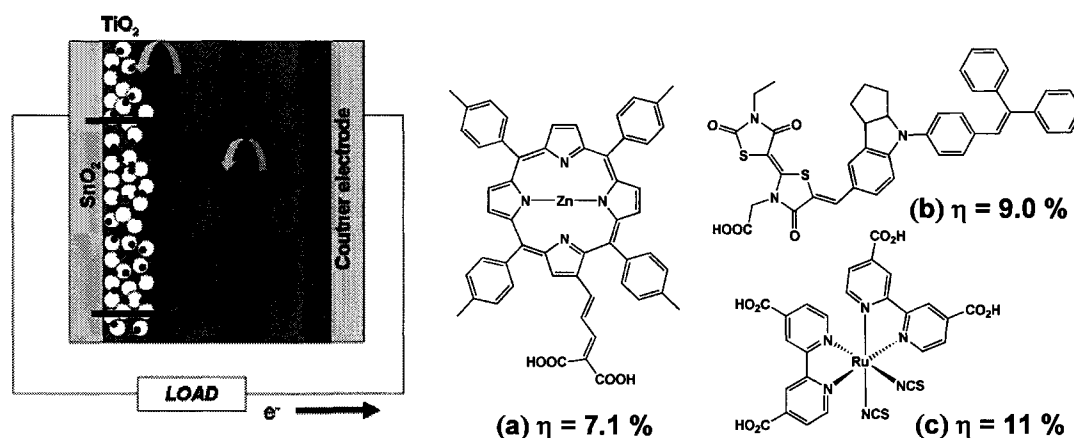


Figure 4. Dye-sensitized TiO_2 solar cell with (a) tetraphenylporphyrin, (b) indoline, (c) ruthenium bipyridyl dyes and their efficiencies in DSSCs

The limitation of the DSSC is the instability of the electrolytic solution (evaporation, sublimation of I_2 , etc.). Additional problems arise with the variation of temperatures at which the cell can operate. Under low temperatures lowered diffusion within the electrolytic solution and crystallization ultimately lead to a lower electrical efficiency. At high temperatures, evaporation of solvent and sublimation of I_2 complicates performance. Methods to improve the environmental stability of the reducing counter-electrode system by using solid electroactive polymer materials is

therefore of significant interest in this field. Much work has been devoted to replacing the liquid I^-/I_3^- redox couple electrolyte with a solid electroactive polymer such as polypyrrole, polyaniline, and polythiophene; however, efficiencies for solid state polymer/dye/ TiO_2 devices have remained low, around $\eta = 0.4 - 2\%$ [24-26]. Typical device preparation of these involves spin casting a solution of conjugated or conductive polymer to fill the nano-porous TiO_2 film. It is thought that the conductive polymer material in these devices does not provide high enough hole mobilities within the thick TiO_2 film which results in electron-hole recombination and current/power loss. Additionally, the shielding effect of electrons moving through the titania layer by the I_3^- redox counter ion may explain why higher efficiencies have yet to be achieved using conductive polymers in a DSSC [27].

The latest generation of DSSC's have been developed to include room temperature ionic liquids and gel electrolytes providing good efficiencies (8% and 6% respectively) coupled with the desirable environmental stability [28,29]. The most efficient solid state DSSC reported uses an electrolyte material containing iodine dissolved in a solvent-free eutectic melt of three ionic liquids which have demonstrated efficiencies as high as 8.2% with excellent long term stability [30]. The Grätzel group has also used a single molecule hole conductor (spiro-MeOTAD) which can be melted into the nano-porous film forming a solid state DSSC with overall efficiencies up to 4% in full sunlight [31]. Most versions quasi-solid-state solar cells still rely on I_3^- ion migration through the charge transfer medium to transport electrons to the oxidized dye molecules on the surface of the TiO_2 . This mechanism is what

differentiates the two basic approaches to solid state dye-sensitized TiO_2 solar cells. One relies upon the necessity of ion mobility and diffusion in the charge carrier region whereas the conductive polymer approach hopes to transport charges (holes) in a stationary, semicrystalline conductive material. Both accomplish this while retaining the same nano-particulate TiO_2 network that has been used with the typical liquid electrolyte DSSCs. The excitonic nature is maintained with the DSSC due to the photoactive monolayer of dye where excitons are generated but do not have to travel far before they are dissociated into holes and electrons. Holes are carried away by electrolyte while electrons are carried away by a TiO_2 nanoparticulate film. The nanoscale interpenetrating network is extremely important in the DSSC for efficient charge migration away from the interface due to the relatively thick active layer (5 – 10 μm).

Several groups have identified the need for more ordered nano-structures and device engineering if a truly efficient solid state polymer/metal oxide solar cell can be realized [32]. A more ordered structure would allow for shorter electron path lengths in the metal-oxide film, or better hole conduction in an ordered polymer film. Retaining the wide bandgap semiconductor TiO_2 remains important to the device structure because it is an inexpensive, well characterized nanomaterial with several synthetic deposition options and tuned opto-electronic properties [33,34]. PV cells developed using a high surface, highly structured titania layer and a polythiophene conductive polymer have exhibited efficiencies around 1.5% in AM 1.5 conditions [35]. This interpenetrating network allows for light harvesting at the interface of the

polythiophene/TiO₂ layer, with holes and electrons generated being shuttled away by the TiO₂ and polymer respectively. PV device like this still remain in the category of excitonic-like solar cells like that described by Gregg [15] because the photo-voltages and currents result from the excitation of a monolayer of dye to form an exciton which dissociates into free carriers at a dye/TiO₂ interface.

1.5 Excitonic Solar Cells: Conjugated Polymer Solar Cells

Since the discovery of photoinduced charge transfer from the excited state of poly[2-methoxy-5-(2'-ethylhexyloxy)-1,4-phenylene vinylene] (MEH-PPV) to Buckminsterfullerene (C₆₀), [36] there has been a huge upsurge in research devoted to finding new conjugated polymers incorporated with an electron acceptor like C₆₀ or its organic soluble derivative, 1-(3-methoxycarbonyl)propyl-1-phenyl-[6,6]-C₆₁ (PCBM) for use in organic solar cells. These devices are described as bulk heterojunction solar cells and are composed of a blend of conjugated polymer such as MEH-PPV, or polythiophene derivatives such as poly(3-hexylthiophene) (P3HT), and PCBM. The p-type conjugated polymer and the n-type electron accepting PCBM are dissolved together, and then deposited onto a conductive substrate using spin coating or doctor blading techniques. Upon drying, the two materials phase segregate, forming an interpenetrating network of donor and acceptor materials [37]. The blended materials in the films have an extremely large interfacial nanoscale contact region where photoinduced charge transfer can occur. Using commercially available conjugated polymer and fullerene materials, efficiencies of 5% or greater have been reached [38].

To improve the state-of-the-art bulk heterojunction solar cells, new low band gap polymers have been synthesized and tested which show improved absorbances and better HOMO/LUMO overlap with electron acceptor molecules such as PCBM [14,39,40]. By better matching of the LUMO of the acceptor to the LUMO of the donor, a theoretical device efficiency of 8% was predicted based solely on reducing the LUMO – LUMO energy offset from 1.1 eV to 0.5 eV (based on a P3HT – PCBM bulk heterojunction solar cell) [41]. There is an incredible potential for structurally tuning various polymers to control their optoelectronic characteristics. Other methods to increase efficiencies have been focused on adjusting the optical properties of the interfaces of the metallic contacts with the photoactive blend layer using sol-gel techniques to deposited TiO₂ layers designed to increase optical path length [42] or to invert the deposited sequence and use the TiO₂ as an electron selective contact [43].

Recently, significant contributions to increase the efficiency of polymer solar cells have been focused on characterizing the nanomorphology of blended organic polymer solar cells [44,45] and use nanostructured hole-conducting polymers to control device fabrication. Nanowires of poly(3-hexyl)thiophene were used by first depositing a nanowire mesh of fibers followed by PCBM incorporation [18]. These devices showed efficiencies as high as 3.0% with device thickness around 150 nm. By controlling the nanomorphology, it is assumed that a reproducible bicontinuous interfacial region could be achieved. These studies highlight how the same network achieved by randomly mixing the donor and acceptor phases can also be obtained

using simple aggregation techniques to control the nanostructure of the hole conductor. It is remarkable that the same trends observed for controlling the interfacial characteristics of DSSCs has carried over to polymer solar cell research. These focus on the control of interfacial geometries of the hole transport materials [46] to improve both the charge transport and the light absorbing properties, making the nanostructure an important focus for all varieties of excitonic solar cells.

1.6 The Use of Porphyrins for Optoelectronic Devices

Porphyrins continue to attract a great deal of attention for organic photonic devices because of their versatile molecular framework, varied optoelectronic properties, and strongly light absorbing centers [47-49]. Porphyrins are frequently the focus of artificial photosynthetic systems designed to generate electricity directly [50,51] or to drive the decomposition of water to H_2 and O_2 [52-54]. For example, porphyrins coupled to fullerenes have received significant attention due to their efficient electron transfer amenable for various photovoltaic applications [55-57]. The realization of using a porphyrin donor-acceptor molecular system in an organic/inorganic solar cell requires structural orientation that enhances exciton diffusion towards interfaces where charge separation takes place [58]. Innovative macromolecular architectures are needed for efficient charge mobility and collection within these devices. Self assembled porphyrin nanorods [59], interfacial films [60], and other multiporphyrin arrays [61] have been developed and used to address these structural requirements.

The introduction of porphyrins for use in excitonic solar cells has also become an important aspect of porphyrin dye research. Kay et al. first reported on the use of a Cu – chlorophyll derivative for a dye-sensitized TiO₂ solar cell and reported overall photocurrent efficiencies close to 3% [62]. Synthetic metallo and free base tetracarboxyphenylporphyrins have also been evaluated in a DSSC with carboxyphenyl groups serving to anchor the dye to the TiO₂ surface while providing a conjugated linker for efficient electron injection into the nanoparticulate film. Photocurrent efficiencies close to 45% have been achieved with power conversion efficiencies of 3% for tetracarboxyphenylporphyrins [63-65]. The Wamser group has developed a DSSC which used a porphyrin containing both aminophenyl and carboxyphenyl groups to photoelectrochemically grow polyaniline in-situ within the pores of the TiO₂ thereby eliminating the liquid electrolyte component, a major hurdle for the development of stable and efficient DSSC devices [24]. This device showed efficiencies as high as 0.8% using an aniline gel precursor which contained polyethylene oxide/LiClO₄ electrolyte and camphorsulfonic acid to initiate polymerization and to keep the growing polyaniline conductive. The highest efficiencies obtained using tetraphenylporphyrins in a DSSC is the recent report of a zinc containing tetraarylporphyrin malonic acid sensitizer by Campbell et al. which demonstrated a peak IPCE value of 63% and a resulting power conversion efficiency of 7.1% [66]. The high efficiencies were associated with increased electron injection efficiency obtained by constructing a coplanar porphyrin/linkage group incorporating substituents on the beta pyrrole position allowing for conjugation between the dye and

the carboxylate TiO_2 binding group.[67] These successful efforts to increase device efficiencies by tuning the dye structure suggest that a 10% efficient porphyrin DSSC is within reach. It is important to note that while the efficiencies reported for the standard ruthenium based dyes used in DSSCs have changed very little since development of DSSCs, there has been at the same time a threefold increase in the efficiencies of tetraphenyl porphyrin dyes.

Tetraphenyl porphyrins have also been used in excitonic solar cells which incorporate conjugated polymer bulk-heterojunction solar cells or in more elaborate supramolecular structures. One example is a device which organized fullerenes and porphyrins for efficient electron transfer through a polypeptide structure resulting in a power conversion efficiency of 1.6% [68]. Dastoor et al. reported on a solid-state porphyrin bulk heterojunction solar cell using a PCBM/MEH-PPV blend which performed with a 40% peak IPCE observed and improved broad band absorbance contribution to the IPCE from 60 to 80% by including a tetraphenyl porphyrin derivative in the polymer/fullerene blend [69]. Other solution processable devices which incorporate liquid crystalline porphyrins and chlorophyll structures indicate promising overall solar energy conversion efficiencies of 0.2% [70] and 1.48% [71] respectively. Many of these excitonic solar cell devices take advantage of materials which are widely used and optimized for efficient thin film organic solar cells such as polythiophene hole-conducting materials and electron-accepting fullerenes. As with many conjugated polymer systems, photoinduced electron transfer from porphyrins to fullerenes is also well studied area with a great deal of literature focused on structures

which have exhibited stabilized charge separated species and long-lived radical ion pairs [72]. In addition, it has been demonstrated that there exists a high binding affinity between the tetraphenyl porphyrin macrocycle and C_{60} structures allowing for the observation of efficient fluorescence quenching by fullerene moieties [73] and dyad linked structures [74]. Structures utilizing porphyrin/ C_{60} nanoclusters [75] and self-assembled monolayers [57] organized on ITO arrays have been reported to give high IPCE values up to 17% for extremely thin layered devices (~ 5 nm). While solar power conversion efficiencies are modest, the photoinduced electron transport occurring between porphyrin and fullerene is a highly efficient process which will require further nanostructure development and/or interfacial engineering to efficiently extract photogenerated free charge carriers.

1.7 The Electropolymerization of Tetraphenylporphyrins

Another important area of porphyrin research has been devoted to the oxidative electropolymerization and deposition of conductive polyporphyrin films. The electropolymerization of porphyrins offers the advantage of controlling the film deposition and conductivity through varying porphyrin monomer and/or potentiometric conditions [76]. Electrochemically deposited porphyrin films have been investigated for a wide variety of applications including electrocatalysis [77], as molecular sieves [78], fuel cell cathodes [79], and in photovoltaic donor/acceptor heterojunction devices [80]. The synthesis of these films occur under oxidative conditions leading to polymeric porphyrins linked together with electropolymerizable

substituents such as vinyl, amino/hydroxyphenyl, pyrrole, and thienyl [81,82].

(Figure 5) Electrochemically polymerized porphyrins can also contain metal cation

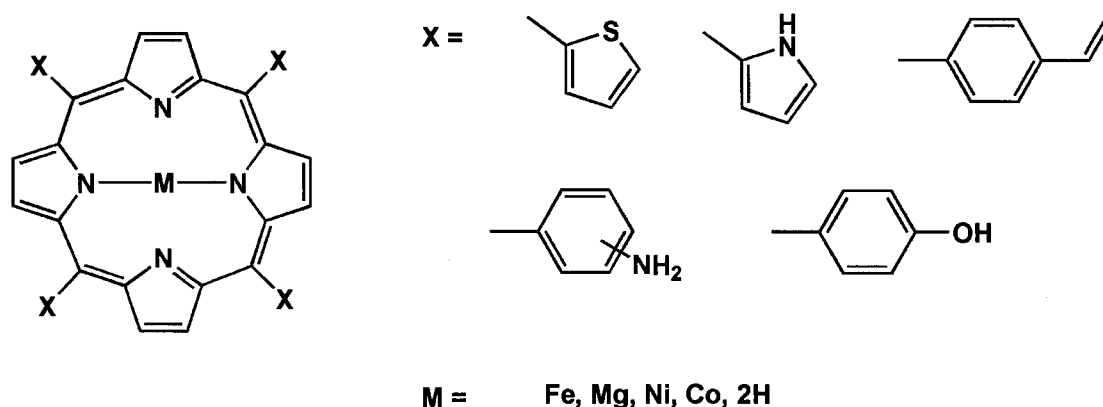


Figure 5. Tetra[aryl]porphyrin structures used in oxidative electropolymerizations

centers whose redox peaks are visible in the electrochemical polymerization window when they are not hidden by the peak currents of the porphyrin oxidation [83].

Although the electrochemical polymerization of tetraphenyl porphyrins is usually carried out using potentiostatic three-electrode techniques such as cyclic voltammetry or fixed potentiometry, alternative polymerization methods have been reported such as the use of photochemically or radiolytically generated radicals to initiate porphyrin polymerization [84].

In the case of tetraaminophenyl meso-substituted porphyrins, it has been found that oxidation occurs primarily on the aminophenyl substituents [85] leading to cation radical formation and coupling reactions as opposed to vinyl substituted porphyrins

(located on the beta pyrrole position) where the entire porphyrin macrocycle is oxidized followed by polymerization [83]. For aminophenylporphyrins, oxidation solely on the substituted aminophenyl groups is observed in the cyclic voltammogram with the first oxidation peak occurs at potentials 0.5 – 0.6 V more negative than is typically required for porphyrin ring oxidation. Because the oxidation affects only the aminophenyl substituent, porphyrin coupling between two cation radical species occurs at the ortho-aminophenyl position. The electrochemically generated polyporphyrin film exhibits similar absorbance spectra to that of the monomer in solution indicating that the π -conjugated porphyrin macrocycle has remained intact throughout the polymerization process [85,86]. Tetrasubstituted aminophenyl porphyrins can all undergo multielectron oxidation reactions and polymerize in a linear 1D or 2D fashion with possible crosslinking between polymer chains [87]. Metallo and non-metallo meso-substituted aminophenyl porphyrins containing both ortho, meta, and para substituted amino groups are found to electropolymerize under a wide range of conditions using both organic and aqueous electrolytic solutions [88-90].

The tetraaminophenyl porphyrin polymerization is closely related to aniline polymerization which can also be deposited electrochemically (or chemically) forming conductive films. (Figure 6) Polyaniline polymerization proceeds with aniline

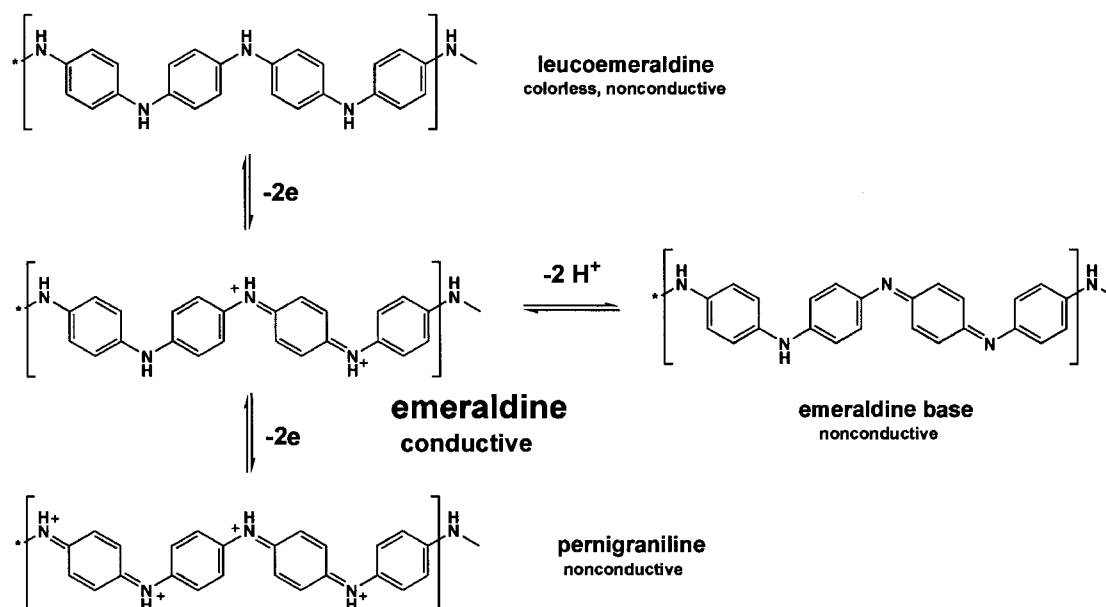


Figure 6. Polyaniline conductive and nonconductive forms

head-to-tail coupling to form a linear chain which is conductive upon oxidizing half the diphenylamine linking groups [91]. The emeraldine base must remain protonated to form the stable electroactive and conductive emeraldine polyaniline form [92,93]. Several studies have reported that polyaniline is not limited to the head-to-tail polymerization and that ortho-ortho aminophenyl coupling reactions under low acidity conditions can result in the formation of dihydrophenazine and phenazine linkages [94]. In the case of tetraaminophenyl porphyrins such as tetrakis-5,10,15,20-(4-aminophenyl)porphyrin (TAPP), it has been assumed that polymerization also proceeds (with head-to-head coupling) to form diphenylamine, dihydrophenazine, or phenazine linkages as shown in Figure 7 [95]. Each step in the proposed mechanism requires a $1 e^-$ electrochemical oxidation per TAPP monomer, coupling of the two

radical cation porphyrins followed by the loss of two protons. The extent to which the poly-TAPP film is oxidized to the completely aromatic phenazine moiety of the

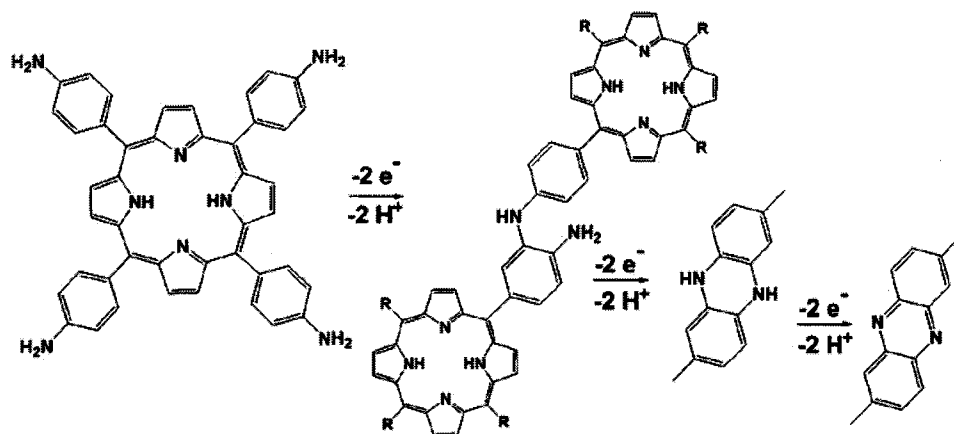


Figure 7. Proposed oxidative polymerization of TAPP with diphenylamine, dihydrophenazine, and phenazine porphyrin linkages

film in the final polymeric products have up to this point been undetermined, however several authors have noted the possible mix of all three linking group structures in the porphyrin polymer [87]. Polymerization of TAPP can proceed in a linear fashion (through trans 5,15-aminophenyl substituents) or through aminophenyl substituents located cis to one another on the porphyrin macrocycle (5,10 substituents). Crosslinking and interchain interactions is also highly probable with poly(4-amino phenyl)porphyrins through unreacted aminophenyl groups.

1.8 Discovery of Nanostructured Poly-TAPP Films – Preliminary Results

The oxidative electropolymerization of tetrakis-5,10,15,20-(4-amino phenyl)porphyrin (TAPP) was investigated to examine the redox characteristics and light absorbing properties of the thin polyporphyrin films. Typical solvent conditions used for electrochemically depositing poly-TAPP using cyclic voltammetry include dichloromethane and a supporting electrolyte, either tetrabutyl or tetraethylammonium perchlorate, organic soluble ammonium salts. It was often found that solutions of TAPP would appear yellowish/brown colored upon dissolution and several times began to precipitate out of the dichloromethane solution over time. The acid sensitivity and protonation of meso-substituted tetra(4-aminophenyl)porphyrins to form a hyperporphyrin structure has been well studied [96]. It was shown by Ojadi et al. that when protonated, porphyrins can exhibit a hyperporphyrin spectrum indicative of quinone structures formed between the two aminophenyl substituents with the porphyrin macrocycle corresponding an excited state charge transfer from the aminophenyl nitrogen to the center nitrogen in the porphyrin macrocycle ring [97,98].

Small amounts of dissolved HCl present in the dichloromethane solution protonated the TAPP as was observed using UV-vis absorbance of the solutions. At the concentrations used for electropolymerization, (0.1 – 1.0 mM) TAPP material gradually began to precipitate out of the dichloromethane solution presumably from protonated porphyrin aggregation [99]. It also has been noted recently that protonation of an electrochemically active aminophenyl porphyrin monomer was found to inhibit porphyrin polymer growth [100]. To avoid this situation and to

ensure TAPP remained nonprotonated, pyridine was added to the electrochemical solution (addition of pyridine immediately redissolved TAPP insoluble aggregates).

The effect of adding pyridine into the electrochemical solution on the electropolymerization for the first 10 CV cycles was negligible with standard increasing peak current oxidation envelopes with each cycle. However, electrode passivation and a gradual slowing of the porphyrin polymer growth were observed beyond 10 electrochemical cycles. In addition, the films deposited from solutions containing 5-15% pyridine appeared in general to have a more uniform porphyrin coating over the polyporphyrin coated area of the electrode than those electrodes obtained when only dichloromethane was used as solvent. The poly-TAPP films were examined using atomic force microscopy (AFM) to examine general morphological features of the film. Using AFM and confirming with SEM (Figure 8), it was discovered that after three electrochemical cycles using a 0.15 mM solution of TAPP (15% pyridine) a high surface area, nanofibrous poly-TAPP material was deposited.

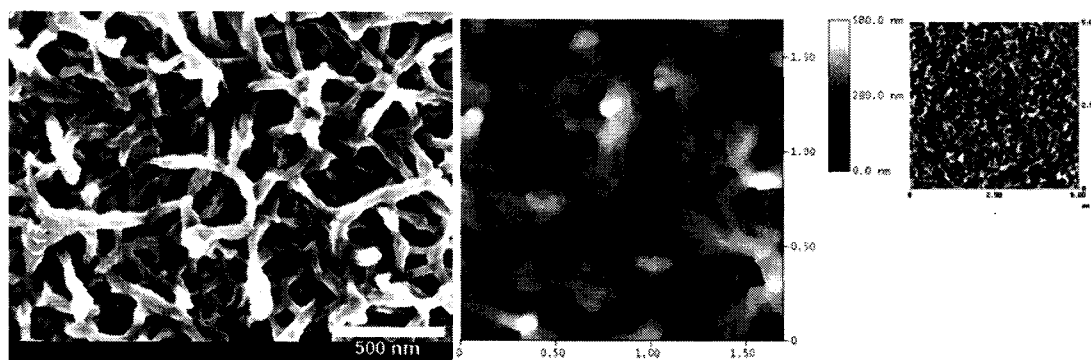


Figure 8. SEM and AFM images of poly-TAPP electrochemically deposited from solution containing 15% pyridine in dichloromethane

Although a few preliminary surface structure investigations of electrochemically deposited porphyrin films have been reported for a metallo diaminophenyl porphyrin [101] and other metalloporphyrins films [102,103], very little polyporphyrin surface nanomorphology data exist, and no known data exist for the surface morphology of nonmetallated poly(4-aminophenyl)porphyrins. Most reported studies indicate a generally smooth surface morphology with some indications of small randomly dispersed 25 nm islands of growth [104]. The electrochemically deposited poly-TAPP porphyrin nanofibers are believed to be the first observation for this type of porphyrin polymer surface morphology. Nanostructured porphyrin materials have been discovered with the use of monomer aggregates which form nanorods [105,106] and nanotubes [107] often due to the formation of J-aggregates in solution. Interestingly, there is a substantial body of literature which reports the syntheses of polyaniline nanofibers electrochemically or chemically through the use of controlling the precipitation and deposition kinetics [108-110]. The aminophenyl substituents on the porphyrin are believed to react in a similar fashion to the oxidative polymerization of aniline which leads to diphenylamine polymer linkages. The morphological surface features between the two systems are strikingly similar and structural correlations between the two systems can be made.

1.9 Nanostructured Poly-TAPP in Bulk Heterojunction and Inverse Dye-Sensitized Solar Cells – Basic Concepts

Excitonic solar cell device architectures were envisioned to take advantage of this nanostructured, highly light absorbing polymer thin film. Bulk heterojunction devices were developed which use the nanostructured poly-TAPP scaffold to dictate the interface between the porphyrin polymer and an appropriate electron acceptor material such as TiO_2 (inverse DSSC) or PCBM (traditional polymer bulk heterojunction electron acceptor material). Several methods were developed which were compatible with the porphyrin nanostructure by retaining the nanofibrous morphology while successfully incorporating an electron accepting material down into the porous poly-TAPP network.

This thesis presents the surface morphology investigations of oxidatively polymerized poly-TAPP nanostructured films and proposes polymerization and conduction mechanisms based upon electrochemical, spectroscopic, and surface morphological data. The majority of the films studied were polymerized using electrochemical methods, however it was discovered that films of poly-TAPP could also be synthesized at an organic/aqueous interface using the chemical oxidant ammonium persulfate (APS). Porphyrin materials utilized for electrochemical polymerization and surface morphology investigations included tetrakis-5,10,15,20-(4-aminophenyl)porphyrin (**TAPP**), 5,15-di(4-aminophenyl)-10,20-di(4-carbomethoxyphenyl)porphyrin (**trans - TA₂CM₂PP**), 5,10-di(4-aminophenyl)-15,20-di(4-carbomethoxyphenyl)porphyrin (**cis - TA₂CM₂PP**), 5,10,15-Tris(4-

aminophenyl)-20-(4-carbomethoxyphenyl) porphyrin (**TA₃CMPP**). Figure 9 shows the various tetraphenylporphyrin structures studied.

The photovoltaic characteristics of poly-TAPP incorporated into an excitonic solar cell device are also presented. The photovoltaic characteristics of the films by themselves were initially tested in an electrochemical solar cell containing a liquid

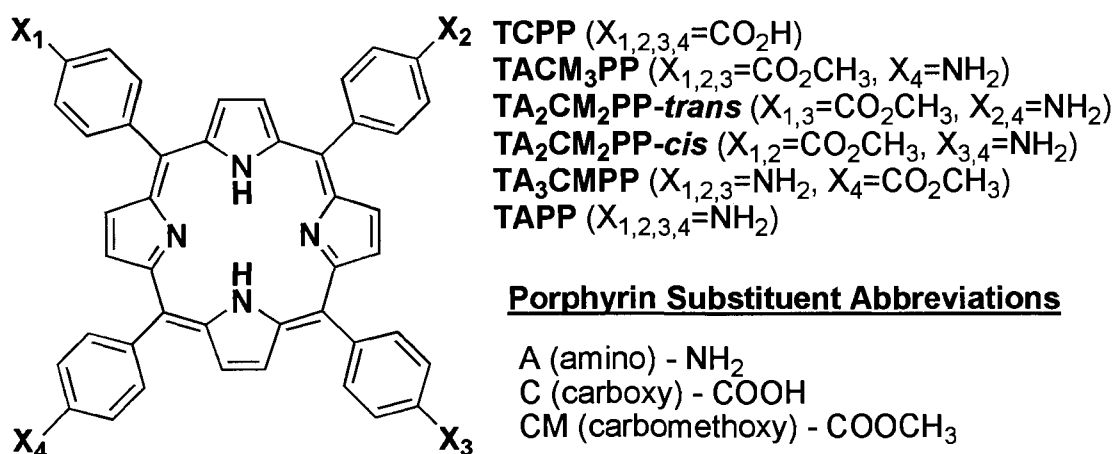


Figure 9. Meso-substituted tetraphenylporphyrins investigated

I^-/I_3^- redox couple used for DSSCs to probe photoactivity the nanostructured films.

Excitonic solar cell devices were then built using bulk heterojunction and an inverse dye-sensitized TiO_2 solar cell geometry. Both devices utilize the high surface area nanofiber poly-TAPP films as a scaffold to direct the interfacial structure between the poly-TAPP organic p-type semiconductor and an electron acceptor material either TiO_2 or 1-(3-methoxycarbonyl)propyl-1-phenyl[6,6] C_{60} (PCBM).

Chapter 2. EXPERIMENTAL

2.1 Materials Used

All materials (solvents, electrolytes, electrode materials) were obtained from TCI, Fisher, or Aldrich. Solvents used in electropolymerizations (dichloromethane, pyridine, lutidine, acetonitrile) were purchased as HPLC grade with less than 0.01% dissolved water. Tetrakis-5,10,15,20-(4-aminophenyl)porphyrin (TAPP) was obtained from TCI and used as received while other aminophenylporphyrin derivatives were obtained using previously reported conditions [111] (syntheses detailed below). Solvents were dried over activated 4Å molecular sieves and electrolytes TBAP/TBAH were recrystallized from methanol/water and dried in vacuo for 24+ hours at 60 °C. Platinum flag counter electrodes were used after heating to red hot in a flame, and rinsed in concentrated nitric acid, water, and then dichloromethane electrolyte solution immediately before use. Electrochemical cells were cleaned with concentrated KOH/IPA solution, rinsed with distilled water and stored in a drying oven overnight at 110 °C. FTO (fluorine-doped tin oxide) or ITO (indium doped tin oxide) electrodes obtained from Delta Technologies or Pilkington Glass were cleaned by sonication in dilute “Micro” electronic grade cleaner for 40 minutes followed by sonication in distilled water and 3:1 electronic grade acetone:IPA solution. After drying in an oven and cooling, electrodes were used immediately for electropolymerization and excitonic solar cell device construction.

Electropolymerizations were conducted using a Princeton Applied Research model 263 Potentiostat with E-Chem control with data software. Electrochemical quartz crystal micro-balance (EQCM) measurements were taken using single quartz crystal platinized electrodes (area = 0.2 cm^2 , 300 nm thick deposited Pt metal layer) in a Teflon mounting and electrochemical test tube cell mounted on the holder as the working electrode. A platinum wire was used as the counter electrode. A Princeton Applied Research Model QCA922 Quartz Crystal Analyzer was used with an operating frequency from 1 to 10 MHz (calibrated for a 9 MHz crystal). Data were analyzed using Win-Echem control and analysis software package. Typical scan ranges were 0.0 to 1.0 V vs. Ag/AgCl or -0.3 to 0.7 vs. Ag/AgNO₃ reference electrode using a 5.3 Hz current and 5.3 Hz voltage filter. Although an aqueous Ag/AgCl reference electrode was used for several of the organic solution electropolymerizations, its properties remained fairly stable throughout the investigations with reproducible data within each set of films polymerized. After each electropolymerization experiment, ferrocene was added and the potential was calibrated against the ferrocenium/ferrocene redox couple.

AFM images were obtained with a Digital Instruments Multimode atomic force microscope operating in tapping mode, and using silicon tipped cantilevers from Veeco Metrology Group (f_0 : 281-319 kHz, k : 20 – 80 N/m). Scan sizes and speeds were adjusted and are recorded on the AFM images taken. SEM micrographs were obtained using an FEI Sirion SEM operating at 2.0 – 5.0 kV accelerating voltage, and at a working distance of 5 mm. Transmission micrographs were obtained using a FEI

Tecnai F-20 TEM operating at 200 kV with films electrochemically grown directly on gold TEM grids (400 mesh, 3.0 mm).

Spectroelectrochemical measurements were made in a quartz cuvette cell in which a freshly deposited poly-TAPP film on FTO working was immersed in a TBAP/acetonitrile electrolyte solution (0.01 M) along with a Pt wire counter electrode and Ag/AgNO₃ reference. Absorbance characteristics of the films were measured in the UV-vis spectrophotometer (Shimadzu UV-260) made at 50 mV (vs. Ag/AgNO₃) increments. Reflectance FT-IR measurements were made at the University of Portland on a Thermo Nicolet 6700 FT-IR spectrometer operating in reflectance mode and evaluated using Grams 8.0 software. Photoactivity of the poly-TAPP films were measured by illuminating (100 mW/cm²) the active area (0.2 - 0.3 cm²) of a liquid electrochemical cell consisting of the electropolymerized poly-TAPP film, redox electrolyte (0.1 M KI, 0.05 M I₂ in a 80:20 (w:w) solution of ethylene carbonate and propylene carbonate), with graphite coated FTO glass counter electrode.

2.2 Electrochemically prepared Poly-TAPP Films

The following procedure was followed for poly-TAPP electropolymerization and deposition. Conditions that were varied include the concentrations of the aminophenyl porphyrin, aminophenylporphyrin derivative used, quaternary ammonium salt electrolyte used, the ratios of pyridine to dichloromethane, the concentrations of dissolved water in the primary solvents (pyridine and

dichloromethane), and the pyridine base derivative used. The electropolymerization of tetrakis-5,10,15,20-(4-aminophenyl)porphyrin (TAPP) is carried out on a fluorine-doped SnO_2 glass electrode (FTO) in a three-probe electrochemical cell using a 1 cm^2 Pt foil counter electrode and Ag/AgNO₃ reference electrode. The electropolymerization carried out for EQCM measurements was conducted in a QA-CL4 well type quartz crystal holder using a 0.2 cm^2 platinized quartz crystal working electrode and a platinum wire coil counter electrode. Typical solutions were prepared with 0.15 mM TAPP used as received from TCI America with 10 mM tetrabutylammonium perchlorate (TBAP) as supporting electrolyte in a 95:5 or 85:15 (v:v) dichloromethane:pyridine deaerated solution (all solutions were purged with argon for 20 minutes prior to electrodeposition). A combination of cyclic voltammetry (-0.3 to +0.7 V vs. Ag/AgNO₃) and fixed potentiometry is used with a 30 s vertex delay at +0.7 V within each cycle. The resultant polyporphyrin coated electrodes were rinsed with dichloromethane and pyridine solution and 2-propanol then dried under nitrogen. Films were used immediately for UV-vis, SEM, reflectance FT-IR, and AFM analyses.

2.3 Chemically Prepared (Interfacial Oxidation) Poly-TAPP

Poly-TAPP was interfacially polymerized by layering an aqueous solution of ammonium persulfate ($(\text{NH}_4)_2\text{S}_2\text{O}_8$ (3.4 mM) on top of a solution of TAPP in dichloromethane (0.15 mM). The solution was allowed to react in a 20 mL sample vial over 12 hrs. after which a thick black film formed at the interface leaving minimal

TAPP dissolved in the dichloromethane solution. The films were harvested using an FTO conductive electrode to initially break through the side of the film followed by scooping them out of the two solutions with the side of the film exposed to the aqueous phase facing up. The films adhered well to both FTO conductive electrodes and glass microscope slides. Films were floated on distilled water and then were rinsed with dichloromethane and acetone. Films were stable and exhibited no discoloration under ambient conditions over a 1 year period of storage.

2.4 Triaminophenyl monocarboxy TA₃CMPP and cis/trans-TA₂CM₂PP

Triaminophenyl monocarboxy porphyrin (TA₃CMPP) and the cis-TA₂CM₂PP were accessed using a partial transformation route previously described [111], involving the synthesis of a mixture of amino/carbomethoxyphenyl porphyrins starting with TCPP, partially transforming the carboxy groups to amines. Workup involves the separation of the six statistical products using preparative TLC plates.

Mixed substituent (4-amino/carboxyphenyl) porphyrins. A solution of tetrakis(4-carboxyphenyl)porphyrin (0.52 g, 0.658 mmol) and 39 g of polyphosphoric acid was warmed to 100°C. To this, 2 equivalents of NH₂OH·HCl (0.108 g, 1.56 mmol) was added and the mixture was slowly heated to 160°C over 3 h. Upon cooling to room temperature, conc. H₂SO₄ (10 mL) and CH₃OH (80 mL) were added and heated to reflux for 36 h. After the addition, the reaction mixture was neutralized with 1 M NH₄OH to a pH of 5.5. The dark porphyrin solution was extracted with chloroform (~1 L), washed with water, and dried over Na₂SO₄. The solution was

evaporated to dryness and dried in vacuo overnight affording a dark purple solid (0.48 g, 96% total yield). Silica TLC indicated six porphyrin products eluting with 4:1 - CH₂Cl₂ : ethyl acetate and 2 drops of triethylamine. The amino/ester porphyrins were isolated as described below, then hydrolyzed in base to give good yields.

5-(4-Aminophenyl)-10,15,20-tris(4-carbomethoxyphenyl)porphyrin

(TACM₃PP). Using a preparative silica TLC plate, 0.05 g of the product mixture was applied and eluted with (4:1) CH₂Cl₂ : ethyl acetate (2 drops Et₃N) collecting the second band (*R_f* = 0.68) as TACM₃PP, 0.007 g (13% of the original mix). UV-vis (THF): λ_{max}, nm (log ε) 420 (5.13), 516 (3.91), 552 (3.78), 595 (3.54), 648 (3.40). ¹H NMR (500 MHz; CDCl₃; Me₄Si). δ_H, ppm -2.79 (2H, s, pyrrole-NH), 3.64 (2H, s, -NH₂), 4.11 (9H, s, -CO₂CH₃), 6.89 (2H, d, *J* = 8.1, Ph-amino), 7.93 (2H, d, *J* = 8.1, Ph-amino), 8.29 (6H, d, *J* = 8.1, Ph-carbomethoxy), 8.44 (6H, d, *J* = 8.1, Ph-carbomethoxy), 8.78 (6H, bs, pyrrole-H), 8.94 (2H, bs, pyrrole-H). MS (ES): *m/z* 804.47 ([*M* + *H*]⁺ calcd. for [C₅₀H₃₈N₅O₆] 804.27).

5,10-Di(4-aminophenyl)-15,20-di(4-carbomethoxyphenyl)porphyrin (*cis* -

TA₂CM₂PP). Using a preparative silica TLC plate, 0.05 g of the product mixture was applied and eluted with (4:1) CH₂Cl₂ : ethyl acetate (2 drops Et₃N) collecting the fourth band (*R_f* = 0.40) as *cis*-TA₂CM₂PP, 0.018 (36% of the original mix). UV-vis (THF): λ_{max}, nm (log ε) 420 (5.04), 517 (3.90), 557 (3.81), 594 (3.54), 651 (3.41). ¹H NMR (500 MHz; CDCl₃; Me₄Si). δ_H, ppm -2.75 (2H, s, pyrrole-NH), 3.65 (4H, s, -NH₂), 4.11 (6H, s, -CO₂CH₃), 7.07 (4H, d, *J* = 8.3, Ph-amino) 7.99 (4H, d, *J* = 8.3, Ph-amino), 8.29 (4H, d, *J* = 8.2, Ph-carbomethoxy), 8.43 (4H, d, *J* = 8.2, Ph-

carbomethoxy), 8.76 (2H, d, $J = 4.8$, pyrrole-H), 8.78 (2H, s, pyrrole-H), 8.94 (2H, s, pyrrole-H), 8.95 (2H, d, $J = 4.8$, pyrrole-H). MS (ES): m/z 761.47 ($[M + H]^+$ calcd. for $[C_{48}H_{37}N_6O_4]$ 761.28).

5,15-Di(4-aminophenyl)-10,20-di(4-carbomethoxyphenyl)porphyrin (*trans* - TA_2CM_2PP). Using a preparative silica TLC plate, 0.05 g of the product mixture was applied and eluted with (4:1) CH_2Cl_2 : ethyl acetate (2 drops Et_3N) collecting the third band ($R_f = 0.48$) as *trans*- TA_2CM_2PP , 0.006 g (12% of the original mix). UV-vis (THF): λ_{max} , nm (log ϵ) 422 (4.91), 518 (3.72), 557 (3.64), 593 (3.30), 652 (3.26). 1H NMR (500 MHz; $CDCl_3$; Me_4Si). δ_H , ppm -2.75 (2H, s, pyrrole-NH), 3.65 (4H, s, - NH_2), 4.10 (6H, s, $-CO_2CH_3$), 7.03 (4H, d, $J = 7.7$, Ph-amino) 7.97 (4H, d, $J = 7.8$, Ph-amino), 8.29 (4H, d, $J = 7.9$, Ph-carbomethoxy), 8.43 (4H, d, $J = 7.9$, Ph-carbomethoxy), 8.77 (4H, d, $J = 4.0$, pyrrole-H), 8.94 (4H, d, $J = 4.0$, pyrrole-H). MS (ES): m/z 761.47 ($[M + H]^+$ calcd. for $[C_{48}H_{37}N_6O_4]$ 761.28).

Although accessing the *trans*- TA_2C_2PP isomer for use in electrochemical polymerization could be afforded by the method outlined above, a straightforward route was gained using a [2+2] condensation of a dipyrromethane with an additional aromatic aldehyde in CH_2Cl_2 with TFA as catalyst followed by oxidation with DDQ to the porphyrin structure.[112] Using one of the several methods already reported, [113,114] synthesis of the 4-nitrophenyldipyrromethane was straightforward, yielding a stable product, which could be purified using standard flash chromatography.

5,15-Di(4-carbomethoxyphenyl)-10,20-di(4-nitrophenyl)porphyrin (*trans* - TCM_2N_2PP). A sample of TCM_2N_2PP was obtained from the reaction of 4-

carbomethoxybenzaldehyde (0.635 g, 3.87 mmol) with *bis*-4-nitrophenyl dipyrromethane (1.03 g, 3.87 mmol) [113] which afforded a purple solid (0.3 g, 21%). ^1H NMR (500 MHz; CDCl_3 ; Me_4Si). δ_{H} ppm -2.83 (2H, s, pyrrole-NH), 4.12 (6H, s, - CO_2CH_3), 8.30 (4H, d, $J = 8.2$, Ph-nitro), 8.40 (4H, d, $J = 8.6$, Ph-carbomethoxy), 8.47 (4H, d, $J = 8.2$, Ph-nitro), 8.66 (4H, d, $J = 8.6$, Ph-carbomethoxy), 8.79 (4H, d, $J = 4.4$, pyrrole-H), 8.86 (4H, d, $J = 4.4$, pyrrole-H). MS (ES): m/z 821.45 ($[\text{M} + \text{H}]^+$ calcd. for $[\text{C}_{48}\text{H}_{33}\text{N}_6\text{O}_8]$ 821.81).

5,15-Di(4-aminophenyl)-10,20-di(4-carboxyphenyl)porphyrin (*trans* - $\text{TA}_2\text{C}_2\text{PP}$). A sample of $\text{TCM}_2\text{N}_2\text{PP}$ (0.1 g, 0.07 mmol) was dissolved in 37% HCl (20 mL). To this solution was added $\text{SnCl}_2 \cdot 2\text{H}_2\text{O}$ (0.6 g, 0.2 mmol), and the reaction mixture was heated at 65 °C for 60 min. The mixture was quenched with NH_4OH to a pH of 5.5 and extracted with CHCl_3 . After drying and evaporation of the solvent, the purple solid was hydrolyzed in a solution of THF/ CH_3OH (2:1) (27 mL) and 40% KOH (5.4 mL). The mixture was stirred under argon for 16 h, 70 °C, cooled to room temperature, and adjusted to a pH of 5.8 using concentrated HCl and 1M HCl. The solution was extracted with ethyl acetate, dried over anhydrous Na_2SO_4 , and evaporated to dryness, affording a purple solid (0.076 g, 85%). ^1H NMR (500 MHz; d_6 DMSO; Me_4Si). δ_{H} , ppm -2.78 (2H, s, pyrrole-NH), 7.06 (4H, d, $J = 8.2$, Ph-amino), 7.91 (4H, d, $J = 8.2$, Ph-amino), 8.40 (4H, d, $J = 8.1$, Ph-carboxy), 8.45 (4H, d, $J = 8.1$, Ph-carboxy), 8.85 (4H, d, $J = 4.1$, pyrrole-H), 9.02 (4H, d, $J = 4.1$, pyrrole-H). MS (ES): m/z 733.47 ($[\text{M} + \text{H}]^+$ calcd. for $[\text{C}_{46}\text{H}_{33}\text{N}_6\text{O}_4]$ 733.25).

2.5 Poly-TAPP – Excitonic Solar Cell Construction

The nanostructured poly(4-aminophenyl)porphyrin films were incorporated into a bulk heterojunction device and evaluated with two electron accepting materials (PCBM and TiO_2). (Figure 10) The nanofibrous poly-TAPP was electrochemically grown from solutions containing 95% dichloromethane and 5% pyridine or just dichloromethane. The poly-TAPP electroactivity was maintained by using films deposited from less than 10 CV cycles. A PCBM bulk heterojunction solar cell was constructed by coating a 2% PCBM chlorobenzene solution ($10\ \mu\text{L}$) onto a $1 \times 1\ \text{cm}^2$ poly-TAPP coated FTO electrode using a capillary tube followed by slow drying ($\sim 3\ \text{min}$) in an undisturbed atmosphere. Poly-TAPP was not appreciably soluble in chlorobenzene, therefore the PCBM solution could be applied directly without concern for dissolving the underlying poly-TAPP layer. Reproducibility with the thickness of the PCBM layer varied from 50 to 150 nm thickness depending on the concentration of PCBM used for incorporation. The device was completed with a 0.6 nm thick LiF layer and 100 nm thick Al layer evaporated slowly ($0.1\ \text{nm/s}$) under vacuum (1×10^{-4} torr). Figure 10 depicts the poly-TAPP solar cell configuration using the nanostructured poly-TAPP film and incorporating either PCBM or TiO_2 within the poly-TAPP electrode. The incorporation of PCBM into the poly-TAPP nanofibrous film and the surface morphology of the PCBM coating were also studied using SEM and atomic force microscopy.

The effect of varying the poly-TAPP film thickness and film oxidation state (either neutral or in its most conductive state) on the solar cell performance was

examined. Poly-TAPP film thickness and surface coverage was varied using between 1 and 5 CV cycles for deposition. Pyridine was employed as co-solvent in the poly-TAPP electrochemical depositions to create a reproducible nanofibrous surface, however, the number of CV scans was five or less, therefore poly-TAPP film was in a conductive state before incorporation into the device.

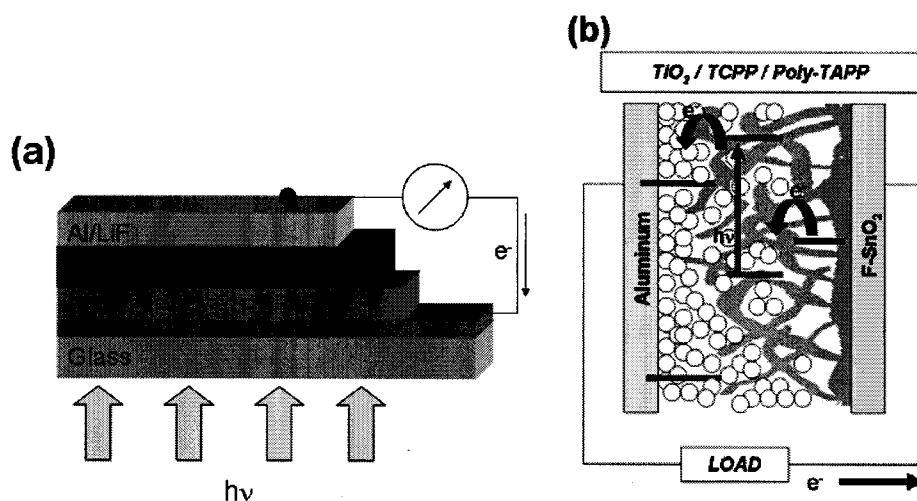


Figure 10. (a) Poly-TAPP bulk heterojunction solar cell device with either PCBM or TiO_2 incorporated into the nanostructured polymer film, (b) Inverse DSSC with a TCP coating and larger TiO_2 particle infiltration

To incorporate TiO_2 into the nanoporous poly-TAPP network to form an “inverse” dye-sensitized solar cell, the fibers were coated with a thin amorphous TiO_2 film using the commercially available titanium lactate precursor “Tyzor LA” [115,116]. Hydrolysis of the titanium lactate occurs at $70\text{ }^\circ\text{C}$ under acidic conditions ($\text{pH} \sim 1.2$) and results in the coating and pore filling of the nanofibrous poly-TAPP

network. Prior to the TiO_2 coating, the fibers were coated with a monolayer of tetrakis-5,10,15,20-(4-carboxyphenyl)porphyrin to provide a carboxylated, hydrophilic surface for the TiO_2 coating and to increase connectivity between the porphyrin nanofiber and the deposited TiO_2 . (Figure 10b) The TCPP forms amide bonds with the free surface amines of the poly-TAPP by using the tetracarbonyl chloride TCPP precursor (TCCPP) (as was detected by using UV-vis spectroscopy) which was synthesized as described below. After the deposition of the thin amorphous TiO_2 film on top of the TCPP coated poly-TAPP nanofibers, a commercial paste of TiO_2 nanoparticles (Solaronix) was applied to the electrode surface and allowed to sit overnight. This step was designed to fill in the remaining pores on the TiO_2 coated poly-TAPP electrode with an additional TiO_2 material providing increased contact to the nanofiber film and smoother contact for the final evaporated metal electrode. The inverse DSSC device was finished by rinsing excess TiO_2 particles off with water, heating at 120 °C to remove leftover surfactants, and evaporation of an Al top electrode contact. To detect the presence of the crystalline anatase TiO_2 particles, X-ray diffraction was used to confirm the presence of crystalline anatase TiO_2 material deposited from the Solaronix paste.

This type of device is an inverse dye-sensitized solar because the interfacial nanomorphology is dictated by the hole conducting polymer layer, rather than the mesoporous titania layer typically deposited in a DSSC prior to hole conductor material incorporation. (Figure 9b) The device is an “inversely” constructed device, but does not operate inversely to what is normally observed, i.e., electrons still migrate

through the TiO_2 layer to the back contact, and holes migrate through the nanofibrous hole conductor poly-TAPP layer.

5,10,15,20-tetrakis(4-chlorocarboxyphenyl)porphyrin. To a 50 mL roundbottom flask was added TCPP (obtained from TCI) (0.05 g, 63 μmol) which was refluxed with 10 mL of SOCl_2 for 24 hours, followed by distillation under vacuum to dryness. The dark green purple material was heated *in vacuo* for several days at 60 $^\circ\text{C}$ to remove any remaining reagent and was stored under vacuum.

Surface Reaction. Solutions of TCCPP (1.0 mM) were made up in anhydrous pyridine and CH_2Cl_2 (2% pyridine v/v) which had been dried over activated 4Å molecular sieves. Electrodes with deposited poly-TAPP films were then completely submerged in the solutions for 3, 6, or 12 hr. reaction times after which they were rinsed with CH_2Cl_2 /pyridine, acetone, distilled water, and ethanol. These samples were used immediately for device construction or analyses.

Chapter 3. RESULTS AND DISCUSSION

3.1 Poly-TAPP Electrochemical Syntheses

The electrochemical behavior of poly-tetrakis-5,10,15,20-(4-aminophenyl) porphyrin (poly-TAPP) films synthesized from solutions using only dichloromethane is shown in Figure 11. The cyclic voltammograms (Figure 11a) and quartz crystal microbalance measurements (Figure 11b) show typical behavior [117] of the electrochemical deposition of poly-TAPP onto an electrode from a dichloromethane

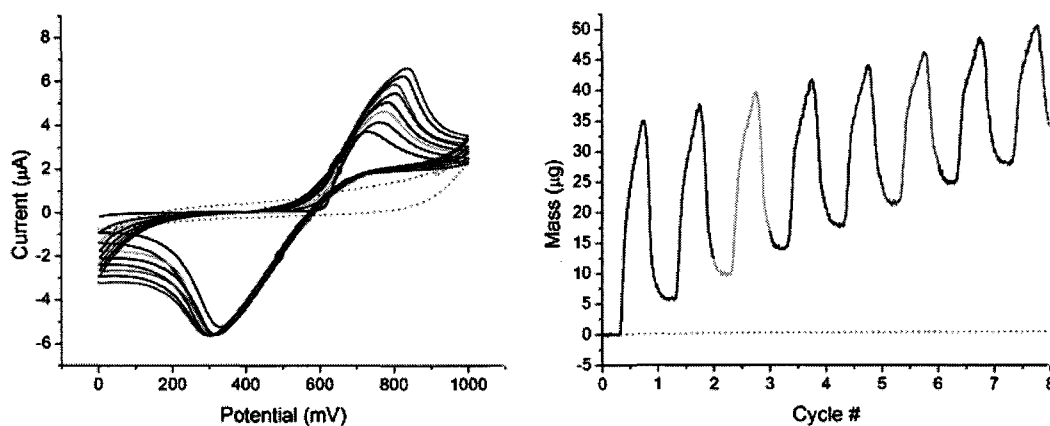


Figure 11. (a) Cyclic voltammograms of the first 8 cycles of TAPP electropolymerization in CH_2Cl_2 with TBAP supporting electrolyte and cycling the electrode from 0 to 1.0 V vs. Ag/AgCl, (b) QCA measurements for the adsorbed mass for the first 8 CV cycles including blank scans in electrolyte solution with no TAPP added (baseline)

solution using cyclic voltammetry (CV). Figure 11 shows an evolving cyclic voltammogram and corresponding quartz crystal resonator frequency changes obtained when a platinum coated quartz electrode is progressively scanned from 0 – 1.0 V vs. Ag/AgCl in a 150 μ M dichloromethane solution of TAPP with tetrabutyl ammonium perchlorate (TBAP) as supporting electrolyte at a scan rate (v) of 20 mV/s. The dotted line in Figure 11 is the CV scan when no TAPP monomer is present and a minimal amount of capacitive current due to electrolyte movement in solution is detectable. In DMSO, TAPP does not electropolymerize but exhibits a reversible two electron oxidation/reduction wave with $E_{1/2}$ (oxidation) close to +515 mV vs. Ag/AgCl [85]. The oxidation of TAPP conducted in dichloromethane shows reversible waves at 728 mV (forward) and 334 mV (reverse) with peak separation of (ΔE_p) 394 mV ($E_{1/2}$ = 531 mV vs. Ag/AgCl) which is considerably larger than the peak separation of forward/reverse oxidation of TAPP in DMSO (typically \sim 80 mV) [85]. Peak separations of 59 mV represent a perfectly reversible redox couple. With increasing scan numbers, the peak oxidation wave magnitude rises in addition to a steadily widening peak separation (over 800 mV by cycle 30). The increasing peak separation suggests a semireversible process not related to diffusion-controlled redox reactions. Apparently porphyrin film redox processes become steadily more irreversible upon successive scanning, requiring increasing overpotentials to oxidize additional porphyrin monomer from solution [76,81]. These findings agree with previous electropolymerizations of poly-TAPP onto a glassy carbon electrode from solutions

containing higher concentrations of TAPP monomer (1.0 mM) with a 500 mV peak separation by the 8th CV cycle [95].

Following film deposition, the porphyrin polymer is insoluble in most organic solvents including dichloromethane, acetone, ethyl acetate, and ethanol. Some film was observed to be removed when the coated electrode was submersed in concentrated H₂SO₄ or HCl, however significant amounts of the polyporphyrin adhered to the electrode even after strong acid treatment in agreement with previous poly-TAPP studies [90].

QCA data indicate that the electropolymerization and deposition process proceed with increased mass deposited (polyporphyrin, cations, solvent) on the electrode surface with each successive scan (1 CV scan correlates to 100s of the QCA data). The change in the resonant frequency of the platinum-coated quartz electrode is related to the adsorbed mass of poly-TAPP accumulated on the electrode during the electrodeposition using the Sauerbrey frequency/mass sensitivity relation [118]. The

$$\Delta F = -1.832 \times 10^8 (\Delta m)/A$$

area (A) of the platinum electrode used is 0.2 cm², which correlates with about 1 ng change in adsorbed mass (Δm) for every 1 Hz change (ΔF) in the resonant frequency. The oscillations which appear during each cycle indicate the diffusion of perchlorate anions and solvent in and out of the film as the electrode oxidizes/reduces the deposited porphyrin polymer film. The oscillations could also include porphyrin

oligomers/monomers which may have become deposited during oxidation and then become loosened or redissolved from the electrode surface during the reverse reductive sweep [118].

The electroactivity of the deposited porphyrin polymer is confirmed by cycling the film-coated electrode in a fresh electrolyte solution to observe oxidation/reduction upon repetitive CV scans. (Figure 12a) At low scan rates, the redox process is semireversible as indicated by a linear scan rate dependence of the peak current at low scan rates (≤ 20 mV/s) and relatively low values of ΔE_p . However, at scan rates > 20 mV/s ΔE_p increases and peak current shows a $(\text{scan rate})^{1/2}$ dependence; these indicate slow film response to the applied electrode potential. (Figure 12 b)

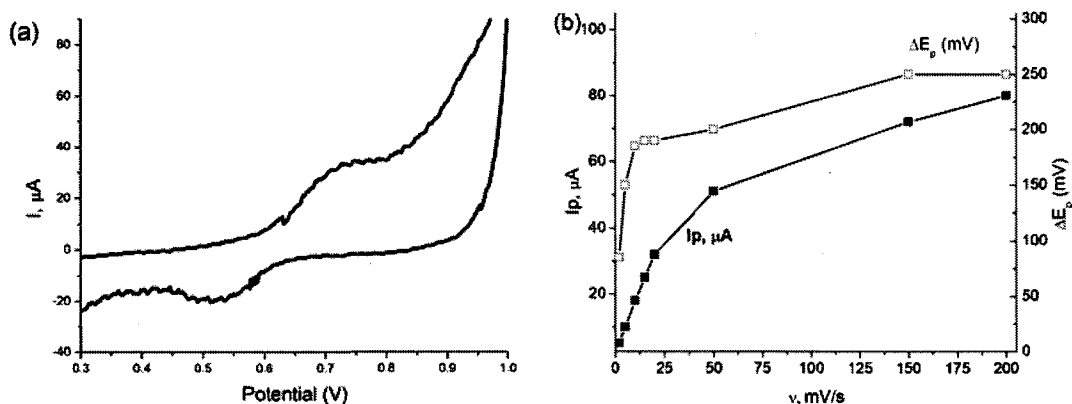


Figure 12. (a) Poly-TAPP film from 3 CV scans cycled in 0.01 M TBAP/acetonitrile solution at 50 mV/s, (b) scan rate dependence of peak current (I_p) and peak potential separations (ΔE_p) on oxidation of poly-TAPP film

Increasing separation between the forward and reverse peak oxidation (ΔE_p) is observed as either the film thickness (not depicted in Figure 12) or the scan rate increases. These types of behaviors have been observed for poly-(Ni)TAPP and were attributed to localized electroactive sites within the polymer limiting charge mobility within the film [90]. The electropolymerization of poly-TAPP with ortho substituted aminophenyl groups also exhibited this behavior with increasing ΔE_p during the actual polymerization, and upon repetitive cycling in a fresh electrolyte solution [76].

To calculate the number of electrons (n) involved in the oxidation of an electrochemically deposited film, the amount of charge passed during an oxidation wave was calculated by integrating the area under a CV scan (5.21×10^{-5} C). Using a general expression for diffusionless electrochemical systems, [119] and calculating

$$i_{pa} = (\Gamma n^2 F^2 A) / (4RT) \cdot \nu$$

for the charge involved with the porphyrin film oxidation (ΓnFA) - (the faradic current was subtracted from the calculated area under the oxidation wave), the (n) number of electrons and Γ (surface coverage in nmol/cm²) can be calculated where F is the Faraday constant, A is the electrode area (0.2 cm²), R is the gas constant and T is the absolute temperature. The scan rate (ν) used for this calculation was 20 mV/s which is the same rate used for the poly-TAPP electrochemical depositions. The number of electrons per oxidation step was calculated to be 0.87 per TAPP molecule which is slightly lower than a theoretical one electron oxidation per TAPP molecule. A 0.5

electron per porphyrin oxidation was reported for several tetra(4-hydroxyphenyl) porphyrins which was attributed to a 1 electron oxidation for two dimeric cofacial porphyrin molecules which has been observed for porphyrins whose macrocyclic ring structures are closely aligned (as they occur in a thin film) and whose redox entities respond like one molecule instead of two [120]. Moles of electrons were also compared to the moles of TAPP monomer deposited on the quartz crystal electrode after the first scan levels off upon returning to the initial potential of (0.0 V) with no further loss of mass after five minutes at this potential. The ratios of moles of electrons per moles of TAPP deposited is very low, (approximately 0.3 e^- per TAPP monomer) indicating that a substantial portion of the observed mass gain on the Pt electrode surface is due to trapped anions/cations/solvent if assuming a $\sim 1\text{ e}^-$ per monomer oxidation. This effect has been observed with poly-3,4-ethylenedioxy thiophene (PEDOT) where adsorbed mass due to electrolyte cation/anions remained within the films even after holding the film poised at a reducing potential for several hours to eliminate trapped electrolyte [121].

The increasing amplitude of the oxidation and reduction waves with each scan indicates an increase in the numbers of porphyrin molecules per cm^{-2} area (surface coverage $\Gamma = \text{nmol}/\text{cm}^2$) at the electrode surface. The adhered porphyrin polymer film remains electroactive throughout the polymerization up to 30 CV cycles. The surface coverage for poly-TAPP films deposited from 1 CV cycle was 3.3 nmol cm^{-2} obtained by integrating the charge under the CV curve of the film cycled in a fresh acetonitrile/TBAP solution. Previous investigations of poly-TAPP electrodepositions

indicate maximum surface coverage around 2.0 nmol cm^{-2} [95] for poly-TAPP, however it is unclear how many electrochemical depositions were used.

The molecular surface area coverage can also be calculated using absorbance of the film with the relation, ($\text{Abs.} = \epsilon \cdot \Gamma \times 10^{-6}$) with the Soret band extinction coefficient calculated previously for interfacially polymerized TAPP/TCPP films ($\epsilon = 6.7 \times 10^4 \text{ M}^{-1} \cdot \text{cm}^{-1}$) [60]. A surface coverage of 2.2 nmol cm^{-2} was calculated from the absorbance ($\Gamma = 15A_{\text{max}}$, A_{max} at 428 nm) of a poly-TAPP film deposited after 1 electrochemical cycle which agrees well with the surface coverage calculated using the charge under the CV oxidation wave (3.3 nmol cm^{-2}). Figure 13 (a) shows the surface coverage (nmol/cm^2 vs. the CV cycle number and UV-vis absorption characteristics (b) of poly-TAPP deposited from 1 and 15 CV cycles with a 30 second delay at the vertex. The surface coverage information shows a linear relationship of increasing poly-TAPP deposited with each electrochemical step (up to 15 electrochemical cycles) indicating that the adhered polymer is conductive with each oxidative sweep and can oxidize additional monomer from solution.

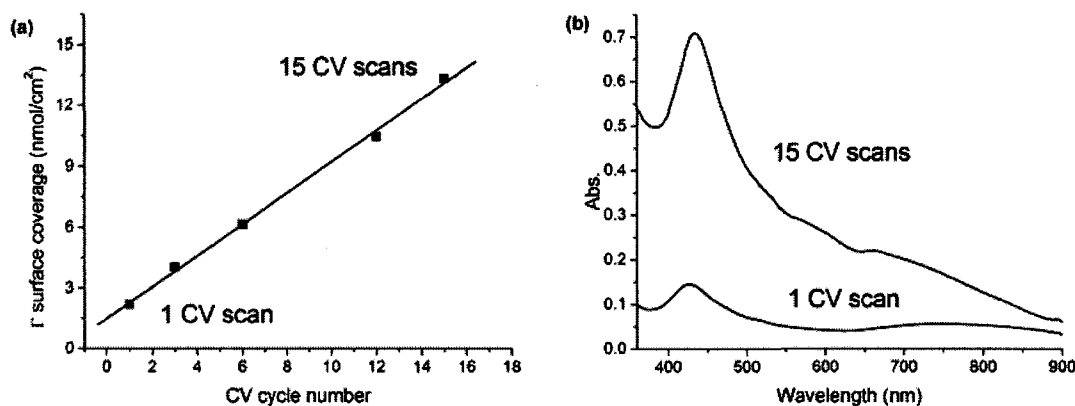


Figure 13. (a) Surface coverage calculated from absorbance at 428 nm vs. cycle number for poly-TAPP films deposited from 1 – 15 electrochemical cycles with linear fit, (b) absorption spectra for 1 and 15 CV cycles

Lastly, with surface coverage information and relative amounts of poly-TAPP deposited, the charge involved in the oxidative polymerization can be determined by performing chronocoulometry to deposit poly-TAPP using a fixed potential polymerization. Polymerizations were performed using EQCM measurements and deposited onto conductive FTO electrodes for surface coverage determination. For 1 x 1 cm² with up to 12 min of deposition with the working electrode poised at 0.4 vs. Ag/AgNO₃ reference electrode (the peak potential observed in the electropolymerization using cyclic voltammetry). Figure 14 (a) shows the increasing mass and final slowing of polymer depositions after 3 minutes of oxidation.

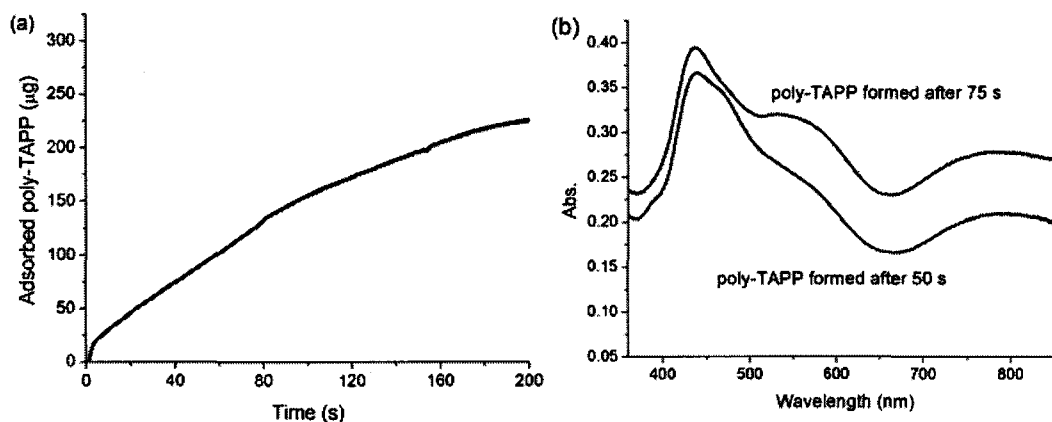


Figure 14. (a) EQCM – chronocoulometry of poly-TAPP deposition at 0.4 V vs. Ag/AgNO₃ from 0.15 mM TAPP, 0.01 M TBAP, (b) UV-vis spectra of deposited film after 50 & 75 s of fixed potentiometry electropolymerization

The number of electrons per mol TAPP monomer deposited was calculated for the polymerization as $\sim 7.5 e^-$ per TAPP monomer. The number of electrons per TAPP molecule utilized for the deposition will be discussed further in the growth mechanisms observed the electropolymerization of TAPP. It is important to note that there are four aminophenyl groups which can be further oxidized even after depositing the linked TAPP polymers onto the electrode surface, therefore it is not surprising that a large number of electrons were required for the deposition. Figure 14 (b) also shows indications that the film is still in its oxidized state with large absorbances in the 550 and 750 nm regions. These absorbances of conductive poly-TAPP have important implications for conductivity mechanisms operative within the films and will be discussed further.

3.2 Poly-TAPP Deposited from Pyridine:CH₂Cl₂ Electrochemical Solutions

As was noted, pyridine was initially added to the electrochemical solvent to ensure that TAPP remained neutral and deprotonated before the electrochemical polymerization. It has been reported that pyridine enhanced the rate of a tetra(hydroxyphenyl)porphyrin electrochemical deposition presumably by proton extraction after porphyrin coupling [95]. When electrochemical solutions of dichloromethane:pyridine (95:5) (v:v) were used to deposit poly-TAPP, initially the polymerization proceeded in a fashion similar to depositions using only dichloromethane. The cyclic voltammograms for the first three CV cycles are shown in Figure 15 (a) along with a combination (EQCM and CV) showing adsorbed mass increases in the potential range where electropolymerization can occur for the first two cycles. The CVs for the first three cycles show signature poly-TAPP oxidation waves with increasing peak current for each cycle at $E_{1/2}$ of 213 mV vs. Ag/AgNO₃. At the vertex of each scan (+0.7 V vs. Ag/AgNO₃) the potential was held for 30 s to enhance the amount of porphyrin polymer deposited during each cycle. The 30 s potentiometric delay at the oxidation vertex point was often used to increase the speed at which the film could be deposited and had little effect on the porphyrin film electrochemistry or (as will be shown) the general nanomorphology. Accompanying the oxidation process is the increased mass deposited on the electrode with each scan and a sustained increase in the deposited polymer during the 30 s vertex delay at 700 mV (vs. Ag/AgNO₃). The current and deposited mass during the delay is observed

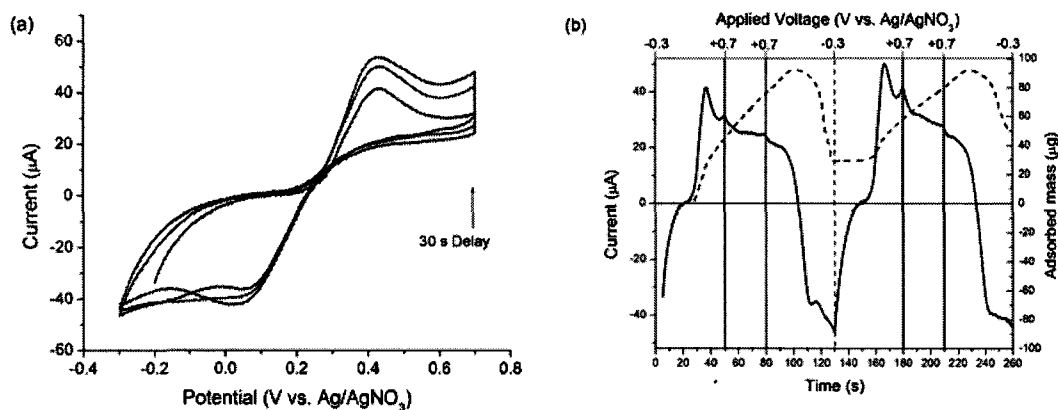


Figure 15. (a) Cyclic voltammogram of the first three cycles of TAPP electropolymerization under conditions using 95:5 (v:v) dichloromethane and pyridine, (b) combined CV (current, solid line) and EQCM (mass, dotted line) data for the first two cycles of electropolymerization of TAPP under standard conditions; the solid vertical lines show the 30 s constant potential delay at +0.7 V; the dashed vertical line shows the end of the first scan

between the vertical lines at 0.7 V indicating that the potential was held at during this time. The mass deposited does not decrease until the beginning of the reverse oxidation wave when the film begins to return to its neutral state accompanied by a dramatic loss of deposited material, presumably perchlorate counter ions, and perhaps porphyrin monomer/oligomers. Interestingly, although the current slowly decreased during the vertex delay, the rate of adsorbed mass increases steadily. This suggests that even though monomer diffusion limits the observable current, the rate of chemical coupling, polymerization, and deposition occurring at the electrode surface is sustained until the onset of the reverse oxidation wave. This is good evidence which

supports mechanisms where the oxidation of the monomer does not directly lead to deposition and increased mass. Rather, chemical coupling steps in solution between electrochemically generated TAPP radical cation molecules results in porphyrin oligomers and polymers of a “critical chain length” [122] which slowly become insoluble and deposit at the electrode surface. These findings agree with a monomer coupling rate determining step frequently cited for many conductive polymer electrodepositions [123,124].

Although typical electrochemical behavior was observed for the first 5 – 10 CV cycles of poly-TAPP deposition using pyridine, electrode passivation was observed after approximately 10 - 12 CV cycles. Cyclic voltammograms of the 1st and 15th CV cycle and are shown for poly-TAPP films electrodeposited from dichloromethane and pyridine solutions in Figure 16. After 15 CV cycles,

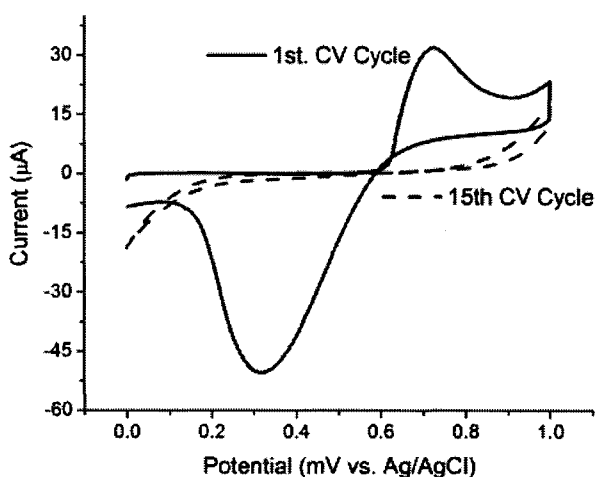


Figure 16. CV cycles for the 1st and 15th electrochemical cycle for poly-TAPP electropolymerization using 95:5 (v:v) pyridine and dichloromethane

the oxidation envelope disappeared, indicating loss of electroactivity such that the film can no longer be oxidized, nor can it oxidized additional TAPP monomer from solution. The film passivation and loss of conductivity is also observable in the EQCM data shown in Figure 17 depicting electrochemical TAPP polymerization conducted with and without a 30 s vertex delay. The addition of 5% pyridine to the dichloromethane electrochemical solvent increased the overall material deposited per cycle for the first 15 CV cycles depositing as much as four times the amount of material during the same 15 CV scans without the use of pyridine. (Figure 17 a) However, it was discovered that after a few cycles the magnitude of anion diffusion in and out of the deposited film is significantly decreased indicating loss of film electroactivity.

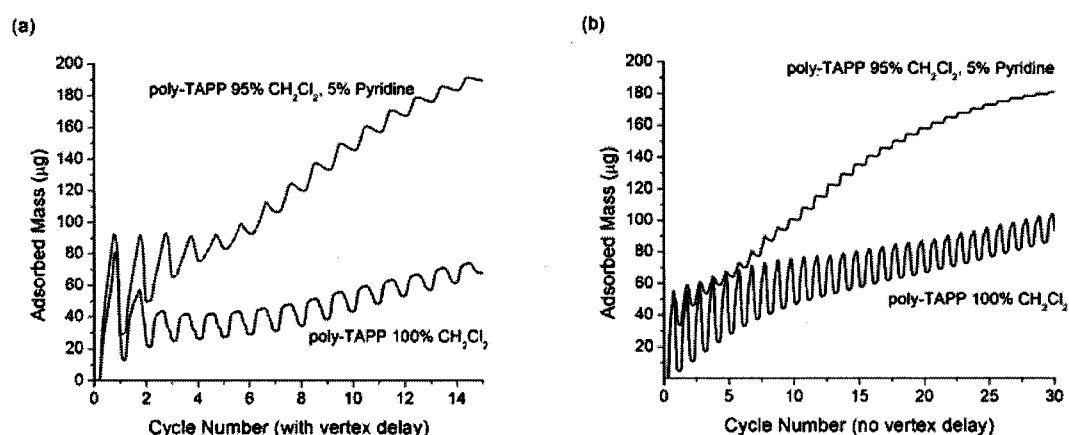


Figure 17. (a) EQCM data for 15 electrochemical cycles for poly-TAPP electropolymerization with 30 s vertex delay, (b) Data for 30 cycles with no vertex delay

The decrease in the migration of anions in and out of the poly-TAPP film is amplified in the EQCM data for 30 CV cycles (Figure 17 b) where the loss of mass due to the changing potential is almost negligible by the 30th CV cycle in samples deposited from solutions containing pyridine. Films which were deposited from solutions containing only dichloromethane exhibited continuing conductivity through 30 CV cycles.

The trends observed in the cyclic voltammograms were also confirmed by evaluating the surface coverage for each CV cycle. Poly-TAPP films were deposited on FTO glass electrodes from 15 CV cycles using with or without base (100 % dichloromethane or 95:5 dichloromethane:pyridine) to examine the adsorbed polymer after the electrodepositions. Surface coverage was calculated using the molar absorptivity as previously described using the Soret peak at 428 nm. Figure 18 (a) depicts the absorption characteristics of films showing the strong Soret peak and indications of the four Q-band absorptions from 500 – 700 nm. Again, the presence of the characteristic porphyrin Soret peak and Q-bands in the absorption spectra is an indication that the porphyrin macrocycle was not affected during the electropolymerization [125]. Figure 18 (b) indicates that the deposition rate when using pyridine during each scan is initially accelerated but begins to slow as surface coverage increases indicating loss of poly-TAPP film electroactivity. The surface coverage of poly-TAPP films deposited using only dichloromethane steadily increased at a rate of 0.8 nmol / CV cycle.

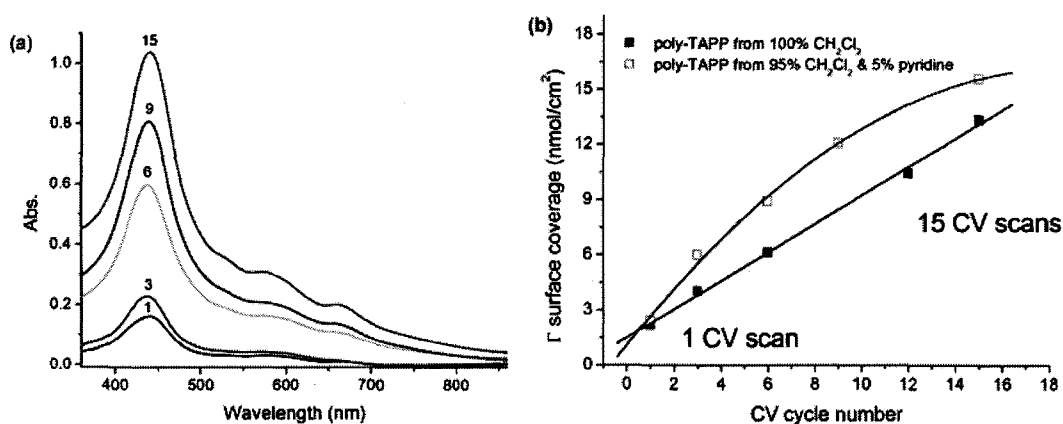


Figure 18. (a) Electronic absorption spectra of poly-TAPP deposited on FTO from 1-15 cycles from pyridine-containing solution, (b) Surface coverage (Γ) vs. CV cycle number for poly-TAPP deposited from solutions with and without pyridine

3.3 Surface Morphology of Poly-TAPP

The surface morphology of poly-TAPP films were characterized using scanning electron microscopy (SEM) to examine the effects of the various synthesis methods. The poly-TAPP films deposited after 3 CV cycles (with 30 s vertex delay) using only dichloromethane solutions (Figure 19 a) exhibit significantly different morphologies than those films produced from solutions containing 5% or 15% pyridine. Poly-TAPP deposited from solutions containing pyridine exhibited well-connected, continuous nanoporous polymer networks (Figure 19 b, c, d) uniformly deposited across the electrode surface. Film thickness varied greatly with the thickest films obtained from using solutions containing 5 - 15% (vol.) pyridine. When

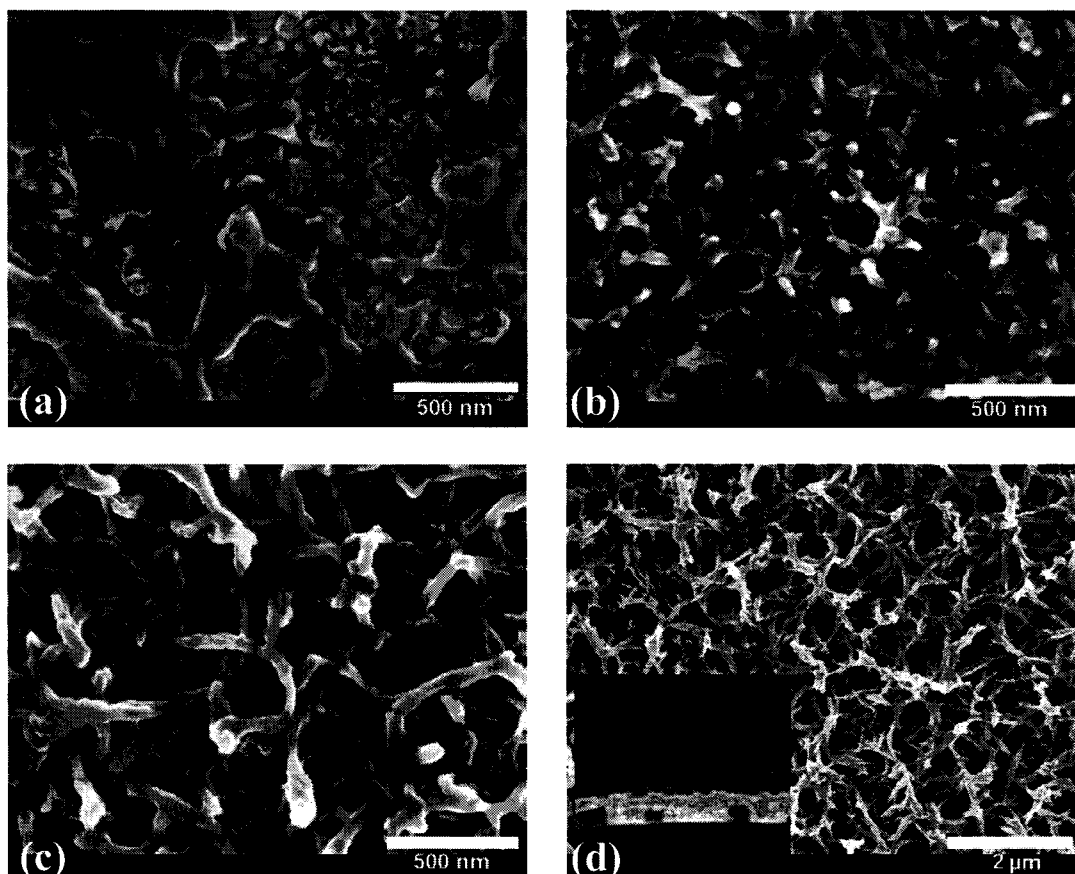


Figure 19. SEM images of poly-TAPP films electropolymerized on FTO electrodes using cyclic voltammetry in a solution of 95:5 (v:v) dichloromethane:pyridine, (a) 3 CV scans, 0% pyridine, (b) 3 CV scans, 5% pyridine, (c) 3 CV scans, 15% pyridine, (d) 15 CV scans, 5% pyridine, (inset) film thickness measurement (528 nm) from cross section of poly-TAPP film

increasing the scan count to 15 to 30 CV cycles, films produced from solutions containing only dichloromethane were thickest due to the sustained film conductivity. The film thickness for both solvent conditions averaged 80 nm for 3 to 5 CV cycles and up to 500 nm for films deposited with 15

electrochemical cycles. (Figure 19 d) In general, because of the high surface roughness, film thickness varied (± 50 nm) over the surface area of the electrodes (~ 1 cm²); however, nanostructured structural features were observed throughout the deposited porphyrin film with high uniformity.

Poly-TAPP films made using the same potentiometric method without pyridine in the electrochemical solution have an amorphous film structure with scattered fiber depositions with the underlying FTO electrode surface still visible in some locations (Figure 19 a). In general, when using only dichloromethane, a wide variety of structures were observed to be deposited on the same sample. Unlike those samples using pyridine, it was difficult to control the uniformity of the deposited films. The SEM images also reveal that a more defined nanofiber structure is deposited more quickly with increasing pyridine concentration; for example Figure 19b shows a denser nanostructured film surface with smaller pores than films obtained from using 15% pyridine.

An approximate surface area was calculated using a nanocylindrical model where the nanofiber diameters from SEM images, the approximate nanofiber coverage in a given area from SEMs of 3 CV cycles (where typically only one or two layers of nanofibers typically are observed), and the surface coverage determined from CV measurements (Γ) are used to calculate the surface area s_0 . This simple estimation method was used with polyaniline nanofibers and gave values reasonably close values to the actual measured values using nitrogen adsorption-desorption isotherms the from Brunauer-Emmett-Teller (BET) method [126]. Using data from a poly-TAPP film

deposited from 3 electrochemical cycles (Figure 19 c - diameter = 50 nm, $\Gamma = 4.02$ nmol cm⁻², $s_0 = 25$ m² g⁻¹) it was possible to estimate the surface area for poly-TAPP

SEM images in Figure 20 show the surface morphology of poly-TAPP films deposited (using 15 CV cycles) at different magnifications to reveal how poly-TAPP grows within a layered morphology and that the nanofibrous nature extends down to the FTO electrode surface. Figure 20 (a) shows a cross-section of poly-TAPP film (from 15 CV cycles in pyridine-containing electrochemical solutions) isolated on a small flake of FTO glass imaged at an 85° angle. The poly-TAPP fibers have a rounded geometry with diameters ranging from 40 - 100 nm. The nanofibrous mats are well connected, forming a spongy network indicating a multi-directionally oriented nucleation and deposition. Pore sizes range from 10 to 500 nm. This image also indicates fiber size stratification in the film with smaller fibers located closer to the electrode surface in a more densely packed arrangement. Figure 20 (b) shows a poly-TAPP film imaged at a 40° angle with a mechanically scraped region in the foreground which is characterized by clumps of fibers that are compacted where the film was removed. Figure 20 (c) is an SEM image captured after 15 electrochemical cycles with a vertex delay showing nanofibers growing across small nonconductive gaps that were detected on the surface of the FTO electrode. In particular, it appears that the nanofibers grow across the nonconductive defect region at the upper layers of the film. Figure 20 (d) shows the polymer nanofiber interconnectivity suggesting that the fibers may exhibit some chemical interactions or bonding during electrochemical deposition of the film.

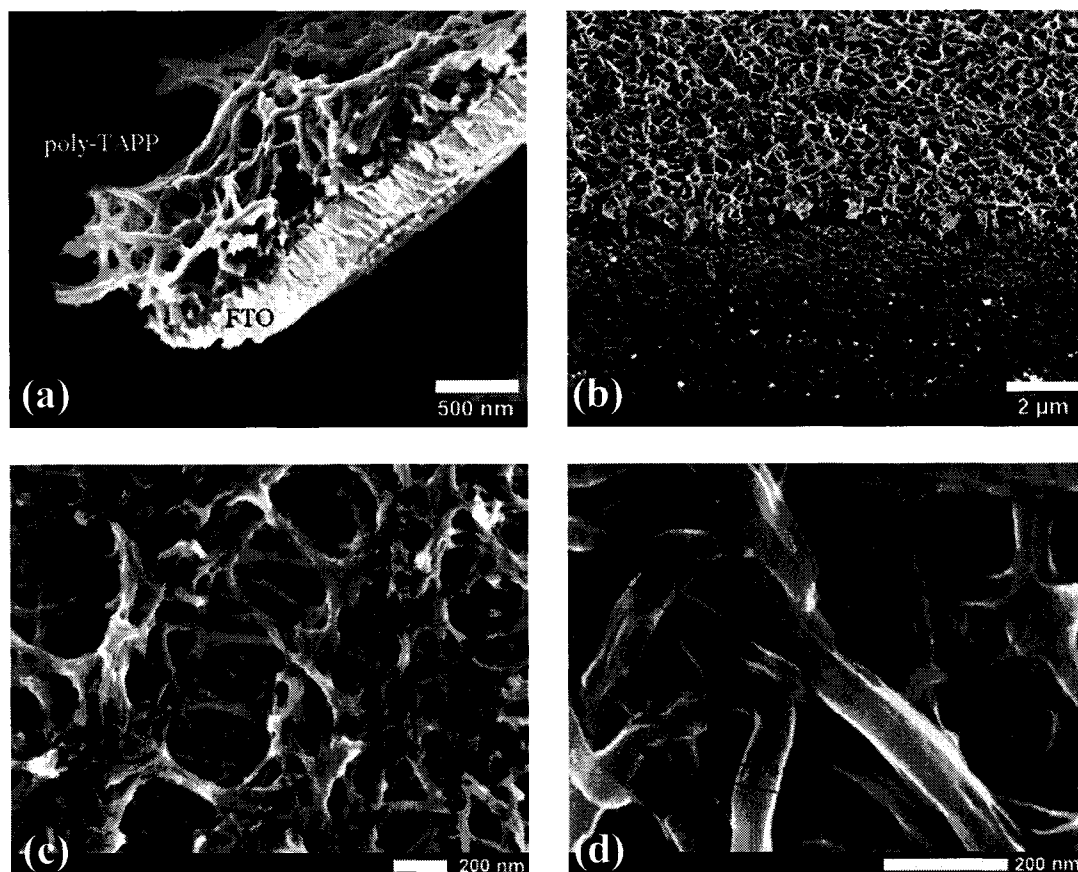


Figure 20. Poly-TAPP film deposited with 15 scans under conditions identical to Figure 19 b, d: (a) cross-section, (b) mechanically scraped section, (c) 15 CV scans, 5% pyridine where film has grown over a nonconductive surface scratch, (d) films deposited using 3 cyclic voltammetry scans at higher magnification

AFM images confirm the general features observed in the SEM for these electropolymerized films. Films synthesized from solutions without pyridine show rough polymer morphology with lumps and grooves associated with an amorphous

polymer structure. The surface roughness exceeds 100 nm for nanostructured poly-TAPP films deposited from 3 CV cycles. (Figure 21)

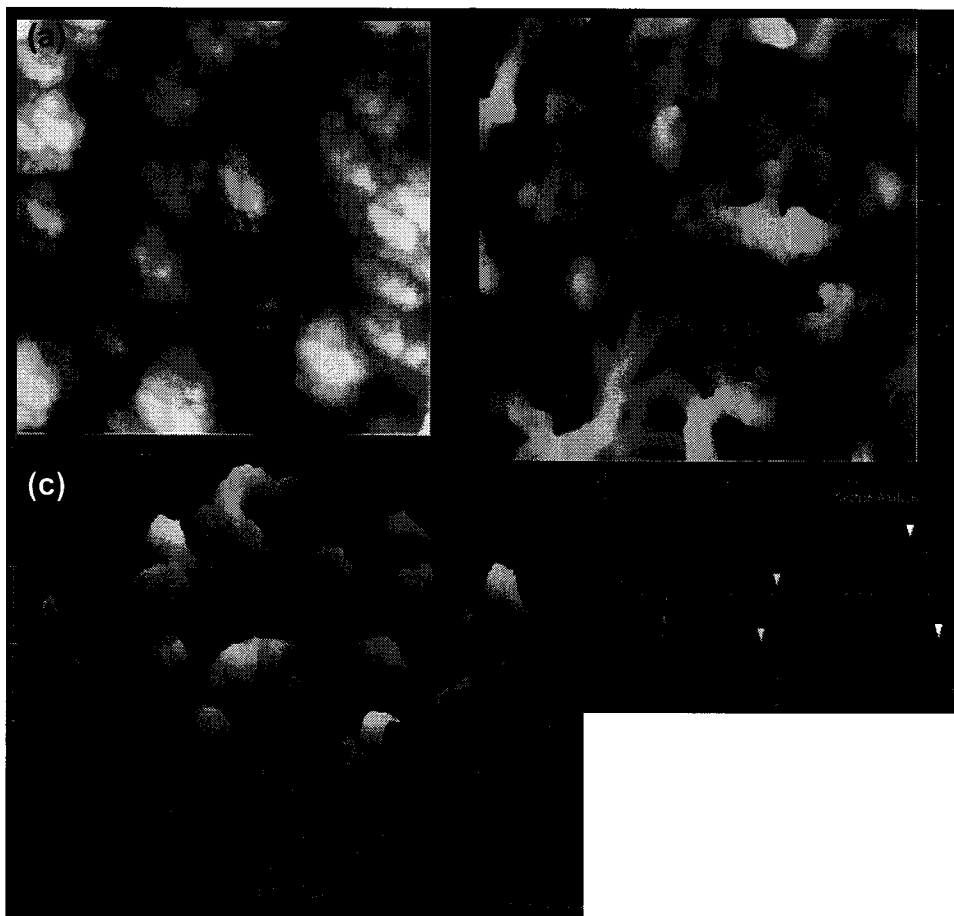


Figure 21. AFM images of poly-TAPP film deposited from (a) dichloromethane without pyridine, (b) 95:5 (v:v) dichloromethane:pyridine, with (c) cross-sectional analysis

Surprisingly, it was discovered that pyridine reacts with dichloromethane over time to form a dipyridinium dichloride which was found to impede nanofiber formation, therefore solutions of TAPP in CH_2Cl_2 /pyridine could not be stored for

longer than a few hours. To solve this, lutidine (2,6-dimethylpyridine) was used, and remained stable (because of steric hindrance, lutidine cannot react with CH_2Cl_2) allowing TAPP solutions to be used hours/days later while retaining the ability to grow nanostructured poly-TAPP films.

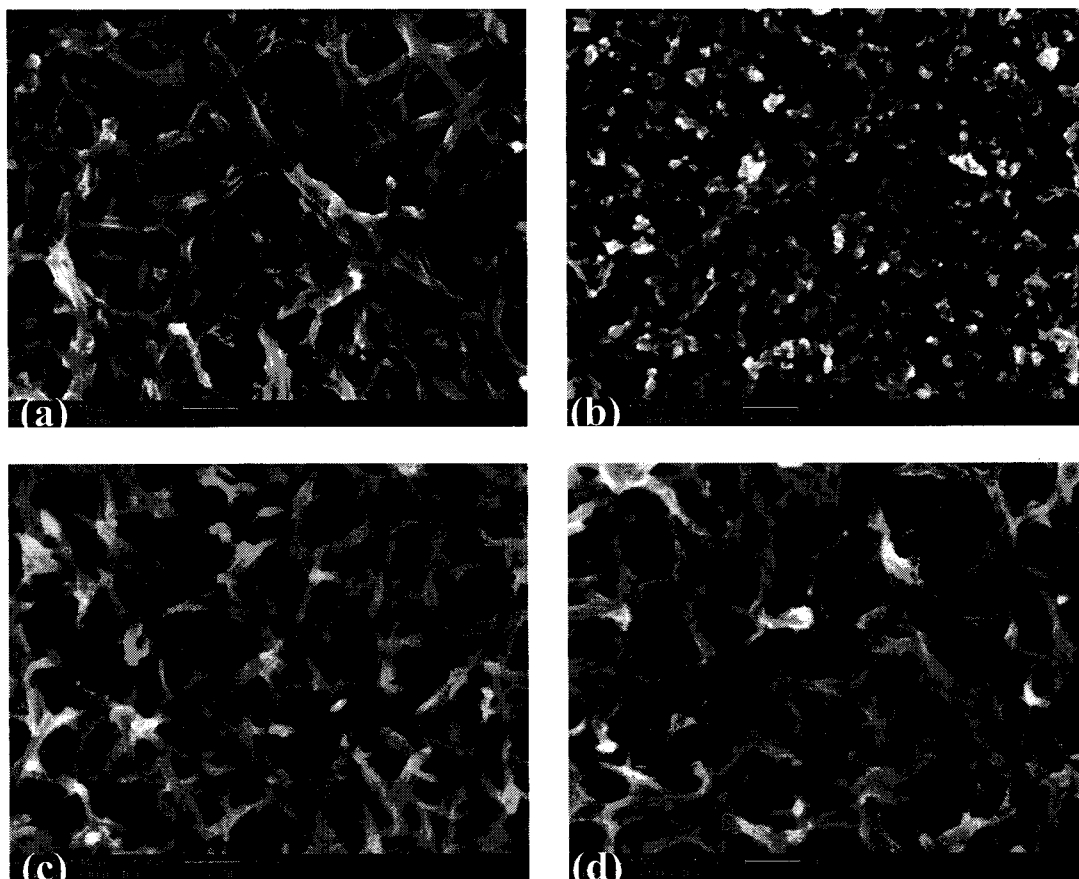


Figure 22. Poly-TAPP from fresh solution (a) after 1 hour, (b) film deposited after 24 hours, (c) poly-TAPP from solution with lutidine after 1 hour, (d) after 24 hours

3.4 The Effects of Dissolved Water on Poly-TAPP Films

Differences in the observed electrochemical deposition of poly-TAPP nanofibers were initially thought to be determined by pyridine concentration alone. However, after examining the effect of dissolved water in the electrochemical solvent it was determined that trace water concentration was also very important for the nanostructured electrochemical poly-TAPP syntheses. Conditions were tested involving poly-TAPP films deposited from rigorously anhydrous dichloromethane and pyridine (95:5) onto an FTO conductive electrode using standard conditions. The typical CV was obtained, and the resulting EQCM data again showed eventual passivation of the electrode after about 10 – 15 CV cycles. (Figure 23) The surface morphology of these films however was completely structureless exhibiting a flat surface with minor indications of small bumps. (Figure 24a) Films were prepared using standard HPLC grade solvents which contain less than 0.1% dissolved water and also prepared with solutions in which the dichloromethane layer had been saturated with water (~1 %) before adding pyridine. Films deposited using a water saturated dichloromethane/pyridine solution exhibited an increased deposition rate with minimized film passivation as depicted in the EQCM graph of the three conditions. Even after 30 CV cycles, there was still a small amount of anion migration in and out of the film indicating film electroactivity. It is surprising that such a small change in the concentration of dissolved water can significantly influence the polymerization rate, and the film nanostructure.

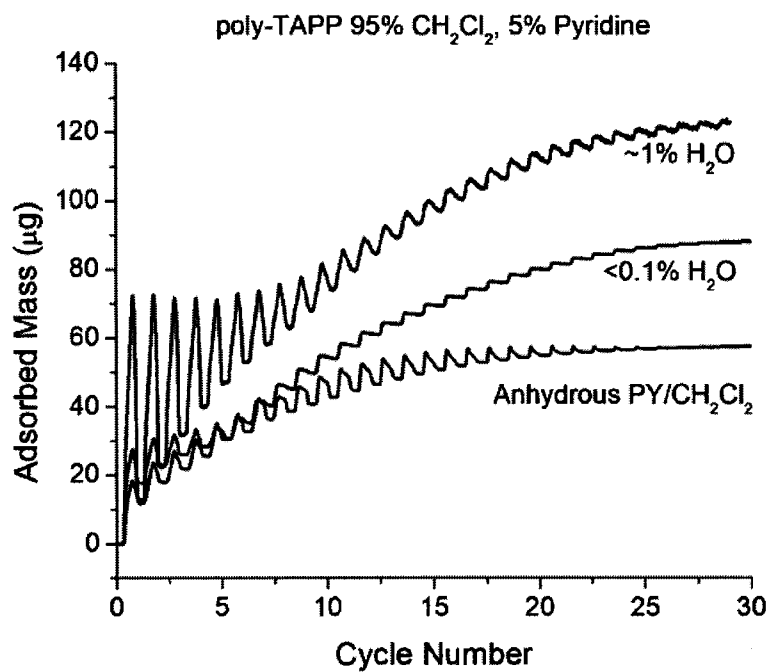


Figure 23. EQCM for poly-TAPP depositions with trace amounts of dissolved water: 1%, $\leq 0.1\%$, and anhydrous (rigorously dried)

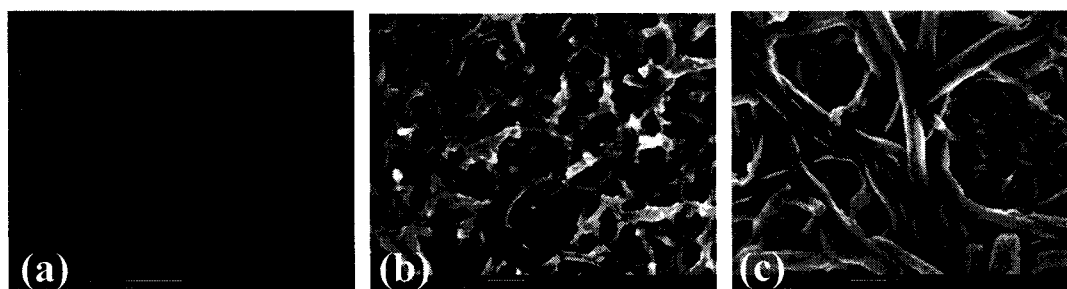


Figure 24. SEM images of poly-TAPP films electrochemically deposited after 15 CV cycles in 95:5 dichloromethane:pyridine, (a) anhydrous conditions, (b) $\leq 0.1\%$ H₂O, (c) $\sim 1\%$ H₂O

The surface morphology results indicate that dissolved water plays an important role in the depositing the nanostructured polymer. Several porphyrin electrooxidative studies have suggested that trace water can play a role in the formation of the π cation radical with anhydrous conditions leading to minimal radical formation and too much water leading to radical quenching [127]. Other studies have reported the effects of dissolved water on the electropolymerization of other conductive polymers such as polypyrrole [128], and polythiophene [129]. Several of these studies have suggested that due to the pK_a of dissolved water in polar organics (H_3O^+ , 2.4) like acetonitrile, water can serve as an efficient base to extract electrochemically generated protons. In the case of polypyrrole deposition in acetonitrile, small amounts of water (~1%) increased the polymerization rate, the conductivity, and improved the film adherence to the electrode [130]. In these studies it was determined that pH at the surface of the electrode needed to be buffered due to the production of protons from the polymerization which protonated intermediates eventually halting the electropolymerization by incorporating nonconductive lengths of the polypyrrole [131]. As has been observed with poly-TAPP polymerization, pyridine was also found to intervene in the electrochemical polymerization of pyrrole and thiophene leading to loss of film conductivity and electrode passivation for both electrochemical polymerizations [132-134]. It was desirable to try and replace pyridine with alternative solvents which might provide the small amounts of dissolved water needed for buffering the electrochemically generated protons at the electrode

surface while avoiding conditions which led to electrode passivation when excess pyridine was used.

To examine this hypothesis, films were prepared from dichloromethane solutions which had been saturated with water or solutions which contain solvents which were miscible with water. Acetonitrile was chosen because of its miscibility with water and dichloromethane. The electropolymerization of TAPP in pure acetonitrile did not deposit films onto FTO electrodes within 15 – 30 CV cycles which is in agreement with Bettelheim et al. [95]. However, films could be produced from 5 – 10% solution mixtures of dichloromethane and acetonitrile using 15 CV cycles.

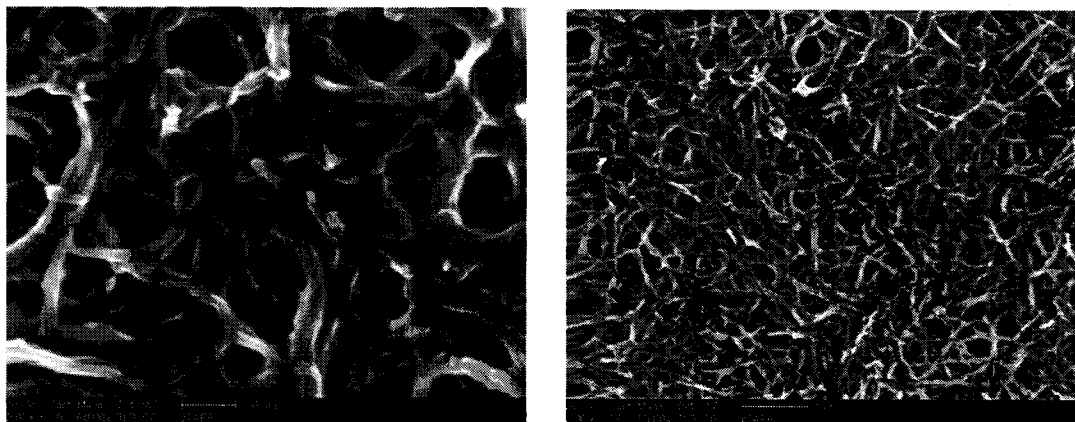


Figure 25. Poly-TAPP films deposited from 15 CV cycles with water saturated dichloromethane ~1%

The SEM surface morphological results presented in Figure 25 show that nanofibrous morphology can be obtained without using pyridine, and that addition of solvents containing small amounts of dissolved water can also lead to interesting

nanostructured features. (Figure 26 a, b) Fiber widths were observed to be slightly larger with diameters ranging between 100 – 200 nm which is double the size of poly-TAPP nanofibers obtained when using the conditions with added pyridine.

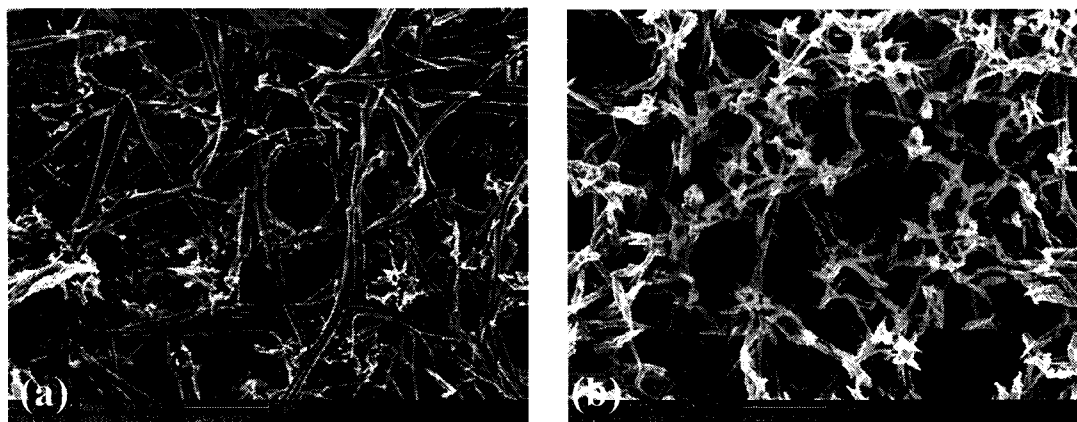


Figure 26. Poly-TAPP film deposited from 15 CV cycles in CH_2Cl_2 with: (a) 5% acetonitrile, (b) $\leq 0.1\%$ water

The greatest improvement of synthesizing poly-TAPP nanostructures without using pyridine is retaining the film's conductivity throughout the electrochemical polymerization process. This was observed in the EQCM data with sustained growth and conductivity after 30 CV cycles. (Figure 27) There is also evidence that solutions containing greater quantities of dissolved water have a slight catalytic effect on the polymerization deposition process suggesting that the water can serve to help extract protons from the monomer coupling step as was suggested with polypyrrole electropolymerizations.

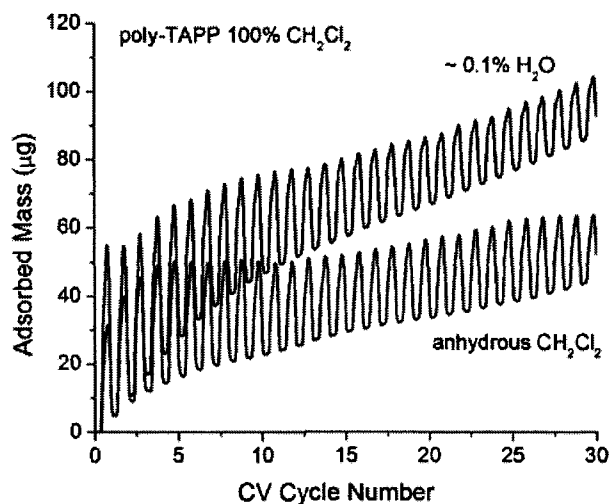


Figure 27. Poly-TAPP grown from dichloromethane solutions containing $\leq 0.2\%$ dissolved water and anhydrous conditions

3.5 The effects of porphyrin derivative on film growth

To examine the effects various aminophenyl derivatives had on the surface morphology of electropolymerized porphyrin films, porphyrins synthesized with three aminophenyl groups (TA₃CMPP) and two aminophenyl groups (cis/trans TA₂CM₂PP) were evaluated using standard electropolymerization methods. It had been observed [111] that when performing electrochemical analyses on various carboxy/aminophenyl porphyrins using cyclic voltammetry, a thin film could be deposited from solutions of the triaminophenyl derivative (TA₃CMPP) and the trans-TA₂CM₂PP however little or no film was deposited from the cis-TA₂CM₂PP derivatives. When examining the film nanofiber structure, TA₃CMPP exhibited nanopod-like structures on the surface, while

the trans-TA₂CM₂PP showed very few surface features (a few bumps). The cis-TA₂CM₂PP did not polymerize any substantial porphyrin material after 30 CV cycles; the first electro-oxidative wave was irreversible and was not repeated during the second CV cycle. Little or no film was detectable in the UV-vis after the deposition using 30 CV cycles of cis-TA₂CM₂PP. In comparison, the TA₃CMPP and trans-TA₂CM₂PP deposited thick films which were conductive for the first 5 – 10 CV cycles. Figure 28 summarizes observed film surfaces from the porphyrin derivatives.

Several authors have reported the effects of hydrogen bonding on polyaniline supramolecular structures observed in electrochemical and chemical oxidative polymerizations [94,135]. These studies have indicated that intermolecular hydrogen bonding observed between the secondary amines and imine groups on adjacent PANi polymer chains are responsible for the nanostructured fiber/tube formation. The stretching vibrations of the secondary amines shifted dramatically when nanostructure features were present suggesting that aggregation of polyaniline materials and deposition is largely regulated by concentration of polymer chains and less concerned with the effects of surfactants and other methods to induce nanostructured features like the micelle forming techniques used to form polypyrrole nanofibers [136]. This is in agreement with other authors working on nanostructured conductive polymers like polyaniline who have shown that reaction time and concentration is more important to

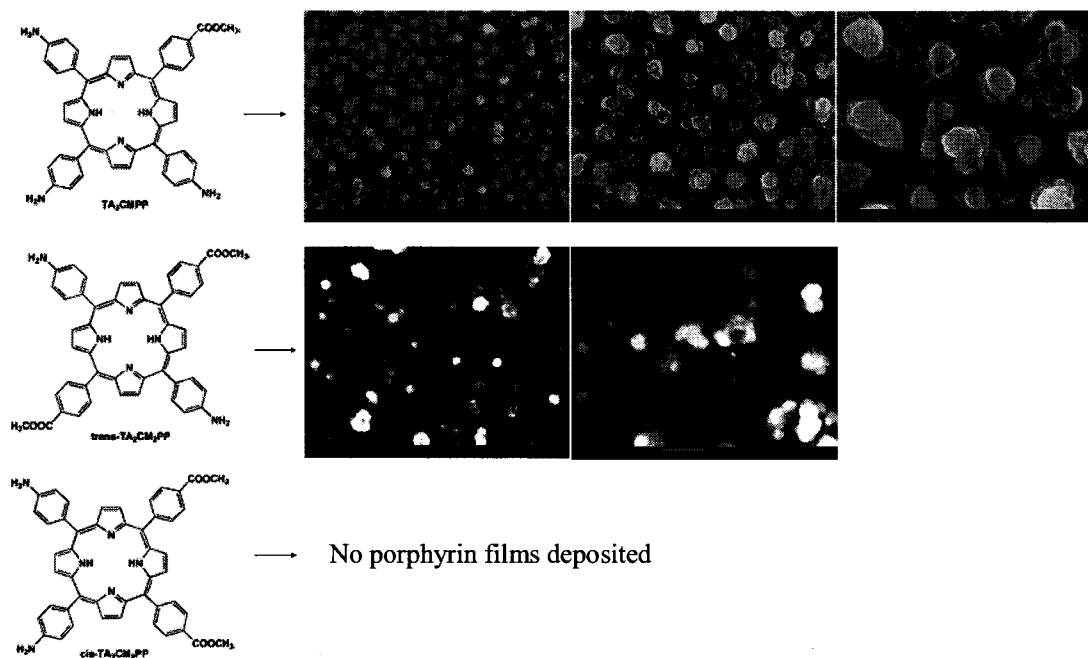


Figure 28. Surface features observed for electropolymerized films obtained from TA_3CMPP and $\text{trans-TA}_2\text{CM}_2\text{PP}$. The $\text{cis-TA}_2\text{CM}_2\text{PP}$ derivative did not deposit any substantial film and exhibited one irreversible oxidation which was not repeated after the first CV cycle. All images from films were produced from CH_2Cl_2 with $\leq 0.1\%$ H_2O

hetero or homogenous nucleation during polymerization and precipitation [108,126,137,138]. Therefore, a simplistic approach for explaining the observations of nanostructured features solely found with the tetra(aminophenyl)porphyrins and not found with porphyrins containing three or less aminophenyl groups is polymer chain aggregation based upon hydrogen bonding between free aminophenyl groups. Therefore, an increased likelihood of these interactions will occur with TAPP over the

other derivatives. The observation of films containing the most nanostructure is in descending order with the trans-TA₂CM₂PP exhibiting the least structured film. The interaction between the two carbomethoxyphenyl groups is limited while the TA₃CMPP has a greater likelihood with one free aminophenyl group. Further evidence of this approach will be presented in the reflectance FT-IR data which show changes in the aminophenyl stretching frequencies associated with hydrogen bonding in the nanostructured polymer films.

3.6 Chemically Interfacially Polymerized Poly-TAPP

The usefulness of poly-TAPP nanofibers grown on conductive substrates is somewhat restrictive due to the limitations of processability as well as the ability to adequately characterize materials electrochemically deposited. An alternative method to chemically polymerize poly-TAPP was sought to allow for better processing and characterization. One method, which has shown to be useful in the synthesis of polyaniline nanofibers at an aqueous/organic interface was developed by Huang et al. to chemically oxidize TAPP monomer at an aqueous/dichloromethane interface using ammonium persulfate (APS). [126,137] Similar experiments were performed using 0.15 mM TAPP and a large molar excess (8 mol equivalents per TAPP of APS dissolved in water at 3.4 mM). The results were dramatic; a thin, (5 - 10 μ M) durable film was produced in 12 hours at the interface accompanied by a complete disappearance of the TAPP in solution. The black films could be harvested with a glass electrode or microscope slide, dried and then handled as a free standing film.

Interestingly, the film nanostructure also presented a nanofibrous structure within large “clumps” of polymer in the films. Digital images depicting the reaction

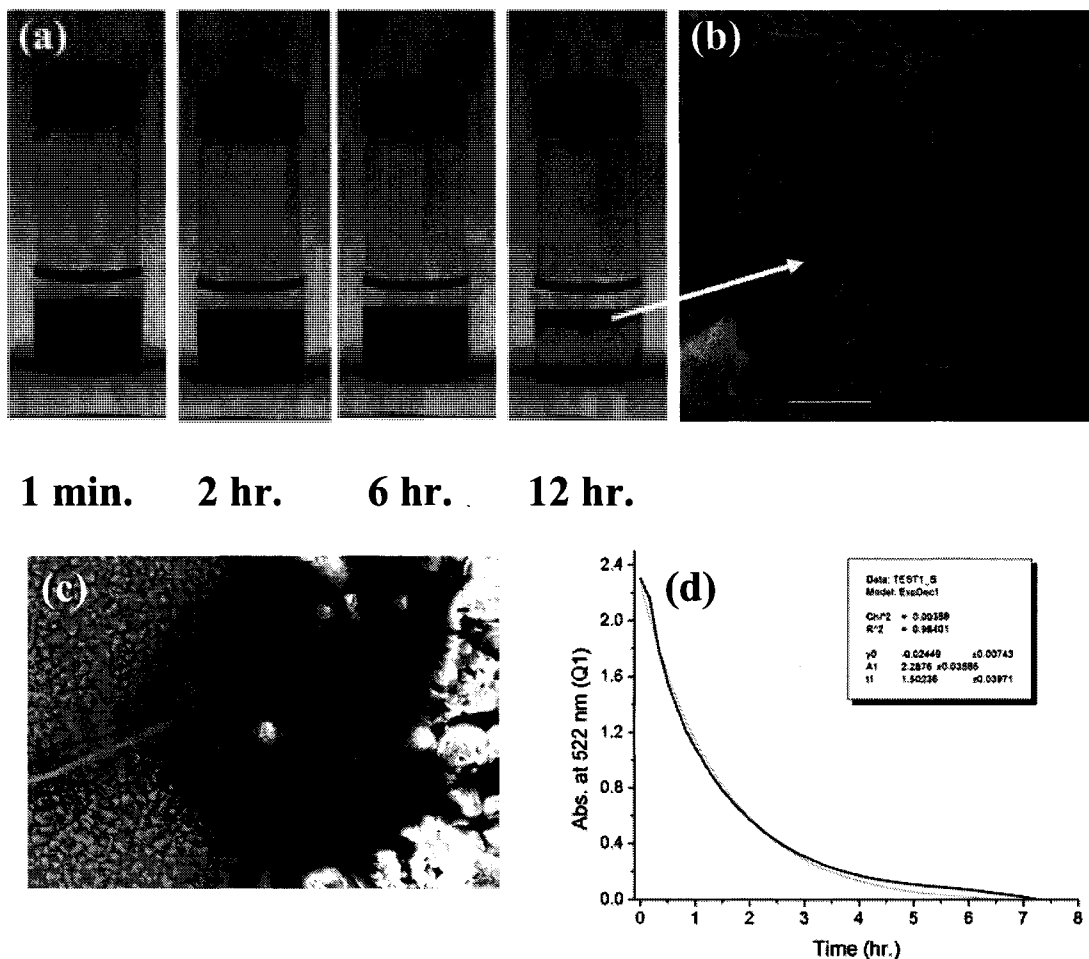


Figure 29. (a) Interfacial poly-TAPP polymerization over 12 hrs reaction time, (b) SEM image of nanofibrous poly-TAPP film, (c) larger “clumps” of harvested porphyrin polymer films within which nanofibrous features were discovered, (d) concentration of TAPP in solution over time with first order decay fit (dotted line)

over 12 hours in a 20 mL sample vial (Figure 29 a) and film SEM images are presented (Figure 29 b, c). Figure 29 (d) depicts the monitoring of TAPP monomer concentration over time as it diffuses to the interface for oxidation and polymerization. This reaction was gently stirred to ensure that the solution concentration remained uniform throughout the interfacial reaction. Therefore, unlike the experiment shown in Figure 29 (a), fresh monomer was continuously available for oxidation and polymerization.

As seen in Figure 29 (a), the oxidation of monomer is rapid enough to form a depletion region just below the surface of the film after two hours. Therefore the rate of polymerization is controlled by TAPP monomer diffusion after the initial oxidation and film formation. Figure 29 (c) shows the SEM image of the larger clumps of poly-TAPP film that were harvested from the interfacial reaction. Fortunately, several of the clumps were split open or halved, which allowed for the discovery of the nanofiber center seen in Figure 29 (b). Although these films were not used for further study, this polymerization method presents a very promising route for creating harvestable nanostructured poly-TAPP films.

3.7 Poly-TAPP Structure and Mechanisms for Growth and Conductivity

The electrochemical polymerization of poly-TAPP is presumed to progress much like polyaniline with an oxidative step to form TAPP radical cations which couple to form initial diphenylamine linkages with the loss of 2 protons/2 e⁻ per coupling step. Further oxidation of the TAPP dimer can lead to dihydrophenazine

linkages or eventually to completely aromatized phenazine linkages. (Figure 30)

To reach the dihydrophenazine structure, the loss of $4 e^-$ per linkage is

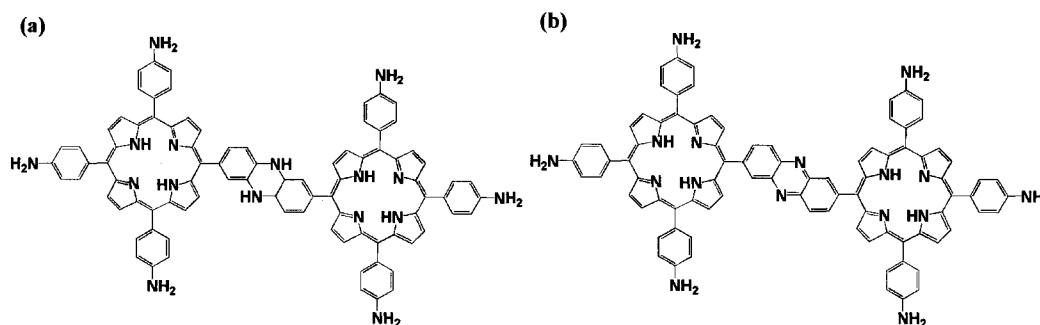


Figure 30 (a) Dihydrophenazine linked dimer, (b) phenazine linked dimer

required. Complicating the situation is the fact that there are 3 other aminophenyl groups which could all participate in the oxidation/polymerization steps which may lead to cross-linking of polymer chains or formation/precipitation of a wide variety aminophenyl linked TAPP oligomers.

Reflectance FT-IR was used to examine signature vibrational transitions for poly-TAPP films obtained from both primary conditions used for the polymerizations studied, i.e., with and without the addition of 5% pyridine to the electrochemical solution. An analysis of the FT-IR spectrum for TAPP has been reported [139] and was used to identify primary TAPP structures in the spectra obtained for the electrochemically deposited films. Figure 31 shows the FT-IR spectra for poly-TAPP electrochemically synthesized and deposited using 30 CV cycles on an FTO electrode from solutions containing 100% dichloromethane (a) or 95:5 dichloromethane and pyridine (b) compared to a TAPP film which was deposited onto an FTO electrode by

sublimating the TAPP monomer under vacuum (0.1 mm Hg) at 450 °C. Figure 31

(c) compares the FT-IR spectra for both electrochemically deposited poly-TAPP films.

Films obtained from solutions containing only dichloromethane showed continued electroactivity through 30 CV cycles, while electrode passivation was observed for the poly-TAPP deposited from solutions containing pyridine.

(a)

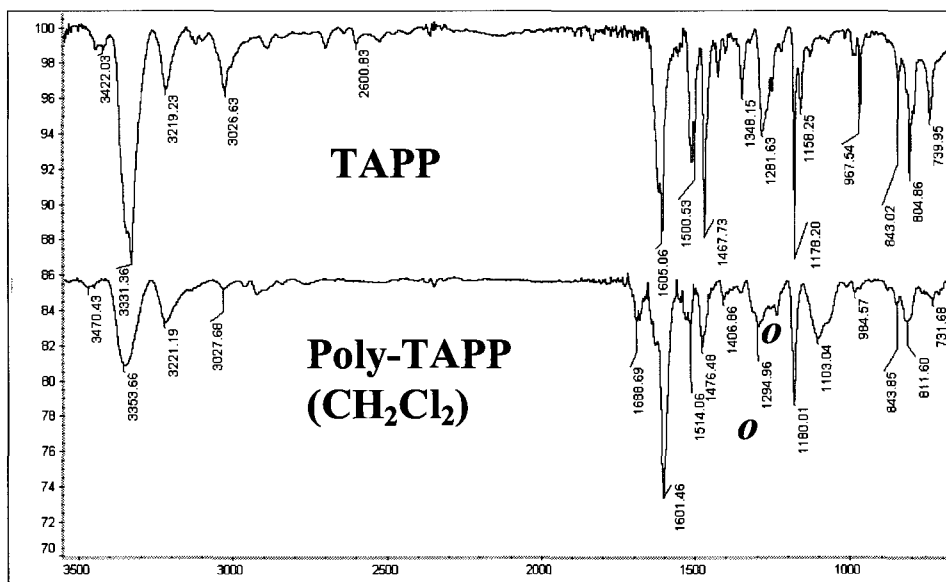


Figure 31. (a) Reflectance FT-IR spectra for evaporated TAPP onto FTO electrode and poly-TAPP from 100% dichloromethane electrochemical solutions (o – peaks attributable to dihydrophenazine)

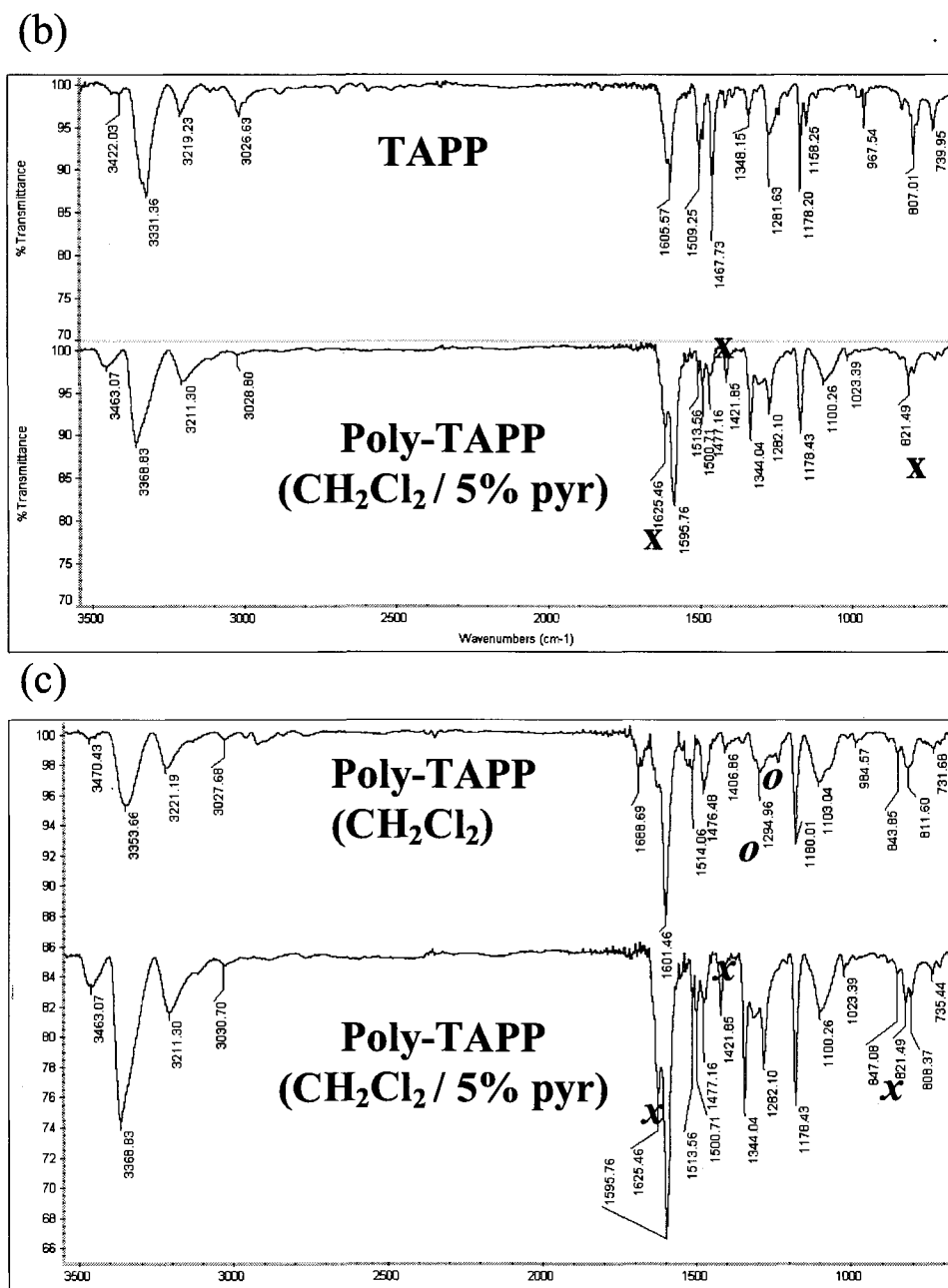


Figure 31. (b) Reflectance FT-IR spectra for evaporated TAPP and poly-TAPP from 95:5 dichloromethane and pyridine, (c) comparisons of both types of poly-TAPP films **x** – peaks attributable to phenazine

o – peaks attributable to dihydrophenazine

All three spectra show intense bands due to the symmetrical and asymmetrical vibrations of the amino groups ($\nu = 3331 - 3470 \text{ cm}^{-1}$) with strong amino deformations ($\nu = \sim 1600 \text{ cm}^{-1}$) and the N-H porphyrin pyrrole nitrogens ($\nu = 3211 \text{ cm}^{-1}$) [47]. Interestingly, the aminophenyl absorbances for both poly-TAPP films are shifted and slightly broadened slightly compared to the sublimed monomer film. A similar trend was noted in polyaniline films where weakened and shifted aminophenyl N-H absorbances around 3370 cm^{-1} were assigned to different types of intra- and intermolecular hydrogen bonding (N-H---N) and used to support hydrogen bonding between chains as an important contribution to the formation of nanostructured aniline oxidation products [94,135]. The aminophenyl shifts seen in the FT-IR spectra for poly-TAPP films also support interchain hydrogen bonding interactions with shifts of $41 - 48 \text{ cm}^{-1}$ for asymmetrical amino absorbances and $22 - 35 \text{ cm}^{-1}$ for symmetrical shifts with a decrease in the absorbance intensities in the films by half. In addition, these findings can support the proposal that tetrasubstituted aminophenylporphyrins have a greater chance than the diaminophenyl or triaminophenyl porphyrins for interchain hydrogen bonding and therefore supramolecular nanofiber formation.

Other characteristic absorbances for tetraphenylporphyrins include the tetrapyrrole macrocycle stretches which appear in the 1470 cm^{-1} thru 1500 cm^{-1} range, the in-plane C-H deformation bands of the pyrrole C-H at 1178 cm^{-1} , and surprisingly a possible TPP^+ radical cation vibrational mode at 1280 cm^{-1} which is present in all spectra [139,140]. Poly-TAPP film spectra contain several unique signature IR bands

indicating the presence of dihydrophenazine and phenazine structures. In the passivated poly-TAPP films a weak band is present at 820 cm^{-1} which is unique skeletal vibration of an aromatic phenazine nitrogen ring system and is typically one of the strongest absorptions observed in the IR spectrum of phenazine. [141] In addition, this skeletal deformation peak is present in all phenazine conjugated systems, is independent of the substitution on the phenazine ring and does not appear in the spectrum of dihydrophenazine [142]. Another new strong absorbance in the passivated poly-TAPP spectrum is the band at 1625 cm^{-1} located on the shoulder of the amino deformation band at 1595 cm^{-1} indicating the unique C=C and C=N stretching of the phenazine ring. Lastly, the peak at 1421 cm^{-1} can be associated with the multiple bond stretching of the C-N=C component of the phenazine linking group which does not appear in the conductive poly-TAPP samples. The bands at 1421 cm^{-1} and 1620 cm^{-1} have also been used to support the evidence of phenazine structures present in polyaniline films. [94,135] Evidence of a dihydrophenazine linkage in the conductive poly-TAPP samples is the C-NH-C stretching peak at 1294 cm^{-1} which is a very strong peak in the spectra of 5,10-dihydrophenazine. [141] Also characteristic for dihydrophenazine is a weaker absorbance around 1230 cm^{-1} which was assigned to the in-plane bending of dihydrophenazine C-H's. In summary, the variations in both poly-TAPP samples suggest the presence of phenazine linkages in the poly-TAPP deposited from solution containing pyridine which led to electrode passivation while

Poly-TAPP Nonconductive	Poly-TAPP Conductive	TAPP monomer	Assignment
3463	3470	3422	Asymmetrical – NH ₂
3368	3353	3331	Symmetrical – NH ₂
3211	3221	3219	Pyrrole – N-H
1625			C=C, C=N phenazine stretch
1595	1601	1605	Amino N-H - deformation
1513	1514	1514	Tetrapyrrole C-C-N-C
1477	1476	1467	Tetrapyrrole C-C-N-C
1421			C-N=C, phenazine stretch
1178	1180	1178	Beta pyrrole C-H deformation
	1294		C-NH-C, dihydrophenazine
1280	1280	1281	TPP ⁺ radical cation (?)
	1230		C-H, dihydrophenazine in-plane
1100	1103		Perchlorate anion, ClO₄⁻
821			Phenazine, skeletal vibrations
811	811	804	Disubstituted phenyl, out of plane
730	731	739	Disubstituted phenyl, out of plane

Table I: Infrared Frequencies (cm⁻¹) of poly-TAPP (both conductive and nonconductive forms) and TAPP monomer (solid) from reflectance FT-IR measurements

dihydrophenazine linkages were detected in films where the conductivity was sustained throughout the 30 CV cycle depositions. Table I lists absorbances for all three structures highlighting unique bands assigned to dihydrophenazine and phenazine structures present within the films.

3.8 Conductivity in Poly-TAPP

In order to oxidize additional TAPP monomer from solution, the poly-TAPP films deposited need to remain conductive during the electrochemical polymerization and deposition. Because of the electrochemical similarities with polyaniline, a conduction mechanism based on a bipolaron conduction pathway [143] can be used to describe the conductivity in poly-TAPP. Figure 32 depicts bipolaron movement along

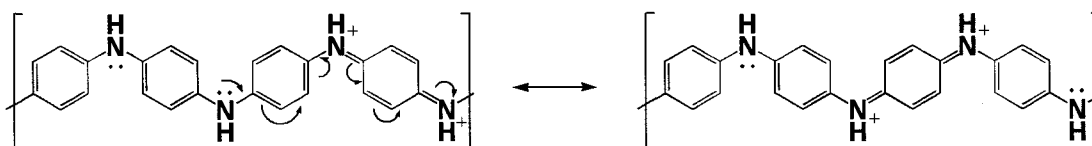


Figure 32. Polyaniline bipolaron conduction mechanism

the PANi polymer chain with charge transfer from the nitrogen lone pair through the nitrogen of the quinoid dication. Optimum conductivity occurs when the PANi chain is half-oxidized, with two neutral diphenylamine linkages for every quinoid dication structure to continue the electron pathway down the chain.

Using dihydrophenazine and protonated phenazine structures in an idealized linear poly-TAPP chain, a similar mechanism can be proposed for charge movement

between linked TAPP molecules. (Figure 33) For this mechanism to progress, a dihydrophenazine (or protonated phenazine, Figure 33 b) linking group must be present in order to continue bipolaron movement from the oxidized quinone form – highlighted bonds (Figure 33 a) to the reduced diamino form (Figure 33 c) assuming

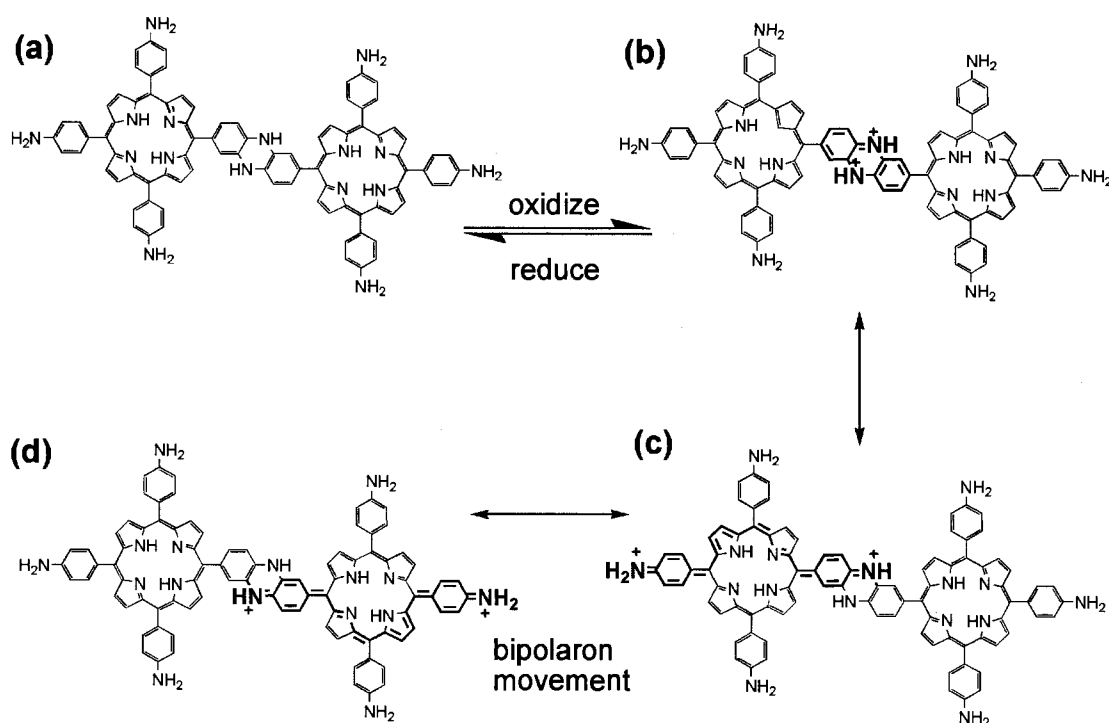


Figure 33. (a) Neutral dihydrophenazine TAPP dimer, (b) oxidized dimer ($2 e^-$) depicting new protonated phenazine linkage, (c) dimer resonance form with quinoid bipolaron form (highlighted bonds) and neutral diaminophenyl form, (d) bipolaron movement within dimer depicting the electron transfer and exchange

charge transport occurs from one porphyrin to the next. This mechanism implies bipolaron delocalization through the quinone and diamine units which is identical to

the charge transport in polyaniline. This simplistic approach does not take into consideration pathways involved with further oxidation of the aminophenyl substituents not contributing to the bonding in the polymer chain nor the effect protonation of the pyrrole nitrogens on the redox properties of the polymer. The pyrrole nitrogens can theoretically contribute to resonance structures similar to the delocalization of the diprotonated phenazine structure moved out to the reduced diaminophenyl nitrogens.

The proposed mechanism in Figure 33 indicates that deprotonation at the diprotonated phenazine structure intermediate would result in the formation of a phenazine linked polymer, which would limit conductivity through the TAPP linkages. A bipolaron would not move through a neutral phenazine linkage similar to the deprotonation of conductive polyaniline (emeraldine salt) which results in the non-conductive emeraldine base [144]. This mechanism fits nicely with reflectance FT-IR data showing the presence of phenazine linkages found in passivated, non-conductive poly-TAPP film samples. In addition, poly-TAPP films which were conductive after polymerization (i.e., showed electroactivity when running the film in fresh electrolyte and were oxidized at 0.7 V vs. Ag/AgCl for five minutes to ensure the correct oxidation state) were soaked in aqueous 5% NaOH solutions overnight became non-conductive and showed no electroactivity. In this scenario, the film was brought to the diprotonated phenazine linked structure, and after deprotonation to the neutral phenazine state, the film became nonconductive.

The quinone structures in Figures 33 (c, d) are crucial components of this TAPP dimer charge transfer mechanism and, similar to a hyperporphyrin structure, require a significant structural change in the TAPP macrocycle. Typically, tetraphenyl porphyrins have significant steric hindrance between hydrogens on the phenyl ortho and the pyrrole beta positions which cause the meso-substituted phenyl groups to twist out of the plane of the porphyrin macrocycle by about $61^\circ - 63^\circ$ [145].

Figure 34 shows several minimized (CHARMM) molecular structures of a TAPP dimer at the fully reduced phenazine (34a), the fully reduced dihydrophenazine (34b), and the fully oxidized dihydrophenazine (34c) indicating conjugation from the phenazine linkage group into both porphyrin macrocycles. From these models, the phenyl ring twist is observable in both the reduced structures while the planar (conductive) form of the TAPP dimer is shown in the oxidized state. A planar configuration between the porphyrin macrocycle and the meso-substituted phenyl group requires twisting of the pyrrole rings within the porphyrin macrocycle to adjust for the interacting phenyl and beta hydrogens. The oxidized, diprotonated porphyrin would also lose its $18 e^-$ aromatic character to account for the aminophenyl quinone structures.

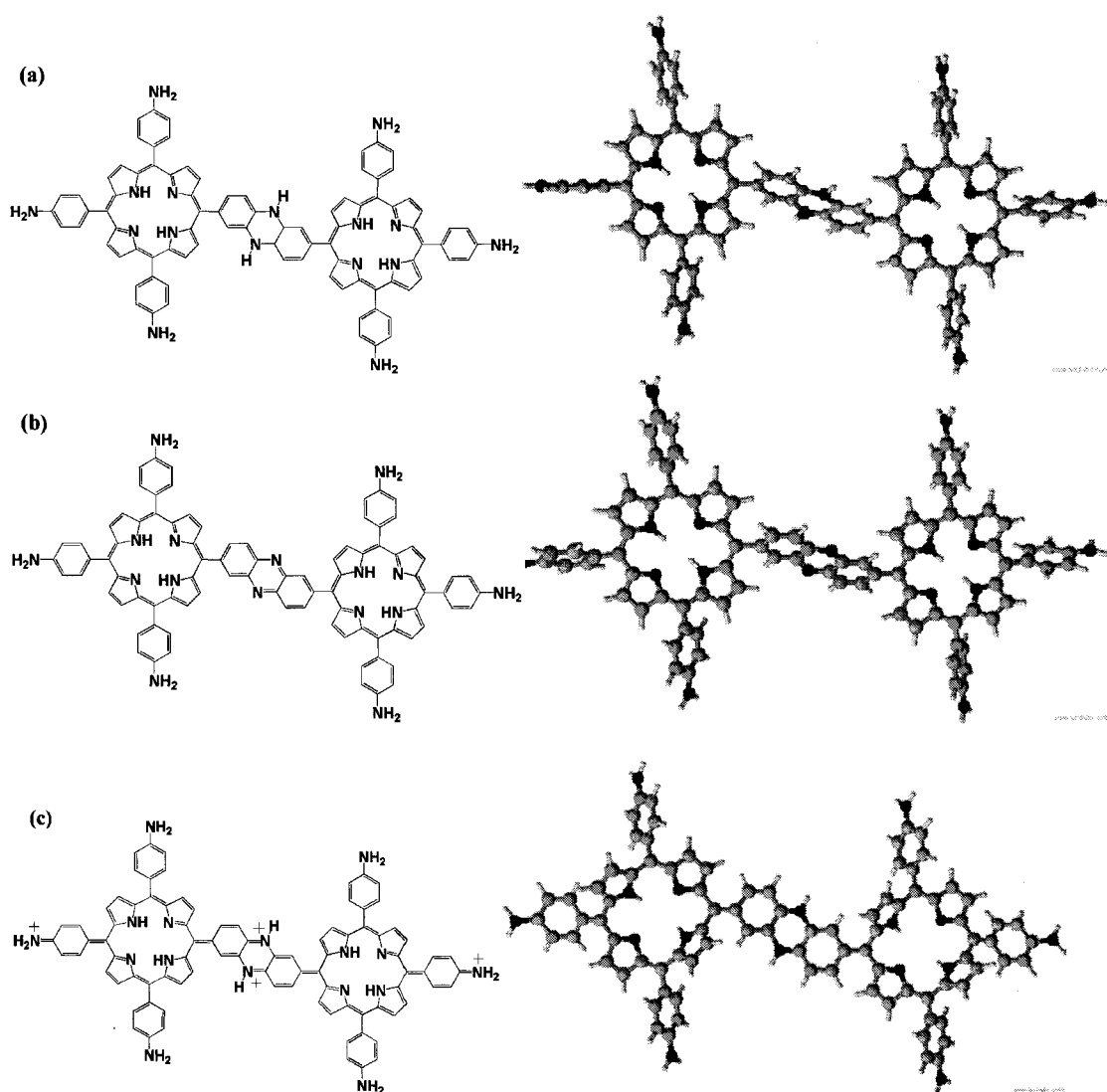


Figure 34. (a) Dihydrophenazine linked dimer with (CHARMM) minimized structure, (b) phenazine linked dimer, (c) fully oxidized (- 4 e⁻) dihydrophenazine dimer

Similar quinone forms of TAPP structures have been proposed for diprotonated hyperporphyrin involving π to π^* charge transfer excited states based

upon spectroscopic evidence of new bands in the 700 – 800 nm region [96,146] and upon H^1 NMR evidence [98]. During the protonation of the TAPP monomer (Figure 35a) in dichloromethane titrated with TFA, a significant red shift of the Soret band occurs from 427 to 460 nm accompanied by the disappearance of the Q-bands and the appearance of a new band at 728 nm. An excited state charge transfer occurs from the lone pairs of the aminophenyl nitrogen into the porphyrin macrocycle stabilizing the protonated interior pyrrole rings [147,148]. (Figure 35 b) The three spectra in Figure

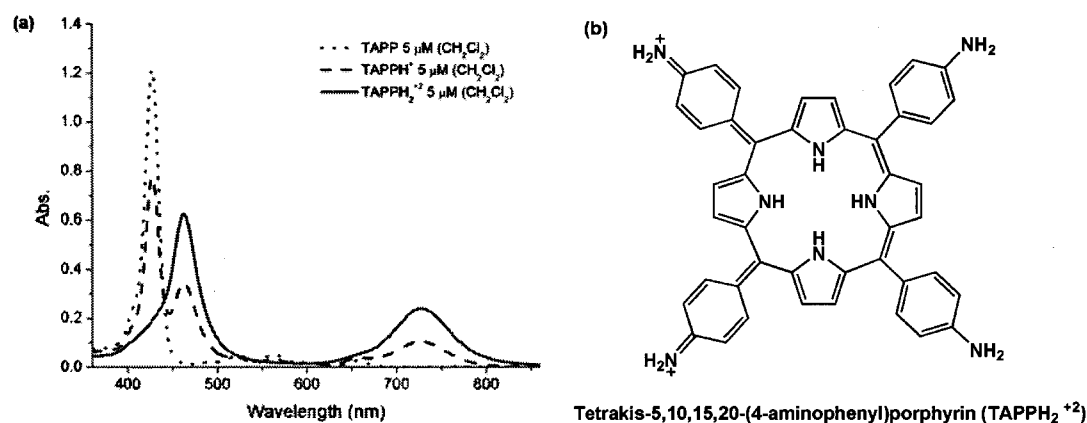


Figure 35. (a) TAPP, neutral, mix of neutral and diprotonated, and diprotonated in CH_2Cl_2 , (b) structure of the charge transfer excited state diprotonated TAPP

35a show various amounts of the diprotonated derivative with the middle spectrum showing a mixture of neutral TAPP and diprotonated TAPP. Spectral and H^1 NMR data have concluded that the monoprotinated derivative does not form during protonation [98].

It is reasonable to believe that comparable structures exist based on spectroelectrochemical measurements of poly-TAPP films at different applied oxidation levels in the range of the observed conductivity. Figure 36a shows similar absorptions in poly-TAPP films using spectroelectrochemical measurements and applying various oxidizing potentials to the film in a dichloromethane/TBAP solution. The charge transfer band which is typically detected around 760 nm for TAPP in solution can be observed in the absorption spectra with a broad absorption occurring at 780 – 800. This spectrum, however, does not completely match with the conductive, partially oxidized form of the poly-TAPP seen at +0.4 V applied potential, with a new broad band absorbance around 550 nm which is not accounted for in the diprotonated TAPP spectra. (Figure 35a) To account for the new bands observed in the poly-TAPP films, a titration of TAPP monomer was performed using ammonium persulfate to oxidize the monomer in solution. It has been demonstrated the TAPP does not electropolymerize in DMSO instead undergoing a reversible two-electron redox reaction, which can be detected in the UV-vis. Figure 36 (b) is a spectrum of TAPP monomer oxidized in DMSO using APS (reaction with 0.5, 0.75, and 1.0 equivalents of APS per TAPP). The oxidative titration spectra of TAPP match remarkably well with the oxidized film with absorbances appearing at 436 nm (porphyrin Soret peak) and new bands at ~550 nm and 750 nm. Since one equivalent of APS gives rise to a 2 e^- oxidation per TAPP molecule, this suggests that the most conductive, oxidized poly-TAPP film has similar absorption characteristics to the doubly oxidized TAPP.

Interestingly, the quinone form of the 2e⁻ oxidation product has two forms with either the cis or trans configuration shown in Figure 36c.

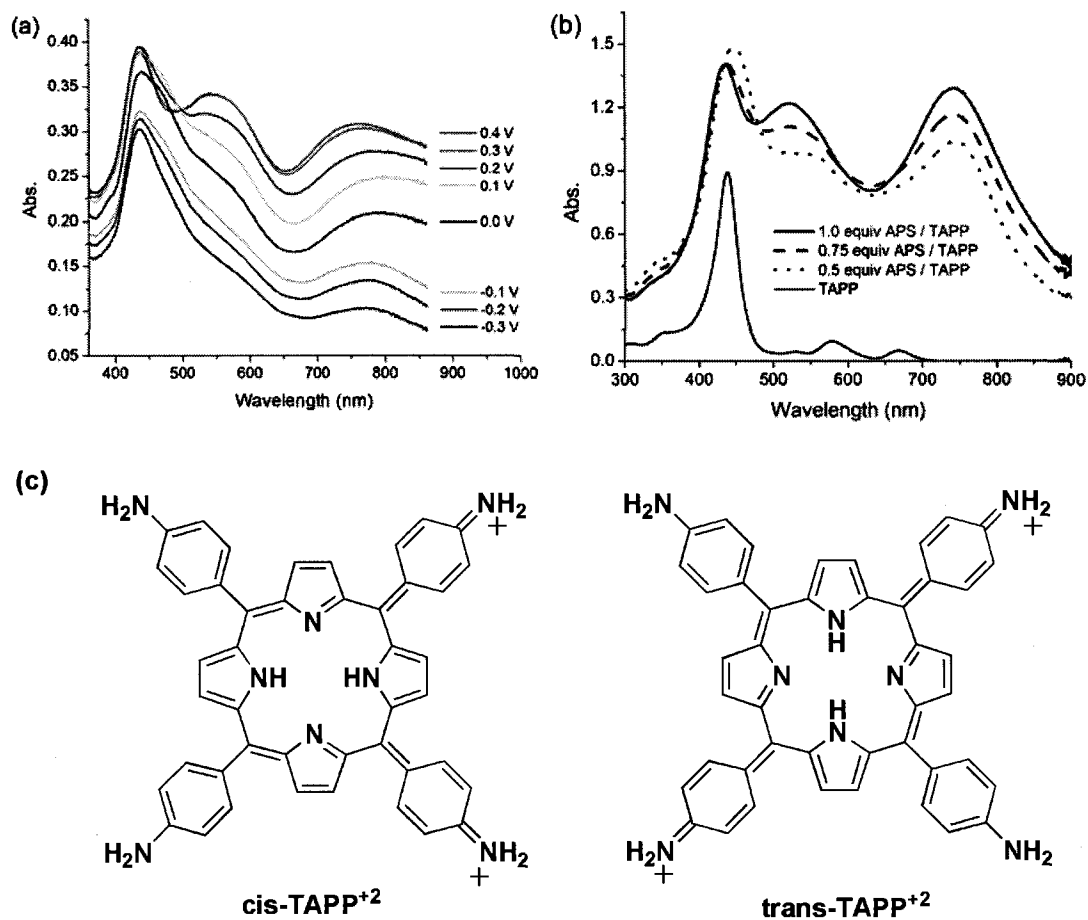


Figure 36. (a) Reversible spectroelectrochemistry of poly-TAPP film at potentials -0.3 V to +0.7 V vs. Ag/AgNO₃, (b) UV-vis spectra of TAPP oxidized in DMSO with APS, (c) Cis and trans quinone structures of oxidized TAPP⁺²

A similar reaction has been reported with the solution oxidation of a tetrasubstituted di(3,5-tert-butyl-4-hydroxyphenyl)porphyrin using m-

chloroperbenzoic acid resulting in the formation of a di-quinone which was air stable and could be reduced back to the porphyrin with aqueous sodium dithionite [149]. The oxidized TAPP solutions in DMSO were not stable and over time gradually become purple colored and then colorless, presumably an indication of porphyrin macrocycle decomposition.

The spectroelectrochemical spectra of poly-TAPP and the bands obtained from the oxidative titration of TAPP in DMSO with APS are consistent with structures like those proposed in Figure 36 (c). This evidence is in agreement with the observation that the addition of pyridine to the electrochemical solvent gradually induces film passivation suggesting deprotonation of oxidized dihydrophenazine structures. Diprotonated phenazine is a crucial structure in these mechanisms allowing for conductivity which proceeds through protonated di-quinone oxidized species and neutral diaminophenyl similar in scope to the half-oxidized structures of polyaniline [144].

3.9 Poly-TAPP Liquid Junction I^-/I_3^- Solar Cell

Photovoltaic activity of the poly-TAPP films, prior to incorporating PCBM or TiO_2 to fill in the nanoporous poly-TAPP electrode, were tested using an electrochemical solar cell with the standard liquid redox agent (I^-/I_3^-). Electrochemically deposited poly-TAPP was synthesized using either a 100% dichloromethane solution or a 5% pyridine/dichloromethane solution. The effect of the oxidation potential applied to the film after deposition was also examined by

applying a fixed potential for five minutes after deposition. Films were either left neutral or doped at the peak oxidation potential for the forward oxidation scan (0.75 mV vs. Ag/AgCl). Films were deposited from 3, 6, and 15 electrochemical cycles with a 30 s vertex delay resulting in a 400 – 500 nm thick film ($\sim 15 \text{ nmol/cm}^2$ average surface coverage). The redox agent (I^-/I_3^-) was dissolved in a 80:20 (w:w) solution of ethylene carbonate and propylene carbonate which did not dissolve poly-TAPP film. The cell was constructed by fixing the poly-TAPP coated FTO

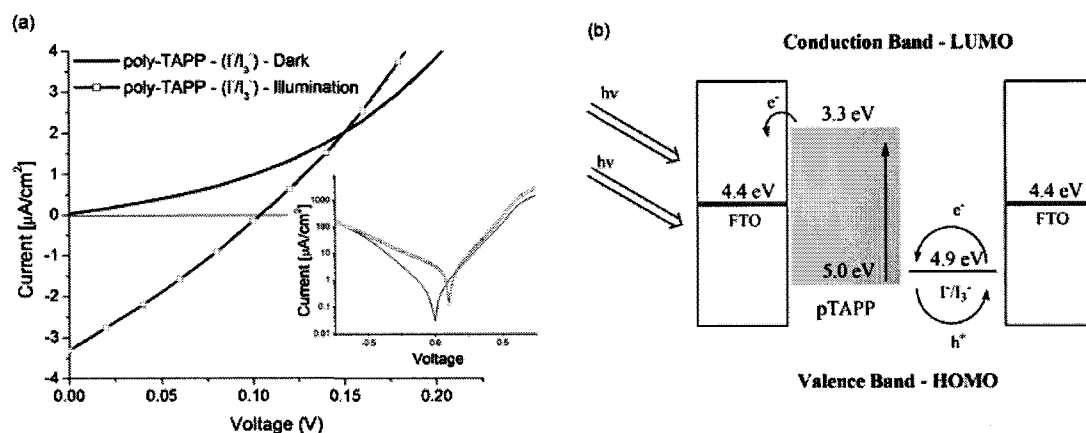


Figure 37. (a) Current-voltage characteristics of the poly-TAPP (15 CV scans, using 95:5 CH_2Cl_2 :pyridine) nanoporous electrochemical cell in the dark and under 100 mW/cm^2 illumination. Inset - log plot of data, (b) Energy diagram for the nanoporous solar cell with work function values for the contact FTO electrodes [150], I^-/I_3^- redox couple [151], and the HOMO/LUMO energy levels for the poly-TAPP film (estimated from those reported for TAPP [85])

electrode to a blank FTO electrode with a Surlyn film thermoplastic melted at 120°C

for five minutes. This provided a 5 - 10 μm channel which was filled with the liquid redox couple using capillary action. Figures 37 (a) and (b) show the current-voltage characteristics of a typical electrochemical poly-TAPP solar cell with relative energy levels of each component.

The highest occupied molecular orbital (HOMO) and lowest unoccupied molecular orbital (LUMO) were determined using the reversible oxidation/reduction waves of the deposited film determined using cyclic voltammetry. The HOMO was estimated at 5.0 eV relative to vacuum (Ag/AgCl is poised at ~ 4.7 eV relative to vacuum) using the ferrocene/ferrocenium redox couple to check the validity of the Ag/AgCl reference electrode using 0.35 V vs. Ag/AgCl for the $E_{1/2}$ of ferrocene.

This cell was constructed using a poly-TAPP electrode deposited from 15 electrochemical cycles from a 95:5 (v:v) pyridine/dichloromethane solution and was left in a non-oxidized form. The active area for the cell shown is 0.45 cm^2 with irradiation from a quartz halogen lamp (100 mW/cm^2). Under illumination a photovoltaic response of the poly-TAPP films is apparent with short-circuit current density values (I_{sc}) ranging from $1\text{--}3\text{ }\mu\text{A/cm}^2$ and V_{oc} of $100\text{--}120\text{ mV}$.

The poly-TAPP cell shows a fast on-off photocurrent response (Figure 38a) with values leveling off to $1\text{--}2\text{ }\mu\text{A/cm}^2$ after 1 hour of illumination. Figure 38 (b) shows a comparison of poly-TAPP films produced from solutions with pyridine and one produced with just dichloromethane. Current-voltage curves indicate slightly higher

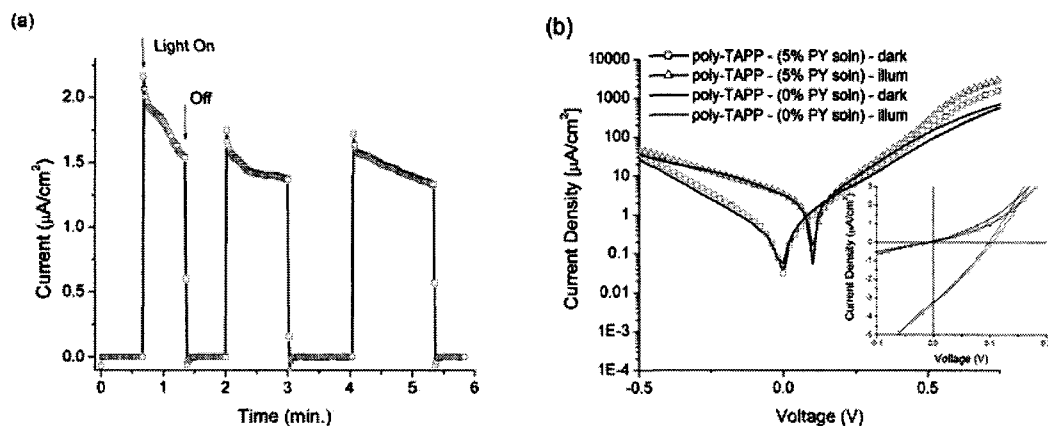


Figure 38. (a) On/off photocurrent response of the poly-TAPP electrochemical solar cell under 100 mW/cm^2 illumination. (b) Current-voltage comparison of solar cells using electrochemically deposited poly-TAPP films (15 cycles) obtained from solutions with and without 5% pyridine in the electropolymerization solution

V_{oc} and I_{sc} values using poly-TAPP film that has been electrochemically deposited from solutions containing 5% pyridine over those from 100% dichloromethane.

Overall performance of the two types of films are almost identical considering film thickness for poly-TAPP with pyridine were typically 30 - 50 nm thicker than poly-TAPP deposited without using pyridine. It is not completely surprising that both films show similar photovoltaic characteristics considering that both films are in their non-conductive state and showed similar surface coverage. Holes and electrons in such films will presumably migrate as has been demonstrated previously with associated hopping mechanisms between adjacent porphyrin sites and polymer chains [152].

Excitons generated in the films are presumed to migrate to the FTO electrode-poly-

TAPP interface and dissociate with I^-/I_3^- redox couple providing electrons back to the oxidized film. Table II summarizes the results of poly-TAPP films tested using the I^-/I_3^- redox shuttle. Photocurrents generated from this device are much lower than those observed for DSSCs which use a monolayer of dye coated onto a high surface area TiO_2 electrode. The solar cell properties indicate that the film thickness and surface coverage affect the observed I_{sc} ($\mu\text{A}/\text{cm}^2$) photocurrent and V_{oc} (mV). In general, photocurrent was greater with neutral poly-TAPP films deposited from 15 CV cycles. This is somewhat surprising considering that excitons can typically only diffuse 10-15 nm before recombination. It is inferred that increases in the observed photocurrent are primarily a result of greater surface coverage of the FTO electrode rather than increased overall film thickness. The photoactivity does suggest that the poly-TAPP film allows for good hole mobility away from the interface of the poly-TAPP and the FTO electrode back to the liquid redox couple.

When oxidized (doped) poly-TAPP films were evaluated in a liquid junction solar cell, the devices performed less efficiently, averaging half the photocurrent observed with films that were not doped ($I_{\text{sc}} = 1.7 \mu\text{A}/\text{cm}^2$, $V_{\text{oc}} = 77 \text{ mV}$ average of four devices). Free charge carriers generated at interfaces within molecular semiconductor films upon light absorption can become trapped in sites within the polymer matrix. Oxidation within the poly-TAPP films leads to higher overall conductivity, but also leads to a higher trap density within the films ultimately limiting photocurrent generation [153]. This might explain why the IV curves are dissimilar under illumination but cannot account for the IV curves observed in the dark. Among

the doped films, poly-TAPP (from pyridine) performed much better than films produced from solutions containing just dichloromethane. (Table II) One possible

Poly-TAPP Film (Synthesis Cond.)	*I_{sc} ($\mu\text{A}/\text{cm}^{-2}$)	*V_{oc} (V)	FF	η_{eff} (%) ($\times 10^{-5}$ %)
Poly-TAPP, doped 0% pyridine	1.87	0.08	0.26	4.1
Poly-TAPP, doped 5% pyridine	1.69	0.08	0.27	4.1
Poly-TAPP, neutral 0% pyridine	2.73	0.09	0.28	6.8
Poly-TAPP, neutral 5% pyridine	3.30	0.1	0.28	9.5
Poly-TAPP from 6 CV cycles, neutral 5% pyridine	0.79	0.08	0.28	1.7

Table II. Poly-TAPP films tested (*average data of 3 devices for each condition) under $100 \text{ mW}/\text{cm}^2$ using $(\text{I}^-/\text{I}_3^-)$ liquid redox shuttle with all films synthesized from 15 electrochemical CV cycles with $\sim 5 \mu\text{M}$ device thickness from heat treated Surlyn film spacers

explanation is that poly-TAPP films (from pyridine containing solutions) which

became electro-inactive after the 10th CV cycle during the polymerization process were not effectively electrochemically doped. As was noted previously, films produced using pyridine and >15 CV cycles exhibited little characteristic charge transfer bands common in the doped form of the polymers. It is reasonable to believe that the passivated film was oxidized to a lesser degree than poly-TAPP generated and deposited using solutions not containing pyridine.

In summary, primary charge separation in a liquid junction poly-TAPP – (I/I₃⁺) solar cell occurs where excitons reach an interface with poly-TAPP/FTO is limited. Taking advantage of the high surface area of poly-TAPP would require better interfacial charge separation than can be provided by the (I/I₃⁺) redox couple.

3.10 PCBM Incorporated Poly-TAPP Excitonic Solar Cell

Organic solar cells have strict requirements for exciton creation, exciton mobility, charge separation, and charge mobility [154]. The limitations of charge mobility in thin porphyrin films have been reported [155] and are an important consideration when designing solar cell devices that incorporate these materials. Utilizing the highly nanofibrous morphology of poly-TAPP requires the use of materials which can allow for contact with a majority of the poly-TAPP surface area creating an interfacial geometry which allows for shorter exciton path lengths to and from interfaces within the device. Using these basic concepts, the nanostructured poly-TAPP fulfills the role of structure-directing agent, light absorber, and considering its relative band levels, p-type hole conductor in an excitonic solar cell. The small

molecule n-type material (PCBM) is a good candidate for completing the solar cell because of its solubility/processability and good electron accepting ability [156]. Therefore, PCBM was infiltrated into the porous poly-TAPP by dissolving the material in chlorobenzene (2% wt.), applying a thin film on top of the poly-TAPP electrode by using a glass capillary to coat the surface, and allowing the film to dry slowly under ambient conditions. A LiF/Al metal electrode was evaporated on top of the active poly-TAPP/PCBM layer to complete the device. The potential energy level diagrams of the resulting solar cell devices are depicted in Figure 39 using literature values obtained for PCBM [13] and poly-TAPP band levels obtained from cyclic voltammetry [111].

The HOMO/LUMO band energies for poly-TAPP from cyclic voltammetry indicate a 1.7 eV band gap with the HOMO level at 5.0 eV and LUMO at 3.3 eV. The poly-TAPP LUMO band energy is offset with the PCBM - LUMO (4.1 eV) by 0.8 eV which is more than the minimum 0.3 – 0.4 eV required for exciton dissociation [14,157] and charge transfer from the photoexcited poly-TAPP to the PCBM. Figure 39 (c, d) also depicts the device geometries and approximate cross-sectional active area of an excitonic solar cell using the nanofibrous porphyrin polymer layer.

Constructing a device such as that depicted in Figure 39 (d) presents several challenges to deposit the top contact onto the active layer. It is a common problem when building devices with active layers around 100 – 200 nm to “short circuit” the device from either pinholes in the film itself, or metal contacts overlapping off the side

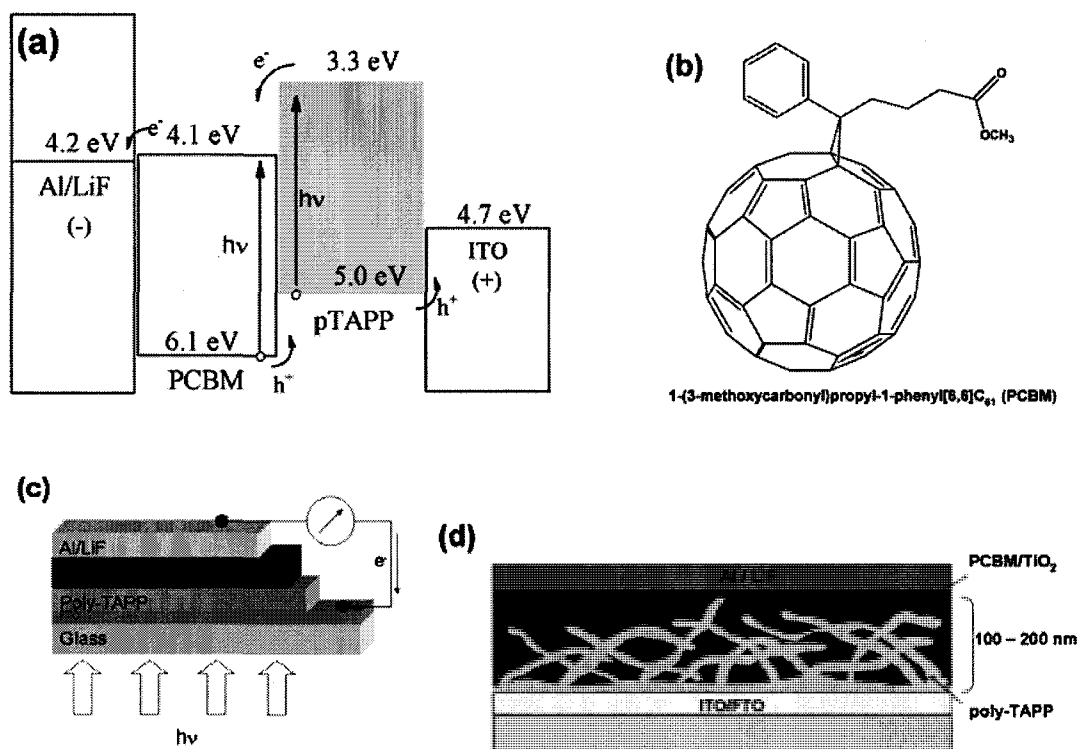


Figure 39. (a) Potential energy diagram of poly-TAPP incorporated with, (b) 1-(3-methoxycarbonyl)propyl-1-phenyl[6,6]C₆₁ (PCBM), (c) Poly-TAPP – PCBM or TiO₂ device geometry with (d) interfacial nanofibrous photoactive layer schematic, yellow poly-TAPP nanofibers with brown PCBM incorporation

of the photoactive layer and making contact with the underlying FTO electrode. The poly-TAPP layer also presents an extraordinarily rough, nanostructured surface making it quite difficult to make good electrical contact with the high surface area. Therefore, efforts were made to coat the poly-TAPP nanofibers so that the metal electrode did not contact the top of poly-TAPP film, i.e., the fibers were not exposed through the deposited PCBM layer. This was to prevent recombination of holes migrating through the poly-TAPP layer with electrons injected into the deposited

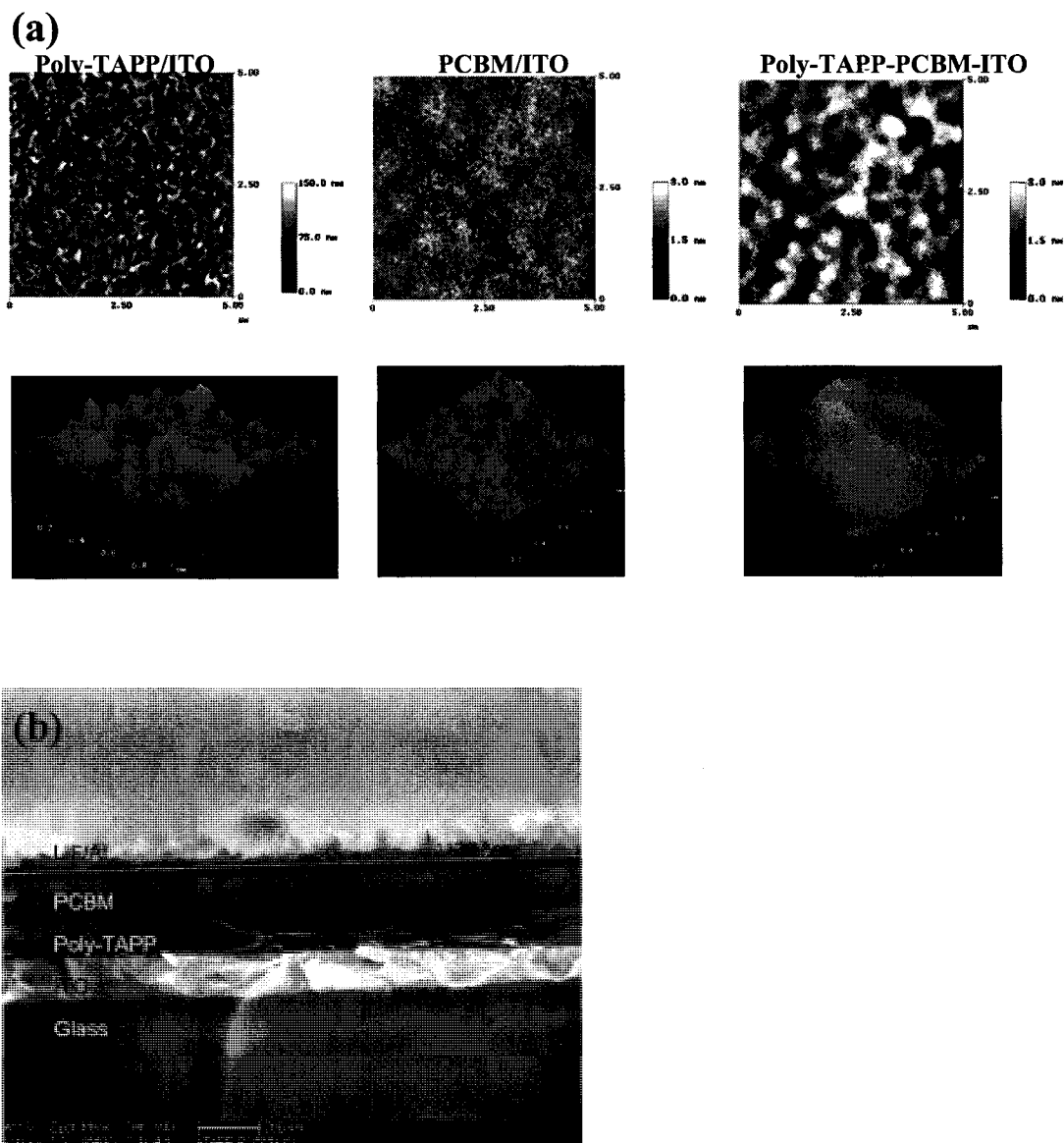


Figure 40. (a) AFM images of poly-TAPP deposited from 3 CV cycles onto an ITO electrode using 5% pyridine. Also shown is the AFM images of PCBM applied from a 2% wt. chlorobenzene solution to a blank ITO and to the top surface of a poly-TAPP electrode (both scale bars are 3 nm), (b) SEM cross-section of the poly-TAPP/PCBM organic solar cell with each layer identified

aluminum back contact. Atomic force microscopy was used to image the deposited poly-TAPP nanofibers before and after application of the drop-cast PCBM layer to ensure complete coverage of the nanostructured film. The morphologies of these surfaces are shown in the AFM images in Figure 40. The first AFM image reveals the poly-TAPP morphology after deposition onto an ITO conductive electrode. The expected nanofibrous surface is visible and indicates a rough surface morphology (scale bar to the right is at 150 nm surface roughness). The second image is a PCBM film coated onto the surface of a clean ITO electrode in order to demonstrate what this surface might look like when coating a completely flat surface (3 nm surface roughness). The last AFM shows the PCBM incorporated onto the poly-TAPP surface and again shows a smooth surface with no poly-TAPP nanostructured features protruding through the PCBM layer (3 nm scale bar). The surface has some “wavy” surface characteristics; however it is considerably smoother than the poly-TAPP nanofibrous electrode. Because of the smooth surface, the evaporated metal electrode can be deposited uniformly while making good contact to the PCBM layer, and electrically to the poly-TAPP nanofibers. SEM cross sections of the finished devices show complete coverage of the poly-TAPP film with some of the poly-TAPP nanostructure visible near the surface of the ITO electrode (bottom). (Figure 40 b)

The UV-vis characteristics of the completed films are shown in Figure 41 (a) with photoluminescence of the poly-TAPP films and TAPP monomer shown in Figure 41 (b). PCBM also absorbs in the 400 nm range and is theorized to contribute to photocurrent in conjugated polymer-PCBM organic solar cells [158]. The combined

poly-TAPP-PCBM film shows the broad combined absorbances in the 400 – 600 nm range with a detectable Soret peak in the poly-TAPP film/PCBM combination spectra.

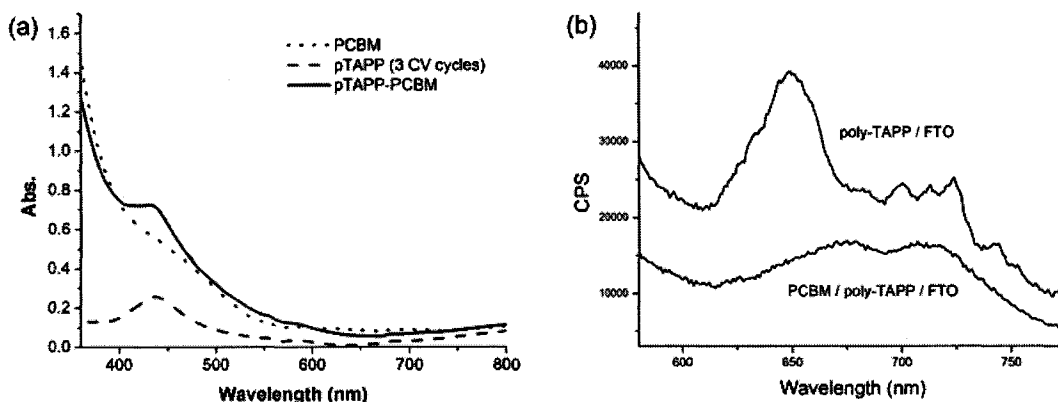


Figure 41. (a) UV-vis spectra of poly-TAPP film, PCBM, and incorporated poly-TAPP/PCBM (b) Photoluminescence spectra of poly-TAPP film and poly-TAPP with PCBM

The fluorescence of poly-TAPP films is very weak, presumably from internal quenching within the film leading to possible energy transfer to the FTO electrode. This was observed for similar aminophenyl containing, electropolymerized porphyrin polymers deposited onto ITO electrodes and was attributed to quenching mechanisms leading to charge transfer to the ITO surface [100]. The quenching due to the addition of the PCBM layer is not conclusive that a charge transfer mechanism is present between poly-TAPP and PCBM layers; however it does indicate some interaction between the two materials. Supporting this interaction is the relative band energies for

both materials which favor charge transfer from the poly-TAPP to the PCBM layer and the fact that PCBM is a well known electron acceptor for organic solar cells [156].

The photovoltaic properties of the poly-TAPP films were evaluated by varying the film thickness of the poly-TAPP using 1, 3, or 6 CV cycles (with a 30 s vertex delay) and the conditions used for electrodepositing films using either entirely dichloromethane solutions or solutions with 5% added pyridine to enhance the nanostructured features of the devices. Figure 42 shows current-voltage curves for the poly-TAPP devices with film thickness variations (Figure 42 b) and the effect of using poly-TAPP which had been deposited from 3 CV cycles which did not contain pyridine (Figure 42 a), or 3 CV cycles which contained 5% pyridine (Figure 42 c). Figure 42d compares the current-voltage curves poly-TAPP – PCBM solar cells using poly-TAPP obtained from both electrochemical solvent conditions under illumination. From these measurements, it is interesting to note that films that were synthesized without pyridine that led to more conductive porphyrin films were found to have higher photocurrents and in general, have a lower series resistance through the device. Devices utilizing poly-TAPP films which used pyridine in their synthesis exhibited higher V_{oc} but with half the photocurrent. Although the films were not in their most conductive states, it appears that hole mobility is decreased in films which passivated more quickly during the electrochemical synthesis.

The trend of thicker poly-TAPP films increasing the observed photocurrent while decreasing the V_{oc} is in agreement with might be expected when more charge carriers generated from a thicker light absorbing layer occur while at the same time

increasing series resistance within the cell resulting a drop in voltage [159]. For these types of devices, a thickness of 3 CV cycles, approximately 80 – 100 nm thick

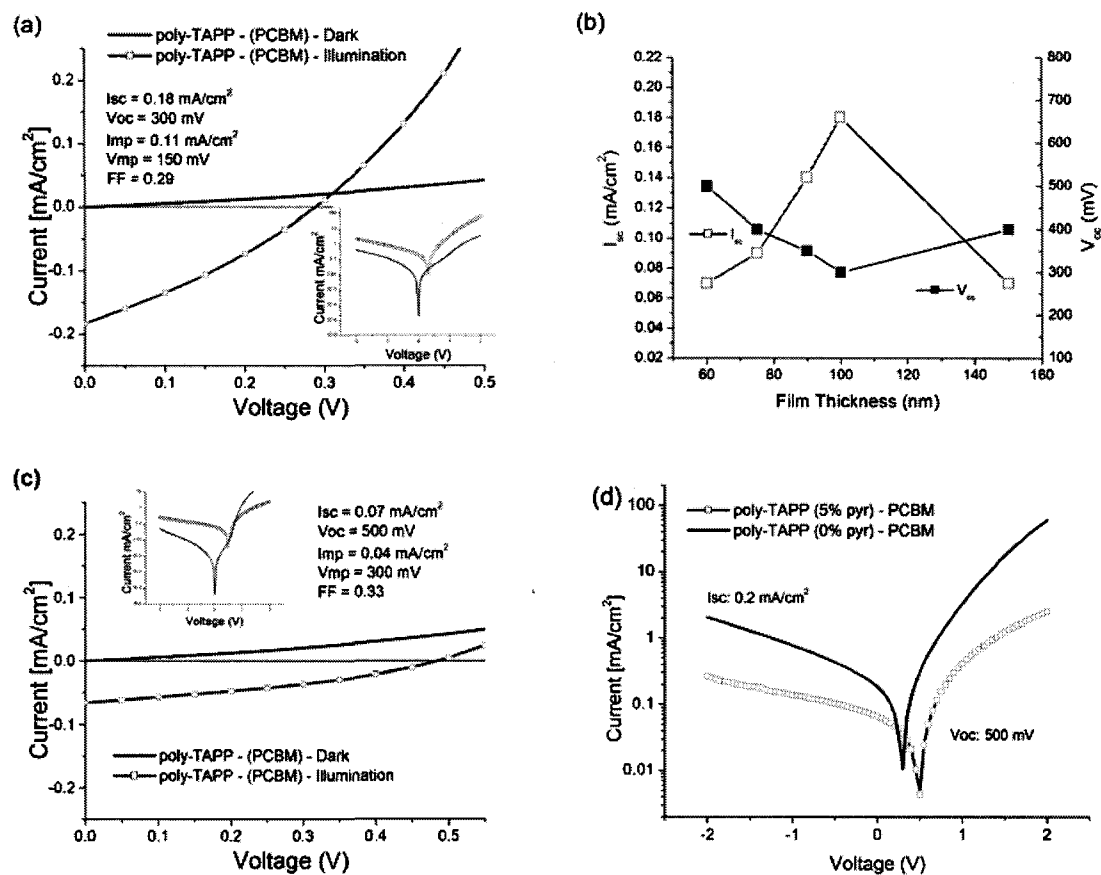


Figure 42. (a) Poly-TAPP – PCBM film using a poly-TAPP film deposited from 3 CV cycles using solutions containing no pyridine in the electrochemical solvent, (b) film thickness variations, (c) poly-TAPP (3 CV cycles) using 5% pyridine in the electrochemical deposition, (d) photocurrent comparison between conditions from (a) and (c)

Poly-TAPP Film (Synthesis Cond.), with PCBM	*I_{sc} (mA/cm⁻²)	*V_{oc} (V)	FF	η_{eff} (%)
Poly-TAPP 1 CV scan, 0% pyridine	0.12	0.41	0.29	0.01
Poly-TAPP 1 CV scan, 5% pyridine	0.14	0.35	0.26	0.01
Poly-TAPP 3 CV scans, 0% pyridine	0.18	0.31	0.29	0.02
Poly-TAPP 3 CV scans, 5% pyridine	0.11	0.50	0.29	0.01
Poly-TAPP 6 CV scans, 5% pyridine	0.07	0.40	0.31	0.008

Table III. Poly-TAPP - organic solar cell devices tested under 100 mW/cm² using PCBM incorporated from 2% chlorobenzene solutions and Al/LiF top electrode (*average data for three runs under each condition)

was optimal for obtaining a V_{oc} of 300 mV with generated photocurrent as high as 0.18 mA/cm^2 . Table III summarizes all the conditions, film thickness (# of CV cycles), and resulting efficiencies for the poly-TAPP – PCBM organic solar cells. Overall, efficiencies for devices constructed using 1 – 3 CV cycles for deposition remained low with $\eta_{eff} (\%) \sim 0.01 - 0.02$ under 100 mW/cm^2 illumination.

The poly-TAPP and the PCBM components were also tested individually in a solar cell. Poly-TAPP was grown on ITO glass electrodes using 3 CV cycles with a “set” potential scan at 500 mV. PCBM was applied using the same casting and evaporation method to a clean ITO electrode. Both cells were completed by evaporating LiF-Al. The current voltage plots show the light/dark curves (Figure 43) for the cells built with just poly-TAPP, just PCBM, and the combined solar cell device under illumination.

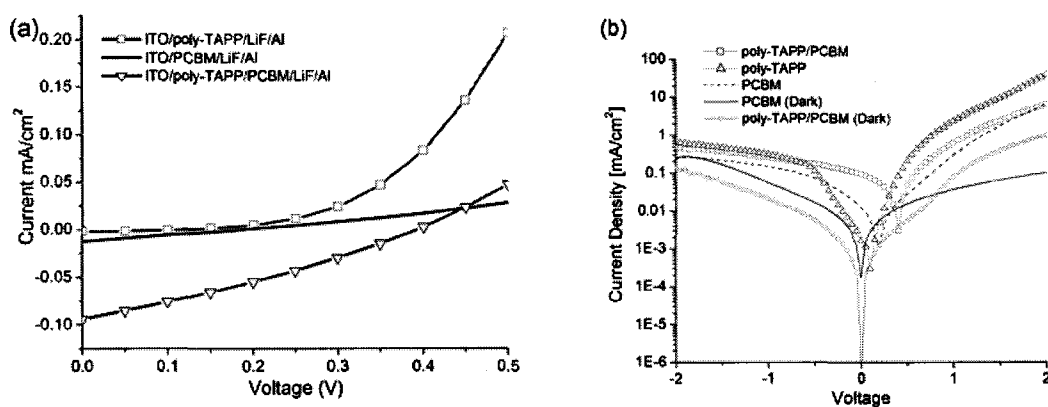


Figure 43. (a) Poly-TAPP, PCBM, and combination poly-TAPP – PCBM solar cells, (b) Current – voltage log plot curves in the dark and under illumination

The graphs show a steep photoconductivity increase for device constructed of just the poly-TAPP film with minimal V_{oc} and I_{sc} observed. The metal LiF/Al interface to the porphyrin polymer film is considered non-uniform because of the nanofibrous structures of the poly-TAPP film surface. The smooth nature of the deposited PCBM film makes good contact with the evaporated LiF/Al metal layer but makes poor contact to the clean ITO substrate. The PCBM layer exhibits a small V_{oc} and I_{sc} under illumination and does not perform as well as the combination solar cell. The poly-TAPP/PCBM solar cell combines the advantages of both morphologies creating a good physical to the top and bottom electrical contact electrodes used.

Finally, the spectral response (incident photon to current efficiency %IPCE) of one the best performing devices was tested ($\eta_{eff} (\%) = 0.02\%$). (Figure 44) This graph indicates that both the poly-TAPP and the PCBM layer contribute to the photocurrent with an increase in performance throughout the Q-band region and notable contribution from the PCBM layer below 450 nm where the poly-TAPP film has a decreased molar absorptivity. The spectral response which is somewhat restricted due to the thin poly-TAPP layer and the absorbances of both materials in the 400 – 500 nm range gives some indications why the efficiencies of these devices are limited. Increasing the absorbance further into the lower band gap region would presumably increase the photogenerated current. In addition, the limitations using porphyrin polymers for hole transport in solar cells have been reported, [80,152,154,155] and are important when considering if poly-TAPP is a good candidate as a hole transport material for organic solar cells. However, the photovoltaic activity observed in the

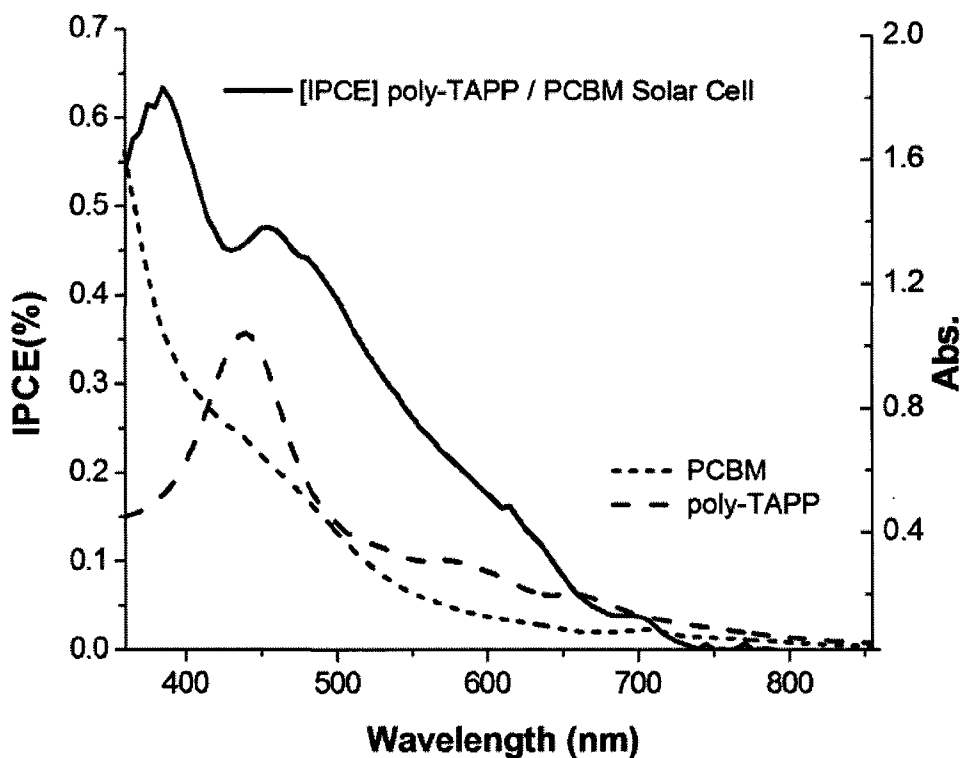


Figure 44. Incident to photon current efficiencies (IPCE %) for a poly-TAPP – PCBM solar cell constructed with electrochemically deposited poly-TAPP (3 CV cycles) and a drop cast film of PCBM ~ 200 nm. Also shown are the absorption spectra of PCBM and poly-TAPP.

devices constructed does strongly suggest that poly-TAPP is responding as a light absorbing layer and hole transport material. The increasing photocurrent with increasing poly-TAPP film thickness, the IPCE spectral response, and the individual component solar cell tests all support the evidence of the importance of using poly-TAPP nanostructured films in this capacity for a PCBM containing organic solar cell.

3.11 Poly-TAPP Inverse TiO₂ DSSC

The design for an inverse dye-sensitized solar cell device using the poly-TAPP nanofibrous morphology was envisioned using the poly-TAPP scaffold as a porous, interpenetrating network to direct the deposition of a TiO₂ electron acceptor layer. Additionally, the free aminophenyl groups available on the surface of the poly-TAPP film can react with additional dyes or materials that could eventually allow for the donor material to be created in the pores. A good candidate, tetrakis(4-carboxyphenyl)porphyrin (TCPP) can serve as an efficient dye [50], donating excited electrons to the thin layer of deposited TiO₂ with the poly-TAPP serving as hole transporter. Figure 45 shows the steps involved for this photovoltaic process and the relative band energies of each material used in an inverse DSSC including TiO₂, TCPP, and poly-TAPP [111]. From the relative positions of the HOMO/LUMO levels

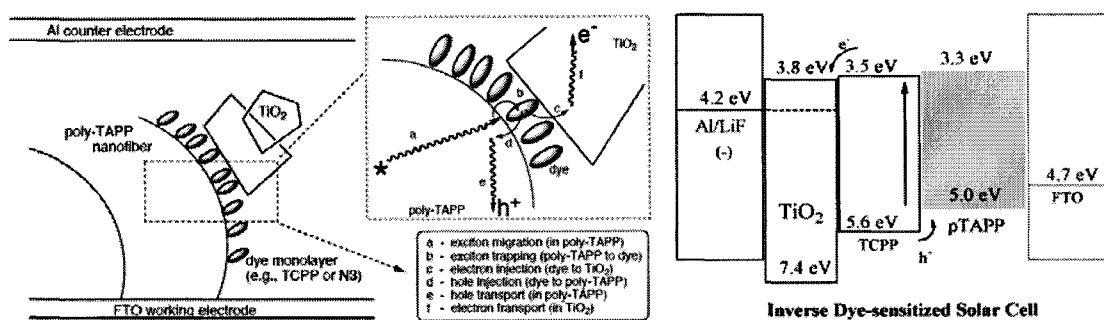


Figure 45. (a) Steps involved in the photoinduced charge separation, using a TCPP dye layer with holes migrating in the poly-TAPP layer and electrons migrating through the TiO₂ layer, (b) Energy level diagram with the relative band energies of the various components of a porphyrin inverse DSSC

of each porphyrin layer, it is apparent that photoexcitation of either the poly-TAPP layer or the TCPP layer can contribute to the generated photocurrent. Complete coverage of the poly-TAPP layer is not absolutely critical because both layers can theoretically serve as the interface with TiO_2 to initiate exciton dissociation.

The single layer of TCPP dye is chemisorbed onto the poly-TAPP surface using the tetra-acid chloride TCCPP in CH_2Cl_2 to form amide bonds with the help of a pyridine catalyst. (Figure 46) This coating also allows for the TCCPP porphyrin to react with the FTO surface and act as an insulator which will cover any areas of the FTO electrode that is not already covered by the poly-TAPP film. This step not only generates an additional light absorbing layer, it allows for the electrical insulation of areas on the poly-TAPP electrode where the film may be too thin or areas where the underlying FTO layer is exposed helping to avoid a short circuit situation.

Additionally, this derivatization gives a new carboxylic acid surface feature that the nano-particulate TiO_2 film will “see” when incorporation is performed. Carboxylic acid functional groups are typically present on many dyes used in typical DSSCs as an anchor for the dye onto the TiO_2 surface [64]. TCPP may be singly or doubly bonded to the surface of the poly-TAPP film, leaving two or three carboxylic acid groups available for interaction with the developing TiO_2 layer. Similar methods have been used previously for the formation of simple amide bond formation between TCCPP and TAPP to form interfacial films [160]. Figure 46 depicts the preparation of TCCPP and the derivatization of the poly-TAPP surface catalyzed by pyridine. The film is

rinsed with organic solvents and then water to remove excess reactants and convert excess acid chlorides to carboxylic acids.

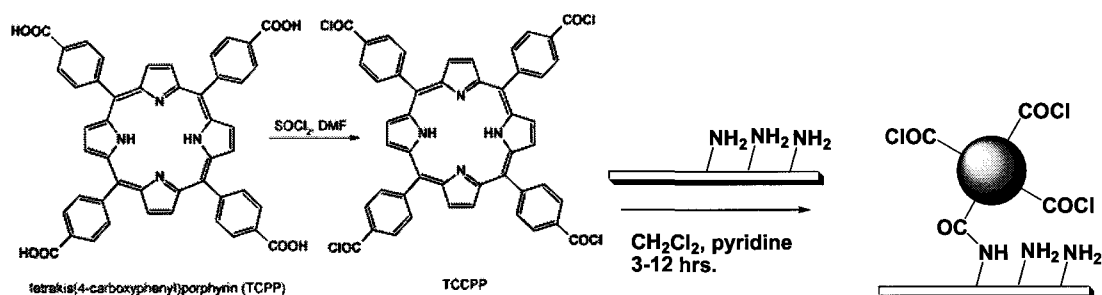


Figure 46. Preparation of TCCPP and surface reaction with poly-TAPP

Poly-TAPP films treated with TCCPP showed a strong increase in the absorption of the Soret band at 423 nm as well as those of the Q-bands located in the mid-visible range around 500-600 nm. Figure 47 shows a poly-TAPP film reacted for 6 hrs using the conditions described above. Soaking for longer than 6 hr did not increase the amount of porphyrin which could be reacted with the surface. From the UV-vis spectrum (Figure 47), it was calculated that the porphyrin surface coverage increased from 5.6 to 7.8 nmol/cm². To ensure that non-covalently bound TCPP was removed, films were soaked in ethanol overnight and rinsed thoroughly with dichloromethane.

The next important step in constructing the inverse dye-sensitized solar cell involves the incorporation of TiO_2 into the nanoporous poly-TAPP film. There exists a significant volume of literature devoted to coating polymer nanofibers with TiO_2 with a wide variety of TiO_2 precursors and deposition methods [161-163]. Several approaches were initially investigated for TiO_2 incorporation. The first was simply

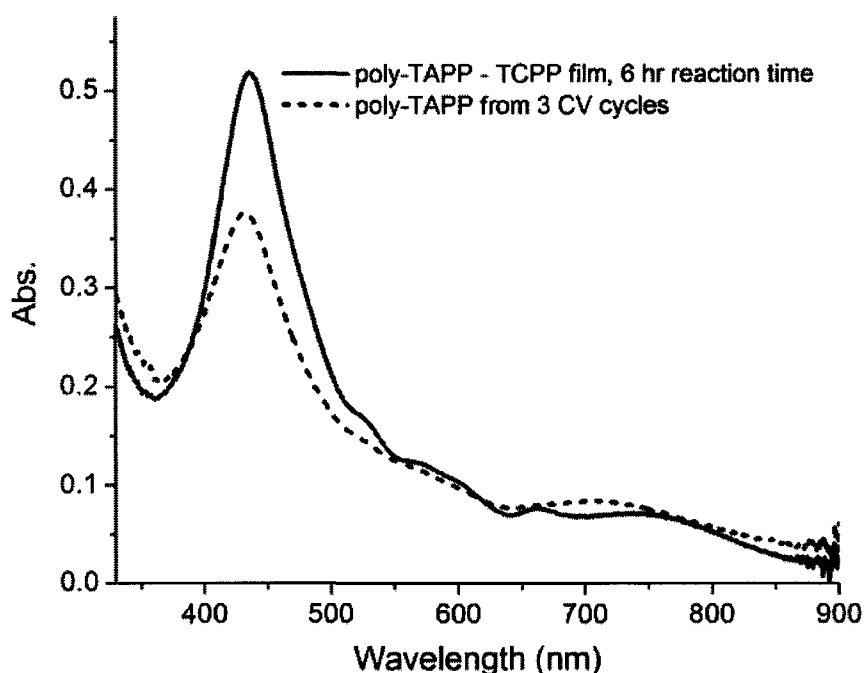


Figure 47. Poly-TAPP film absorbance spectra for the surface derivatization of poly-TAPP (synthesized from three electrochemical cycles) with TCCPP after 6 hr reaction

modeled after the methods reported and used by many DSSC researchers of applying a TiO_2 undercoat on top of the FTO before laying down the 10-15 μm thick TiO_2 nanoparticulate film [164]. Undercoats are usually applied by spin coating, or by pipetting a dilute solution of $\text{Ti}(\text{O}-i\text{Pr})_4$ in 2-propanol, which quickly hydrolyzes to an amorphous TiO_2 thin film. This undercoat can act as both a blocking layer to the redox couple interacting with the underlying FTO layer and an electrical connection between TiO_2 nanoparticulate films and the FTO conductive surface. Figure 48 shows SEM images of TiO_2 | poly-TAPP | TCCP film coated using dilute $\text{Ti}(\text{O}-\text{Pr})_4$ to spin

coat and hydrolyze the isopropoxide onto the surface of the nanofibers using 2 and 10 TiO_2 precursor coatings. Sequential layering of the precursor can be carried out because the deposited/hydrolyzed TiO_2 layer is no longer soluble in the precursor 2-

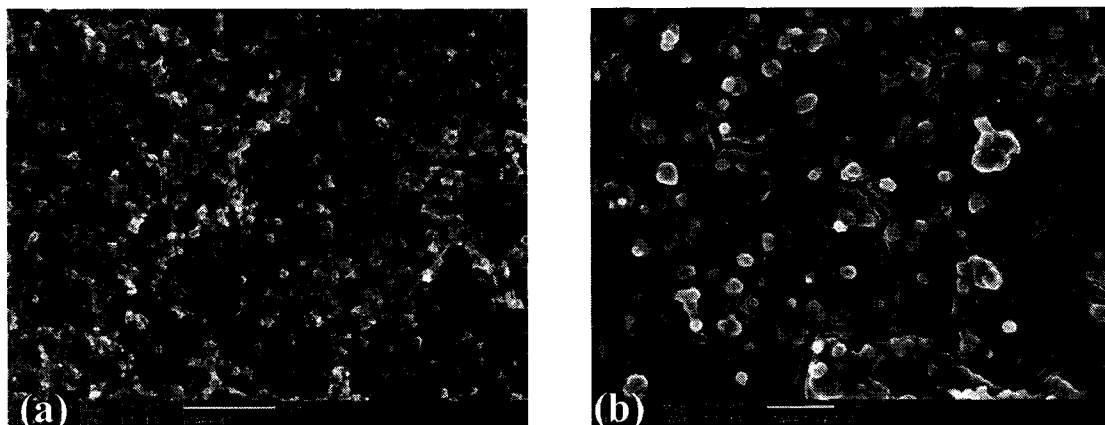


Figure 48. (a) Hydrolyzed TiO_2 coating from two $\text{Ti}(\text{O-Pr})_4$ precursor solution coatings, (b) ten precursor solution coatings

propanol solution. The SEM images reveal that the hydrolysis using 10 coatings exerted enough force on the poly-TAPP films to tear the film down to the FTO surface. The recognizable FTO crystallite layer is visible within the cracks caused by the hydrolysis. This is unfortunate, and would likely result in a short circuit after Al electrode evaporation. Therefore other strategies of conformally growing TiO_2 onto the poly-TAPP nanofibers were pursued.

The above technique represents one of the two basic approaches to incorporating TiO_2 materials into nanoporous materials. The first encompasses techniques developed to conformally grow TiO_2 onto the nanofibrous surface by

carefully infiltrating a TiO₂ precursor onto the surface, followed by hydrolysis and deposition. A second approach introduces already formed TiO₂ nanoparticles and coats the surface with the particles. The limitation of the first approach is that the deposited TiO₂ in many instances will be deposited in a non-crystalline or amorphous form which has lowered electron mobility. Crystalline nanoparticles have higher electron mobility than amorphous TiO₂; however, recent studies have suggested that a very thin amorphous TiO₂ layer (30 nm) deposited using sol-gel techniques can still provide electron mobilities high enough ($\mu_e = 1.7 \times 10^{-4} \text{ cm}^2\text{V}^{-1}\text{s}^{-1}$) to facilitate efficient electron injection from a bulk heterojunction photoactive layer [42,43]. A limitation of using already formed crystalline TiO₂ nanoparticles is the ability for the particles to penetrate and reach all surfaces within the nanoporous structure. It was determined that by using both methods sequentially, good incorporation of TiO₂ into the nanoporous poly-TAPP electrode can be achieved while retaining good connectivity and charge mobility within the crystalline TiO₂ particle layer. Firstly, new techniques to conformally grow a thin amorphous TiO₂ layer on the poly-TAPP nanofibers were studied, to be followed by TiO₂ nanoparticle infiltration using a paste of 10 nm particles to fill the remaining open pores within the film.

The method chosen for conformally growing the TiO₂ onto the porous poly-TAPP layer was one developed by several collaborators at Pacific Northwest National Laboratory and involved an aqueous sol-gel incorporation method [115,116]. The poly-TAPP was immersed in a solution of the commercial titanium lactate precursor “Tyzor LA” which hydrolyzes slowly at low pH ~ 2.1 at 70 °C. The films were taken

out immediately after the solution turned cloudy indicating the deposition process had increased dramatically (typically after 5 – 10 min. of reaction time). If slides were left in too long, the entire poly-TAPP film turned into a thick (500 nm) TiO_2 deposited

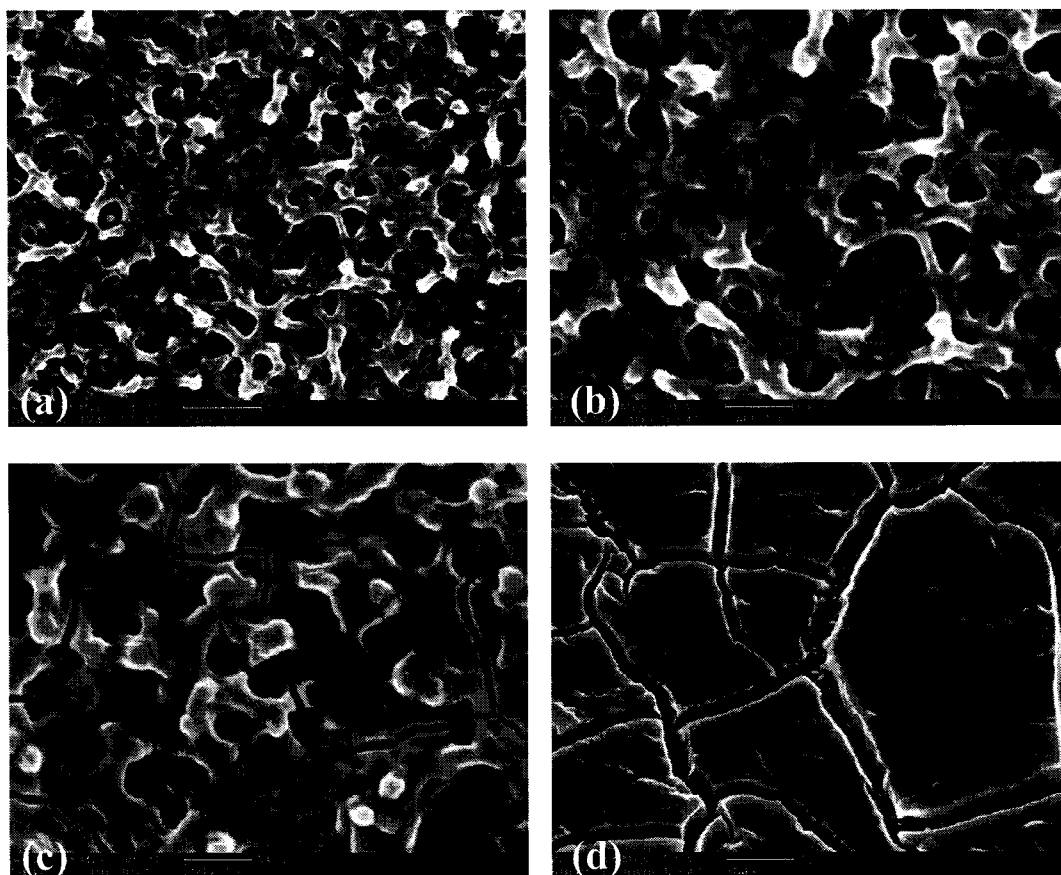


Figure 49. (a) Hydrolysis of Tyzor LA on a poly-TAPP electrode using a 0.05 M Tyzor LA solution at pH 2.1 after five minutes (onset of solution turning cloudy) (b) same conditions, higher magnification, (c) poly-TAPP electrode soaked for 15 minutes, (d) 30 minutes (~500 nm thick film – cracks reveal FTO confirmed by EDX)

layer (Figure 49 d), severely degrading the poly-TAPP layer and creating large cracks down to the FTO surface in the film. Figure 49 shows the structural results of the various conditions to conformally grow TiO_2 films.

Methods to incorporate the TiO_2 nanocrystalline particles were developed by simply using a commercial (Solaronix) 10 nm particle TiO_2 paste which was applied directly on top of the surface of the poly-TAPP film. The purpose of the extra TiO_2 particle layer is to smooth the top electrode surface where the top electrode contact would be evaporated. After the paste dried, the films were rinsed with water to remove excess particles from the surface. The SEM images in Figure 50 show the incorporation of TiO_2 particles onto a TiO_2 coated poly-TAPP | TCPP electrode. Figure 50 c shows XRD analysis of the deposited films indicating no evidence of crystalline anatase TiO_2 after the coating with the Tyzor LA solution (the primary peaks observed are all due to diffraction obtained from the underlying crystalline FTO electrode). The anatase form of TiO_2 after deposition with the nanoparticulate Solaronix paste (2θ at 25° , 37° , 65° - signature anatase peaks).

After completion of the cells by the evaporation of a top Al electrode, the devices were tested under AM 1.5 irradiation conditions. Figure 51 shows the performance of the inverse DSSC, including a current-voltage curve (a), current v. time (b), and the effects of light intensity on the device (c). The devices exhibited limited photovoltaic properties with photocurrents reaching as high as 0.05 mA/cm^2 . Unfortunately, the generated photocurrent began to degrade immediately after initial illumination. (Figure 51 b) After several minutes of testing under 100 mW/cm^2 ,

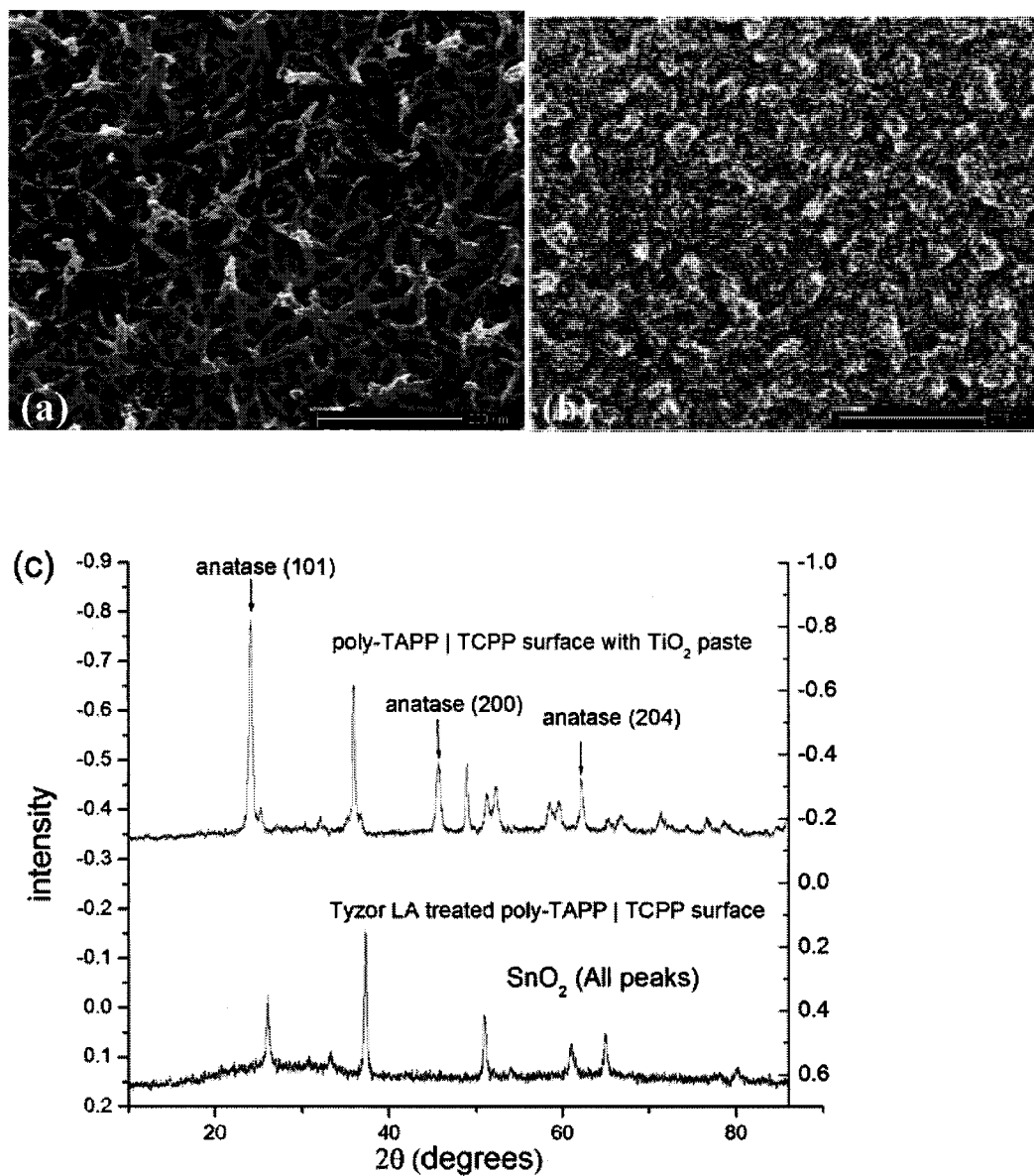


Figure 50. (a) Thin TiO₂ coated poly-TAPP from Tyzor LA solution, (b) after coating with Solaronix paste, drying, and rinsing with water to remove excess TiO₂ particles, (c) XRD showing the films after Tyzor LA treatment and after TiO₂ nanoparticulate paste incorporation

the devices were also tested at various light intensities (Figure 51 c) and exhibited near linear light intensity response up to 80 mW/cm^2 . Variations in the numbers of poly-TAPP CV cycles (1 or 3 CV) and the poly-TAPP synthesis conditions were tested in an inverse DSSC architecture (Table IV). The low fill factor observed for most of these devices are presumed to be a result of parallel and series resistances

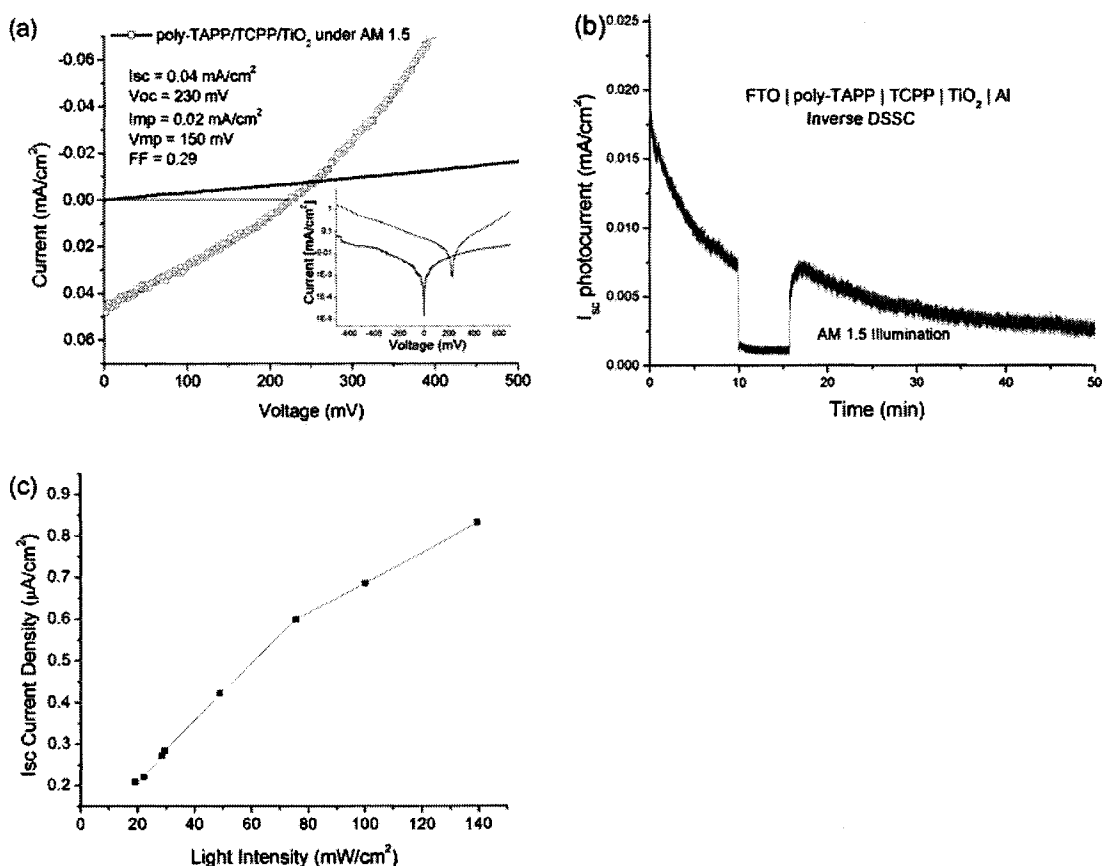


Figure 51. (a) Current-voltage curve of inverse DSSC under illumination 100 mW/cm^2 , (b) photocurrent vs. time, (c) photocurrent vs. light intensity – measurements taken after 30 min of irradiation

within the device. A common way to increase the fill factor in organic solar cells is to increase free charge carrier mobility within the hole conducting medium, usually accomplished by increasing the crystallinity of the polymer through a heat treatment step [165].

The low device performance and efficiencies may largely be due to the complications of the back Al electrode contact. In general, the evaporation of the back

Poly-TAPP Film (Synthesis Cond.)	I_{sc} (mA/cm⁻²)	V_{oc} (V)	FF	η_{eff} (%)
Poly-TAPP – 3 CV scans, 5% pyr	0.04	0.23	0.3	0.006
Poly-TAPP – 3 CV scans, 0% pyr	0.01	0.1	0.26	0.001
Poly-TAPP – 1 CV scans, 5% pyr	0.002	0.31	0.25	
Poly-TAPP – 1 CV scans, 0% pyr	0.0001	0.31	0.25	

Table IV. Summary of inverse DSSC cells tested under AM 1.5 conditions

(FTO | poly-TAPP | TCPP | TiO₂ from Tyzor LA | TiO₂ nanoparticles | Al)

contact is frequently a problematic component of the device construction. Even after the additional incorporation of TiO₂ nanoparticles to fill in the remaining pores, the top surface of the device is still quite rough due to the underlying poly-TAPP nanofibrous surface. (Figure 50 b) Frequently, inverse DSSCs constructed were

shorted due to Al metal contacting the FTO electrode through pinholes generated during the hydrolysis of the TiO_2 precursor. Therefore, making good contact to the top TiO_2 film and avoiding shorts is critical to optimizing the solar cell performance. In addition, the sensitivity of the evaporated aluminum electrode to oxygen could also cause resistive losses if oxidized aluminum is present.

Other issues of this type of nano-engineered device include the efficiency of TiO_2 coverage of the poly-TAPP film using the method developed for this device and the electron mobility through a combination of amorphous TiO_2 and the additional incorporated TiO_2 nanoparticles. The loss of photocurrent after illumination may also be due to the oxidative sensitivity of the porphyrin film under illumination. The stability of the conjugated hole conductor system is a common issue faced in the design and construction of bulk heterojunction solar cells [166]. Testing the devices under inert conditions or sealing the device to avoid the diffusion of oxygen into the photoactive layer is often crucial for sustaining generated photocurrents. However, overall, the photovoltaic response of these devices is improved over the liquid devices using poly-TAPP and I^-/I_3^- redox shuttle. The improvement is gained with increased light absorbance from the additional TCPP layer, and the improved photoinduced charge mechanisms present between the high surface area interfacial contact regions between the dye layer and the TiO_2 .

Chapter 4. CONCLUSIONS

Meso-substituted tetraphenylporphyrins with aminophenyl groups undergo oxidative electropolymerization depositing conductive nanostructured films when polymerized by cyclic voltammetry in dichloromethane. A wide variety of surface morphologies of electrochemically grown thin films have been observed depending on electrochemical solvent, potentiometric method, and the aminophenyl porphyrin monomer utilized. Porphyrins that successfully generated polymer films on the electrode include those tetrasubstituted with four para-aminophenyl groups, trisubstituted, or trans-disubstituted, however only the tetrasubstituted para-aminophenyl porphyrin tetrakis-5,10,15,20-(4-aminophenyl)porphyrin (TAPP) led to a nanofibrous film morphology. The morphology of poly-TAPP is a highly interconnected nanofibrous network, with fiber diameters in the range of 40-100 nm. It was initially discovered that by altering the poly-TAPP synthesis conditions with the addition of excess pyridine to the dichloromethane electrochemical solvent ($\geq 5\%$ vol), a highly interconnected nanofibrous polymer film surface could be engineered. Unfortunately, the poly-TAPP film growth slowed after a limited number of electrochemical growth cycles indicating passivation of the nanofibrous porphyrin polymer film surface. Films grown without using pyridine in the electrochemical solvent remained conductive throughout 30 electrochemical cycles. Nanostructured poly-TAPP features were also observed for free-floating films of poly-TAPP formed at an aqueous/DCM interface using an aqueous oxidant (ammonium persulfate) and

monomer TAPP in DCM. Interfacially polymerized poly-TAPP represents a new porphyrin polymer pathway to nanostructured porphyrin materials with improved film harvesting capabilities.

Reflectance FT-IR detected the presence of dihydrophenazine and phenazine linkage moieties within both types of deposited porphyrin films. Dihydrophenazine linkages were found in films whose electroactivity remained constant throughout the film growth process while phenazine linkages were prevalent in films where passivation and loss of electrochemical activity had occurred. In a process analogous to the formation of polyaniline, a mechanism for the growth characteristics and electrical conduction properties has been developed correlating poly-TAPP structure and film growth processes monitored using electrochemical quartz crystal microbalance measurements, UV-vis absorption characteristics, and FT-IR spectra. It is proposed that the loss of electrical activity is a result of the over oxidation of the film catalyzed by the addition of proton accepting agents such as pyridine which leads to a higher concentration of phenazine linkages within the film. To overcome these limitations, it was discovered that by adding minor amounts of water (instead of pyridine) to the electrochemical solvent to buffer the poly-TAPP polymerization process, the films remained conductive and produced nanofibrous features similar to those observed when using pyridine in the electrochemical solvent.

The poly-TAPP nanofibrous films were evaluated as a nanoporous scaffold for the construction of bulk heterojunction solar cells where the interfacial contact region is controlled by the poly-TAPP film structure. Appropriate electron acceptor materials

used include the fullerene derivative PCBM which can be incorporated into the films using drop cast film methods or TiO_2 which can be introduced using conformal growth methods to coat the poly-TAPP nanofibers. The introduction of TiO_2 layer in this manner forms the basis for the design of an “inverse” dye-sensitized solar cell where the TiO_2 electron accepting layer is deposited after the nanostructured poly-TAPP hole conducting layer. The interfacial geometry is therefore controlled by an optimized organic hole-conducting layer and in effect, the device is built inversely to the typical dye-sensitized TiO_2 nanoparticulate solar cell.

Poly-TAPP electrodes incorporated with PCBM into the nanoporous poly-TAPP film exhibited short-circuit current densities of $140 \mu\text{A}/\text{cm}^2$ and open-circuit potential values up to 500 mV. Increasing the film thickness led to an increase in the observed photocurrent with a corresponding drop in voltage. Incident photon to current efficiencies spectra indicate that the poly-TAPP is contributing to the photocurrent along with the PCBM layer. This suggests excitons are generated in both layers followed by dissociation at the interface with holes migrating through the poly-TAPP layer and electrons through the PCBM layer. Studies using only PCBM reveal that poly-TAPP is a crucial component for making increased interfacial contact and allowing for significantly increased solar energy conversion. An inverse dye-sensitized solar cell was developed by incorporating TiO_2 into a dye-coated nanoporous poly-TAPP electrode using an aqueous sol-gel technique. These cells demonstrated short-circuit current densities of $46 \mu\text{A}/\text{cm}^2$ and open-circuit potential values of 232 mV under AM 1.5 solar illumination. The lower performance of the

inverse DSSC has been attributed to poor contact with the overlying particulate TiO_2 layer and noncrystallinity in the thin amorphous TiO_2 layer coating the nanofibers.

While the application of these highly nanostructured poly-TAPP films for solar cells is intriguing, these electrochemically deposited films may also be useful in many other areas including optoelectronics, sensors, or biomaterials. In addition, very few electrochemically deposited conductive polymer films reported devote time to characterizing the morphology of the deposited films. The techniques used here to speed up the deposition process or alter the mechanism may be useful for other conductive polymer systems possibly resulting in more nanostructured polymer discoveries. Finally, the concept of an inverse dye-sensitized solar cell is novel, and may represent an important conceptual contribution to designing efficient dye-sensitized solar cells.

References

1. Annual Energy Outlook, E.; October 2007 ed.; Government, U. S., Ed.; Energy Information Administration, 2008.
2. Enting, I. G., Wigley, T. M. L. and Heimann, M.; Future emissions and concentrations of carbon dioxide: Key ocean/atmosphere/land analyses,. *CSIRO Division of Atmospheric Research* 1994.
3. Lewis, N. S. and Crabtree, G., Eds. *Basic Research Needs for Solar Energy Utilization*; Office of Science, U. S. Department of Energy, 2005.
4. Nocera, D. G.; On the future of global energy. *Daedalus* 2006; **135**: 112.
5. D'Souza, F., Smith, P. M., Zandler, M. E., McCarty, A. L., Itou, M., Araki, Y. and Ito, O.; Energy Transfer Followed by Electron Transfer in a Supramolecular Triad Composed of Boron Dipyrin, Zinc Porphyrin, and Fullerene: A Model for the Photosynthetic Antenna-Reaction Center Complex. *J. Am. Chem. Soc.* 2004; **126**: 7898-7907.
6. SPV 2006 Solar Photovoltaic Report. *Solar Photovoltaics Report* 2006: 1-128.
7. Shaheen, S. E., Ginley, D. S. and Jabbour, G. E.; Organic-based photovoltaics: toward low-cost power generation. *MRS Bulletin* 2005; **30**: 10-19.
8. U.S. Photovoltaic Industry Roadmap. *U.S. Dept. of Energy* 2001.
9. Nanosolar; High-Performance Thin-Film Photovoltaics Using Low-Cost Process Technology. *PVSEC* 2008.
10. O'Regan, B. and Grätzel, M.; A low-cost, high-efficiency solar cell based on dye-sensitized colloidal titanium dioxide films. *Nature* 1991; **353**: 737-740.
11. Yu, G., Gao, J., Hummelen, J. C., Wudl, F. and Heeger, A. J.; Polymer Photovoltaic Cells: Enhanced Efficiencies via a Network of Internal Donor-Acceptor Heterojunctions. *Science* 1995; **270**: 1789-1791.
12. Brabec, C. J., Sariciftci, N. S. and Hummelen, J. C.; Plastic solar cells. *Adv. Funct. Mater.* 2001; **11**: 15-26.
13. Gledhill, S. E., Scott, B. and Gregg, B. A.; Organic and nano-structured composite photovoltaics: An overview. *J. Mater. Res.* 2005; **20**: 3167-3179.

14. Winder, C., Matt, G., Hummelen, J. C., Janssen, R. A. J., Sariciftci, N. S. and Brabec, C. J.; Sensitization of low bandgap polymer bulk heterojunction solar cells. *Thin Solid Films* 2002; **403-404**: 373-379.
15. Gregg, B. A.; Excitonic Solar Cells. *J. Phys. Chem. B* 2003; **107**: 4688-4698.
16. Kietzke, T.; Recent Advances in Organic Solar Cells. *Adv. Opto. Elect.* 2007: 40285.
17. Mor, G. K., Shankar, K., Paulose, M., Varghese, O. K. and Grimes, C. A.; Use of Highly-Ordered TiO₂ Nanotube Arrays in Dye-Sensitized Solar Cells. *Nano Lett.* 2006; **6**: 215-218.
18. Xin, H., Kim, F. S. and Jenekhe, S. A.; Highly Efficient Solar Cells Based on Poly(3-butylthiophene) Nanowires. *J. Am. Chem. Soc.* 2008; **130**: 5424-5425.
19. Gregg, B. A. In *Organic Photovoltaics*, Sariciftci, N. S. (Ed.), 2004; pp 139 - 159.
20. Nelson, J. In *The Physics of Solar Cells*, 2002; pp 17-39.
21. Nazeeruddin, M. K. P., P.; Renouard, T.; Zakeeruddin, S. M.; Humphry-Baker, R.; Comte, P.; Liska, P.; Cevey, L.; Costa, E.; Shklover, V.; Spiccia, L.; Deacon, G. B.; Bignozzi, C. A.; Grätzel, M.; Engineering of Efficient Panchromatic Sensitizers for Nanocrystalline TiO₂-Based Solar Cells. *J. Am. Chem. Soc.* 2001; **123**: 1613-1624.
22. Grätzel, M.; Solar Energy Conversion by Dye-Sensitized Photovoltaic Cells. *Inorg. Chem.* 2005; **44**: 6841-6851.
23. Hamann, T. W., Jensen, R. A., Martinson, A. B. F., Ryswyk, H. V. and Hupp, J. T.; Advancing beyond current generation dye-sensitized solar cells. *Energy & Environ. Sci.* 2006; **1**: 66-78.
24. Kim, H.-S. and Wamser, C. C.; Photoelectropolymerization of aniline in a dye-sensitized solar cell. *Photochem. Photobiol. Sci.* 2006; **5**: 955-960.
25. Nogueira, A. F., Longo, C. and De Paoli, M. A.; Polymers in dye sensitized solar cells: overview and perspectives. *Coord. Chem. Rev.* 2004; **248**: 1455-1468.
26. Saito, Y., Azechi, T., Kitamura, T., Hasegawa, Y., Wada, Y. and Yanagida, S.; Photo-sensitizing ruthenium complexes for solid state dye solar cells in combination with conducting polymers as hole conductors. *Coord. Chem. Rev.* 2004; **248**: 1469-1478.

27. Bisquert, J., Cahen, D., Hodes, G., Ruehle, S. and Zaban, A.; Physical Chemical Principles of Photovoltaic Conversion with Nanoparticulate, Mesoporous Dye-Sensitized Solar Cells. *J. Phys. Chem. B* 2004; **108**: 8106-8118.
28. Wang, P., Wenger, B., Humphry-Baker, R., Moser, J.-E., Teuscher, J., Kantlehner, W., Mezger, J., Stoyanov, E. V., Zakeeruddin, S. M. and Grätzel, M.; Charge Separation and Efficient Light Energy Conversion in Sensitized Mesoscopic Solar Cells Based on Binary Ionic Liquids. *J. Am. Chem. Soc.* 2005; **127**: 6850-6856.
29. Kubo, W., Murakoshi, K., Kitamura, T., Yoshida, S., Haruki, M., Hanabusa, K., Shirai, H., Wada, Y. and Yanagida, S.; Quasi-Solid-State Dye-Sensitized TiO₂ Solar Cells: Effective Charge Transport in Mesoporous Space Filled with Gel Electrolytes Containing Iodide and Iodine. *J. Phys. Chem. B* 2001; **105**: 12809-12815.
30. Bai, Y., Cao, Y., Zhang, J., Wang, M., Li, R., Wang, P., Zakeeruddin, S. M. and Grätzel, M.; High-performance dye-sensitized solar cells based on solvent-free electrolytes produced from eutectic melts. *Nat. Mater.* 2008; **7**: 626-630.
31. Grätzel, M.; Dye-sensitized solid-state heterojunction solar cells. *MRS Bulletin* 2005; **30**: 23-27.
32. Zukalova, M., Zukal, A., Kavan, L., Nazeeruddin, M. K., Liska, P. and Grätzel, M.; Organized Mesoporous TiO₂ Films Exhibiting Greatly Enhanced Performance in Dye-Sensitized Solar Cells. *Nano Letters* 2005; **5**: 1789-1792.
33. Oekermann, T., Zhang, D., Yoshida, T. and Minoura, H.; Electron Transport and Back Reaction in Nanocrystalline TiO₂ Films Prepared by Hydrothermal Crystallization. *Journal of Physical Chemistry B* 2004; **108**: 2227-2235.
34. Hurum, D. C., Gray, K. A., Rajh, T. and Thurnauer, M. C.; Recombination Pathways in the Degussa P25 Formulation of TiO₂: Surface versus Lattice Mechanisms. *J. Phys. Chem. B* 2005; **109**: 977-980.
35. Holmes-Smith, A. S., Hamill, A., Campbell, M. and Uttamlal, M.; Electropolymerized platinum porphyrin polymers for dissolved oxygen sensing. *Analyst (Cambridge, United Kingdom)* 1999; **124**: 1463-1466.
36. Sariciftci, N. S., Smilowitz, L., Heeger, A. J. and Wudl, F.; Photoinduced Electron Transfer from a Conducting Polymer to Buckminsterfullerene. *Science* 1992; **258**: 1474-1476.

37. Hoppe, H., Egbe, D. A. M., Muehlbacher, D. and Sariciftci, N. S.; Photovoltaic action of conjugated polymer/fullerene bulk heterojunction solar cells using novel PPE-PPV copolymers. *J. Mater. Chem.* 2004; **14**: 3462-3467.
38. Ma, W., Yang, C., Gong, X., Lee, K. and Heeger, A. J.; Thermally stable efficient polymer solar cells with nanoscale control of the interpenetrating network morphology. *Advanced Functional Materials* 2005; **15**: 1617-1622.
39. Sariciftci, N. S. and Winder, C.; Low bandgap polymers for photon harvesting in bulk heterojunction solar cells. *J. Mater. Chem.* 2004; **14**: 1077 - 1086.
40. Bundgaard, E. and Krebs, F. C.; Low band gap polymers for organic photovoltaics. *Solar Energy Materials & Solar Cells* 2007; **91**: 954-985.
41. Scharber, M. C., Muehlbacher, D., Koppe, M., Denk, P., Waldauf, C., Heeger, A. J. and Brabec, C. J.; Design rules for donors in bulk-heterojunction solar cells-towards 10 % energy-conversion efficiency. *Advanced Materials (Weinheim, Germany)* 2006; **18**: 789-794.
42. Kim, J. Y., Kim, S. H., Lee, H.-H., Lee, K., Ma, W., Gong, X. and Heeger, A. J.; New architecture for high-efficiency polymer photovoltaic cells using solution-based titanium oxide as an optical spacer. *Adv. Mater.* 2006; **18**: 572-576.
43. Waldauf, C., Morana, M., Denk, P., Schilinsky, P., Coakley, K., Choulis, S. A. and Brabec, C. J.; Highly efficient inverted organic photovoltaics using solution based titanium oxide as electron selective contact. *Appl. Phys. Lett.* 2006; **89**: 233517/233511-233517/233513.
44. Yang, X., Loos, J., Veenstra, S. C., Verhees, W. J. H., Wienk, M. M., Kroon, J. M., Michels, M. A. J. and Janssen, R. A. J.; Nanoscale Morphology of High-Performance Polymer Solar Cells. *Nano Letters* 2005; **5**: 579-583.
45. Kim, H., So, W.-W. and Moon, S.-J.; The importance of post-annealing process in the device performance of poly(3-hexylthiophene): Methanofullerene polymer solar cell. *Solar Energy Materials & Solar Cells* 2007; **91**: 581-587.
46. Martens, T., Munters, T., Goris, L., D'Haen, J., Schouteden, K., D'Olieslaeger, M., Lutsen, L., Vanderzande, D., Geens, W., Poortmans, J., De Schepper, L. and Manca, J. V.; Nanostructured organic pn junctions towards 3D photovoltaics. *Appl. Phys. A: Mater. Sci. & Proc.* 2004; **79**: 27-30.
47. Kadish, K. M., Smith, K. M. and Guillard, R., Eds. *The Porphyrin Handbook*; Academic Press: San Diego, 2000.

48. Duncan, T. V., Rubtsov, I. V., Uyeda, H. T. and Therien, M. J.; Highly Conjugated (Polypyridyl)metal-(Porphinato)zinc(II) Compounds: Long-Lived, High Oscillator Strength, Excited-State Absorbers Having Exceptional Spectral Coverage of the Near-Infrared. *J. Am. Chem. Soc.* 2004; **126**: 9474-9475.
49. Hasobe, T., Imahori, H., Yamada, H., Sato, T., Ohkubo, K. and Fukuzumi, S.; Enhancement of light harvesting and photocurrent generation by ITO electrodes modified with meso,meso-linked porphyrin oligomers. *Nano Lett.* 2003; **3**: 409-412.
50. Cherian, S. and Wamser, C. C.; Adsorption and Photoactivity of Tetra(4-carboxyphenyl)porphyrin (TCPP) on Nanoparticulate TiO₂. *J. Phys. Chem. B.* 2000; **104**: 3624-3629.
51. Campbell, W. M., Burrell, A. K., Officer, D. L. and Jolley, K. W.; Porphyrins as light harvesters in the dye-sensitized TiO₂ solar cell. *Coord. Chem. Rev.* 2004; **248**: 1363-1379.
52. Gust, D., Moore, T. A. and Moore, A. L.; Mimicking Photosynthetic Solar Energy Transduction. *Acc. Chem. Res.* 2000; **34**: 40-48.
53. Alstrum-Acevedo, J. H., Brennaman, M. K. and Meyer, T. J.; Chemical Approaches to Artificial Photosynthesis. 2. *Inorg. Chem.* 2005; **44**: 6802-6827.
54. Udaltsov, A. V. and Kovalev, Y. V.; Photoinduced self-organization of donor-acceptor complex intended for oxidative splitting of water. *J. Photochem. Photobiol., A* 2000; **135**: 193-202.
55. Vail, S. A., Schuster, D. I., Guldi, D. M., Isosomppi, M., Tkachenko, N., Lemmetyinen, H., Palkar, A., Echegoyen, L., Chen, X. and Zhang, J. Z. H.; Energy and Electron Transfer in b-Alkynyl-Linked Porphyrin-[60]Fullerene Dyads. *J. Phys. Chem. B* 2006; **110**: 14155-14166.
56. Durantini, E. N.; Synthesis and Spectroscopic Properties of a Covalently Linked Porphyrin-Fullerene C₆₀ Dyad. *Synth. Commun.* 2006; **36**: 2135-2144.
57. Isosomppi, M., Tkachenko, N. V., Efimov, A., Kaunisto, K., Hosomizu, K., Imahori, H. and Lemmetyinen, H.; Photoinduced electron transfer in multilayer self-assembled structures of porphyrins and porphyrin-fullerene dyads on ITO. *J. Mater. Chem.* 2005; **15**: 4546-4554.
58. Spanggaard, H. and Krebs, F. C.; A brief history of the development of organic and polymeric photovoltaics. *Sol. Energy Mater. Sol. Cells* 2004; **83**: 125-146.

59. Wang, Z., Medforth, C. J. and Shelnutt, J. A.; Porphyrin Nanotubes by Ionic Self-Assembly. *J. Am. Chem. Soc.* 2004; **126**: 15954-15955.
60. Li, W. and Wamser, C. C.; Synthesis and Characterization of Interfacially Polymerized Films of Tetraphenylporphyrin Derivatives. *Langmuir* 1995; **11**: 4061-4071.
61. Holten, D., Bocian, D. F. and Lindsey, J. S.; Probing Electronic Communication in Covalently Linked Multiporphyrin Arrays. A Guide to the Rational Design of Molecular Photonic Devices. *Acc. Chem. Res.* 2002; **35**: 57-69.
62. Kay, A. and Grätzel, M.; Artificial Photosynthesis. 1. Photosensitization of Titanium Dioxide Solar Cells with Chlorophyll Derivatives and Related Natural Porphyrins. *J. Phys. Chem.* 1993; **97**: 6272-6277.
63. Kalyanasundaram, K., Vlachopoulos, N., Krishnan, V., Monnier, A. and Gratzel, M.; Sensitization of titanium dioxide in the visible light region using zinc porphyrins. *J. Phys. Chem.* 1987; **91**: 2342-2347.
64. Odobel, F., Blart, E., Lagree, M., Villieras, M., Boujtita, H., El Murr, N., Caramori, S. and Alberto Bignozzi, C.; Porphyrin dyes for TiO₂ sensitization. *Journal of Materials Chemistry* 2003; **13**: 502-510.
65. Jasieniak, J., Johnston, M. and Wacławik, E. R.; Characterization of a Porphyrin-Containing Dye-Sensitized Solar Cell. *J. Phys. Chem. B* 2004; **108**: 12962-12971.
66. Campbell, W. M., Jolley, K. W., Wagner, P., Wagner, K., Walsh, P. J., Gordon, K. C., Schmidt-Mende, L., Nazeeruddin, M. K., Wang, Q., Grätzel, M. and Officer, D. L.; Highly Efficient Porphyrin Sensitizers for Dye-Sensitized Solar Cells. *J. Phys. Chem. C* 2007; **111**: 11760-11762.
67. Wang, Q., Campbell, W. M., Bonfantani, E. E., Jolley, K. W., Officer, D. L., Walsh, P. J., Gordon, K., Humphrey-Baker, R., Nazeeruddin, M. K. and Grätzel, M.; Efficient Light Harvesting by Using Green Zn-Porphyrin-Sensitized Nanocrystalline TiO₂ Films. *J. Phys. Chem. B* 2005; **109**: 15397-15409.
68. Hasobe, T., Saito, K., Kamat, P. V., Troiani, V., Qiu, H., Solladie, N., Kim, K. S., Park, J. K., Kim, D., D'Souza, F. and Fukuzumi, S.; Organic solar cells. Supramolecular composites of porphyrins and fullerenes organized by polypeptide structures as light harvesters. *J. Mater. Chem.* 2007; **17**: 4160-4170.
69. Dastoor, P. C., McNeill, C. R., Frohne, H., Foster, C. J., Dean, B., Fell, C. J., Belcher, W. J., Campbell, W. M., Officer, D. L., Blake, I. M., Thordarson, P.,

- Crossley, M. J., Hush, N. S. and Reimers, J. R.; Understanding and Improving Solid-State Polymer/C₆₀-Fullerene Bulk-Heterojunction Solar Cells Using Ternary Porphyrin Blends. *J. Phys. Chem. C* 2007; **111**: 15415-15426.
70. Sun, Q., Dai, L., Zhou, X., Li, L. and Li, Q.; Bilayer- and bulk-heterojunction solar cells using liquid crystalline porphyrins as donors by solution processing. *Appl. Phys. Lett.* 2007; **91**: 253505-253503.
71. Yun, J.-J., Jung, H.-S., Kim, S.-H., Han, E.-M., Vaithianathan, V. and Jenekhe, S. A.; Chlorophyll-layer-inserted poly(3-hexyl-thiophene) solar cell having a high light-to-current conversion efficiency up to 1.48%. *Appl. Phys. Lett.* 2005; **87**: 123102-123103.
72. El-Khouly, M. E., Araki, Y., Ito, O., Gadde, S., McCarty, A. L., Karr, P. A., Zandler, M. E. and D'Souza, F.; Spectral, electrochemical, and photophysical studies of a magnesium porphyrin-fullerene dyad. *Phys. Chem. Chem. Phys.* 2005; **7**: 3163-3171.
73. Bhattacharya, S., Ujihashi, N., Aonuma, S., Kimura, T. and Komatsu, N.; Spectral and theoretical studies on effective and selective non-covalent interaction between tetrahexylporphyrins and fullerenes. *Spectrochim. Acta, Part A* 2007; **68**: 495-503.
74. Guldi, D. M., Nuber, B., Bracher, P. J., Alabi, C. A., MacMahon, S., Kukol, J. W., Wilson, S. R. and Schuster, D. I.; Synthesis and Photophysics of a Copper-Porphyrin-Styrene-C₆₀ Hybrid. *J. Phys. Chem. A* 2003; **107**: 3215-3221.
75. Hasobe, T., Imahori, H., Fukuzumi, S. and Kamat, P. V.; Light Energy Conversion Using Mixed Molecular Nanoclusters. Porphyrin and C₆₀ Cluster Films for Efficient Photocurrent Generation. *J. Phys. Chem. B* 2003; **107**: 12105-12112.
76. White, B. A. and Murray, R. W.; Electroactive Porphyrin Films from Electropolymerized Metallotetra(o-aminophenyl)porphyrins. *J. Electroanal. Chem.* 1985; **189**: 345-352.
77. Trevin, S., Bedioui, F., Villegas, M. G. G. and Bied-Charreton, C.; Electropolymerized nickel macrocyclic complex-based films: design and electrocatalytic application. *J. Mater. Chem.* 1997; **7**: 923-928.
78. Pressprich, K. A., Maybury, S. G., Thomas, R. E., Linton, R. W., Irene, E. A. and Murray, R. W.; Molecular Sieving by Electropolymerized Porphyrin Films Only a Few Monolayers Thick. *J. Phys. Chem.* 1989; **93**: 5568-5574.

79. Bettelheim, A., Soifer, L. and Korin, E.; Electropolymerized porphyrin films as methanol barriers in direct methanol fuel cells. *J. Electroanal. Chem.* 2004; **571**: 265-272.
80. Maree, C. H. M., Roosendaal, S. J., Savenije, T. J., Schropp, R. E. I., Schaafsma, T. J. and Habraken, F. H. P. M.; Photovoltaic Effects in Porphyrin Polymer Films and Heterojunctions. *J. Appl. Phys.* 1996; **80**: 3381-3389.
81. Bedioui, F., Devynck, J. and Bied-Charreton, C.; Immobilization of Metalloporphyrins in Electropolymerized Films: Design and Applications. *Acc. Chem. Res.* 1995; **28**: 30-36.
82. Yuasa, M., Oyaizu, K., Yamaguchi, A., Ishikawa, M., Eguchi, K., Kobayashi, T., Toyoda, Y. and Tsutsui, S.; Structure and redox properties of electropolymerized film obtained from iron meso-tetrakis(3-thienyl)porphyrin. *Polym. Adv. Tech.* 2005; **16**: 616-621.
83. Macor, K. A. and Spiro, T. G.; Porphyrin Electrode Films Prepared by Electrooxidation of Metalloprotoporphyrins. *J. Am. Chem. Soc.* 1983; **105**: 5601-5607.
84. Armijo, F., Ferraudi, G., Isaacs, F., Aguirre, M. J. and Costamagna, J.; On the photo- and electro-induced polymerization of M(tetrakis(x-aminophenyl)porphyrin), where x = 2, 3 or 4 and M = Zn(II) or Ni(II). *Inorganica Chimica Acta* 2006; **359**: 2281-2284.
85. Ransdell, R. A. and Wamser, C. C.; Solvent and Substituent Effects on the Redox Properties of Free-Base Tetraphenylporphyrins in DMSO and Aqueous DMSO. *J. Phys. Chem.* 1992; **96**: 10572-10575.
86. Lin, C.-Y., Hung, Y.-C., Liu, C.-M., Lo, C.-F., Lin, Y.-C. and Lin, C.-L.; Synthesis, electrochemistry, absorption and electro-polymerization of aniline-ethynyl metalloporphyrins. *Dalton Trans.* 2005: 396-401.
87. Bruti, E. M., Giannetto, M., Mori, G. and Seeber, R.; Electropolymerization of Tetrakis(o-aminophenyl)porphyrin and Relevant Transition Metal Complexes from Aqueous Solution. The Resulting Modified Electrodes as Potentiometric Sensors. *Electroanal.* 1999; **11**: 565-572.
88. Cornejo, G., Ramirez, G., Villagran, M., Costamagna, J., Trollund, E. and Aguirre, M. J.; Electropolymerization and electrocatalytic behavior of electrodes modified with Fe and non-metalled tetraaminophenylporphyrins: Effect of the position of the amino group on the ligand. *Journal of the Chilean Chemical Society* 2003; **48**: 49-55.

89. Chen, S.-M., Chen, Y.-L. and Thangamuthu, R.; Electropolymerization of iron tetra(o-aminophenyl)porphyrin from aqueous solution and the electrocatalytic behavior of modified electrode. *J. Solid State Electrochem.* 2007; **11**: 1441-1448.
90. Huang, S. S., Tang, H. and Li, B. F.; Electrochemistry of electropolymerized tetra(p-aminophenyl)porphyrin nickel film electrode and catalytic oxidation of acetaminophen. *Mikrochim. Acta* 1998; **128**: 37-42.
91. Phillips, S. D., Yu, G., Cao, Y. and Heeger, A. J.; Spectroscopy and transient photoconductivity of partially crystalline polyaniline. *Physical Review B: Condensed Matter and Materials Physics* 1989; **39**: 10702-10707.
92. Luzny, W. and Banka, E.; Relations between the Structure and Electric Conductivity of Polyaniline Protonated with Camphorsulfonic Acid. *Macromolecules* 2000; **33**: 425-429.
93. Wei, X. L., Wang, Y. Z., Long, S. M., Bobeczko, C. and Epstein, A. J.; Synthesis and Physical Properties of Highly Sulfonated Polyaniline. *J. Am. Chem. Soc.* 1996; **118**: 2545-2555.
94. Trchova, M., Sedenkova, I., Konyushenko, E. N., Stejskal, J., Holler, P. and Ciric-Marjanovic, G.; Evolution of Polyaniline Nanotubes: The Oxidation of Aniline in Water. *J. Phys. Chem. B* 2006; **110**: 9461-9468.
95. Bettelheim, A., White, B. A., Raybuck, S. A. and Murray, R. W.; Electrochemical Polymerization of Amino-, Pyrrole-, and Hydroxy-substituted Tetraphenylporphyrins. *Inorg. Chem.* 1987; **26**: 1009-1017.
96. Weinkauff, J. R., Cooper, S. W., Schweiger, A. and Wamser, C. C.; Substituent and Solvent Effects on the Hyperporphyrin Spectra of Diprotonated Tetraphenylporphyrins. *J. Phys. Chem. A* 2003; **107**: 3486-3496.
97. Ojadi, E. C. A., Linschitz, H., Gouterman, M., Walter, R. I., Lindsey, J. S., Wagner, R. W., Droupadi, P. R. and Wang, W.; Sequential Protonation of meso-(p-(Dimethylamino)Phenyl) Porphyrins: Charge-Transfer Excited States Producing Hyperporphyrins. *J. Phys. Chem.* 1993; **97**: 13192 - 13197.
98. Walter, R. I., Ojadi, E. C. A. and Linschitz, H.; A Proton NMR Study of the Reactions with Acid of Meso-Tetraphenylporphyrins with Various Numbers of 4-Dimethylamino Groups. *J. Phys. Chem.* 1993; **97**: 13308 - 13312.
99. Okada, S. and Segawa, H.; Substituent-Control Exciton in J-Aggregates of Protonated Water-Insoluble Porphyrins. *J. Am. Chem. Soc.* 2003; **125**: 2792-2796.

100. Liddell, P. A., Gervaldo, M., Bridgewater, J. W., Keirstead, A. E., Lin, S., Moore, T. A., Moore, A. L. and Gust, D.; Porphyrin-Based Hole Conducting Electropolymer. *Chem. Mater.* 2008; **20**: 135-142.
101. Holmes-Smith, A. S., Zheng, X. and Uttamlal, M.; Characterization of an electropolymerized Pt(II) diamino phenyl porphyrin polymer suitable for oxygen sensing. *Meas. Sci. Technol.* 2006; **17**: 3328-3334.
102. Bennett, J. E. and Malinski, T.; Conductive Polymeric Porphyrin Films: Application in the Electrocatalytic Oxidation of Hydrazine. *Chem. Mater.* 1991; **3**: 490-495.
103. Armijo, F., Goya, M. C., Gimeno, Y., Arevalo, M. C., Aguirre, M. J. and Creus, A. H.; Study of the electropolymerization of tetrakis(3-aminophenyl)porphyrin Fe(III) chloride on Au electrodes by cyclic voltammetry and STM. *Electrochem. Commun.* 2006; **8**: 779-784.
104. Duong, B., Arechabaleta, R. and Tao, N. J.; In situ AFM/STM characterization of porphyrin electrode films for electrochemical detection of neurotransmitters. *J. Electroanal. Chem.* 1998; **447**: 63-69.
105. Doan Stephanie, C., Shanmugham, S., Aston, D. E. and McHale Jeanne, L.; Counterion dependent dye aggregates: nanorods and nanorings of tetra(p-carboxyphenyl)porphyrin. *J. Am. Chem. Soc.* 2005; **127**: 5885-5892.
106. Schwab, A. D., Smith, D. E., Bond-Watts, B., Johnston, D. E., Hone, J., Johnson, A. T., dePaula, J. C. and Smith, W. F.; Photoconductivity of Self-Assembled Porphyrin Nanorods. *Nano Lett.* 2004; **4**: 1261-1265.
107. Hu, J. S., Guo, Y. G., Liang, H. P., Wan, L. J. and Jiang, L.; Three-Dimensional Self-Organization of Supramolecular Self-Assembled Porphyrin Hollow Hexagonal Nanoprisms. *J. Am. Chem. Soc.* 2005; **127**: 17090-17095.
108. Huang, J. and Kaner, R. B.; A general chemical route to polyaniline nanofibers. *J. Am. Chem. Soc.* 2004; **126**: 851-855.
109. Gupta, V. and Miura, N.; Electrochemically deposited polyaniline nanowire's network, a high-performance electrode material for redox supercapacitor. *Electrochem. Solid-State Lett.* 2005; **8**: A630-A632.
110. Ding, H., Wan, M. and Wei, Y.; Controlling the diameter of polyaniline nanofibers by adjusting the oxidant redox potential. *Adv. Mater.* 2007; **19**: 465-469.

111. Walter, M. G., Wamser, C. C., Ruwitch, J., Zhao, Y., Braden, D., Stevens, M., Denman, A., Pi, R., Rudine, A. and Pessiki, P. J.; Syntheses and optoelectronic properties of amino/carboxyphenylporphyrins for potential use in dye-sensitized TiO₂ solar cells. *J. Porphyrins Phthalocyanines* 2007; **11**: 601-612.
112. Littler, B. J., Ciringh, Y. and Lindsey, J. S.; Investigation of Conditions Giving Minimal Scrambling in the Synthesis of trans-Porphyrins from Dipyrromethanes and Aldehydes. *Journal of Organic Chemistry* 1999; **64**: 2864-2872.
113. Littler, B. J., Miller, M. A., Hung, C., Wagner, R. W., O'Shea, D. F., Boyle, P. D. and Lindsey, J. S.; Refined Synthesis of 5-Substituted Dipyrromethanes. *J. Org. Chem.* 1999; **64**: 1391-1396.
114. Sobral, A. J. F. N., Rebanda, N. G. C. L., da Silva, M., Lampreia, S. H., Ramos Silva, M., Beja, A. M., Paixao, J. A. and Rocha Gonsalves, A. M. d. A.; One-step synthesis of dipyrromethanes in water. *Tetrahedron Letters* 2003; **44**: 3971-3973.
115. Li, X. S., Fryxell, G. E., Engelhard, M. H. and Wang, C.; The synthesis of cadmium doped mesoporous TiO₂. *Inorg. Chem.* 2007; **10**: 639-641.
116. Li, X. S., Fryxell, G. E., Birnbaum, J. C. and Wang, C.; Effects of Template and Precursor Chemistry on Structure and Properties of Mesoporous TiO₂ Thin Films. *Langmuir* 2004; **20**: 9095-9102.
117. Bettelheim, A., Ozer, D., Harth, R. and Murray, R. W.; Electrochemistry of various substituted aminophenyl iron porphyrins:
Part I. Redox properties of dissolved, adsorbed and electropolymerised species. *J. Electroanal. Chem.* 1989; **266**: 93-108.
118. Paolesse, R., Natale, C. D., Dall'Orto, V. C., Macagnano, A., Angelaccio, A., Motta, N., Sgarlata, A., Hurst, J., Rezzano, I., Mascini, M. and D'Amico, A.; Porphyrin thin films coated quartz crystal microbalances prepared by electropolymerization technique. *Thin Solid Films* 1999; **354**: 245-250.
119. Laviron, E.; General expression of the linear potential sweep voltammogram in the case of diffusionless electrochemical systems. *J. Electroanal. Chem.* 1979; **101**: 19-28.
120. Le Mest, Y., L'Her, M., Hendricks, N. H., Kim, K. and Collman, J. P.; Electrochemical and spectroscopic properties of dimeric cofacial porphyrins with nonelectroactive metal centers. Delocalization processes in the porphyrin .pi.-cation-radical systems. *Inorg. Chem.* 1992; **31**: 835-847.

121. Seshadri, V., Wu, L. and Sotzing, G. A.; Conjugated Polymers via Electrochemical Polymerization of Thieno[3,4-b]thiophene (T34bT) and 3,4-Ethylenedioxythiophene (EDOT). *Langmuir* 2003; **19**: 9479-9485.
122. Heinze, J., Rasche, A., Pagels, M. and Geschke, B.; On the Origin of the So-Called Nucleation Loop during Electropolymerization of Conducting Polymers. *J. Phys. Chem. B* 2007; **111**: 989-997.
123. Carrillo, I., Sanchez de la Blanca, E. and Gonzalez-Tejera, M. J.; Influence of the electropolymerization time on the nucleation mechanism, structure and morphology of polyfuran/perchlorate doped films. *Polymer* 2001; **42**: 9447-9453.
124. Baba, A., Tian, S., Stefani, F., Xia, C., Wang, Z., Advincula, R. C., Johannsmann, D. and Knoll, W.; Electropolymerization and doping/dedoping properties of polyaniline thin films as studied by electrochemical-surface plasmon spectroscopy and by the quartz crystal microbalance. *J. Electroanal. Chem.* 2004; **562**: 95-103.
125. Savenije, T. J., Koehorst, R. B. M. and Schaafsma, T. J.; Spectroelectrochemical Measurement of Charge Transport Properties of Electropolymerized Tetrakis(hydroxyphenyl)porphyrins. *J. Phys. Chem. B* 1997; **101**: 720-725.
126. Huang, J. and Kaner, R. B.; The Intrinsic nanofibrillar morphology of polyaniline. *Chem. Commun.* 2006: 367-376.
127. Milgrom, L. R., Hill, J. P. and Flitter, W. D.; Facile Aerial Oxidation of a Porphyrin. Part 13. Generation of Pi-Cation Radicals via acid addition to mesotetrakis(3,5-ditertbutyl-4-hydroxyphenyl)porphyrin and its two-electron oxidation product *Tetrahedron* 1993; **49**: 507-513.
128. Zhou, M. and Heinze, J.; Electropolymerization of Pyrrole and Electrochemical Study of Polypyrrole. 3. Nature of "Water Effect" in Acetonitrile. *J. Phys. Chem. B* 1999; **103**: 8451-8457.
129. Downard, A. J. and Pletcher, D.; A study of the conditions for the electrodeposition of polythiophene in acetonitrile. *J. Electroanal. Chem.* 1986; **206**: 147-152.
130. Downard, A. J. and Pletcher, D.; The influence of water on the electrodeposition of polypyrrole in acetonitrile. *J. Electroanal. Chem.* 1986; **206**: 139-145.

131. Sabouraud, G., Sadki, S. and Brodie, N.; The mechanisms of pyrrole electropolymerization. *Chem. Soc. Rev.* 2000; **29**: 283-293.
132. Morse, N. J., Rosseinsky, D. R., Mortimer, R. J. and Walton, D. J.; Electrochemical and spectroscopic studies of pyridine intervention in the electrooxidation of pyrrole. *J. Electroanal. Chem.* 1988; **255**: 119-141.
133. Rosseinsky, D. R., Morse, N. J., Slade, R. C. T., Hix, G. B., Mortimer, R. J. and Walton, D. J.; Mechanisms of the chemical and electrochemical polymerizations of pyrrole compared by product spectrometry and conductivity loss effected by pyridine inhibition or by over-oxidation. *Electrochim. Acta* 1991; **36**: 733-738.
134. Qian, R., Pei, Q. and Huang, Z.; The role of H⁺ ions in the electrochemical polymerization of pyrrole. *Makromolekulare Chemie* 1991; **192**: 1263-1273.
135. Zujovic, Z. D., Zhang, L., Bowmaker, G. A., Kilmartin, P. A. and Travas-Sejdic, J.; Self-Assembled, Nanostructured Aniline Oxidation Products: A Structural Investigation. *Macromol.* 2008; **41**: 3125-3135.
136. Wu, A., Kolla, H. and Manohar, S. K.; Chemical Synthesis of Highly Conducting Polypyrrole Nanofiber Film. *Macromolecules* 2005; **38**: 7873-7875.
137. Huang, H. and Kane, R. B.; A General Chemical Route to Polyaniline Nanofibres. *J. Am. Chem. Soc.* 2004; **126**: 851-855.
138. Huang, J. and Kaner, R. B.; Nanofiber formation in the chemical polymerization of aniline: a mechanistic study. *Angew. Chem. Int. Ed.* 2004; **43**: 5817-5821.
139. Udal'tsov, A. V. and Kazarin, L. A.; Stabilization of donor-acceptor complexes formed by associated porphyrins in thin films. *J. Photochem. Photobiol. A* 1996: 99-107.
140. Shimomura, E. T., Phillippi, M. A., Goff, H. M., Scholz, W. F. and Reed, C. A.; Infrared spectroscopy of oxidized metalloporphyrins: detection of a band diagnostic of porphyrin-centered oxidation. *J. Am. Chem. Soc.* 1981; **103**: 6778-6780.
141. Wheaton, G. A., Stoel, L. J., Stevens, N. B. and Frank, C. W.; Optical spectra of phenazine, 5,10-dihydrophenazine, and the phenazhydrins. *Appl. Spectrosc.* 1970; **24**: 339-343.
142. Stammer, C. and Taurins, A.; Infrared spectra of phenazines. *Spectrochim. Acta* 1963; **19**: 1625-1654.

143. Nalwa, H. S. *Handbook of Organic Conductive Molecules and Polymers*; John Wiley & Sons Ltd., 1997; Vol. 2; pp 1-10.
144. MacDiarmid, A. G., Chiang, J. C., Huang, W., Humphrey, B. D. and Somasiri, N. L. D.; Polyaniline: protonic acid doping to the metallic regime. *Mol. Cryst. Liq. Cryst.* 1985; **125**: 309-318.
145. Silvers, S. J. and Tulinsky, A.; The Crystal and Molecular Structure of Triclinic Tetraphenylporphyrin. *J. Am. Chem. Soc.* 1967; **89**: 3331-3337.
146. Wasbotten, I. H., Conradie, J. and Ghosh, A.; Electronic Absorption and Resonance Raman Signatures of Hyperporphyrins and Nonplanar Porphyrins. *J. Phys. Chem. B* 2003; **107**: 3613-3623.
147. Vitasovic, M., Gouterman, M. and Linschitz, H.; Calculations on the Origin of Hyperporphyrin Spectra in Sequentially Protonated meso-(Dimethylaminophenyl)porphyrins. *J. Porphyrins Phthalocyanines* 2001; **5**: 191-197.
148. Ojadi, E., Selzer, R. and Linschitz, H.; Properties of Porphyrin Dimers, Formed by Pairing Cationic and Anionic Porphyrins. *J. Am. Chem. Soc.* 1985; **107**: 7783-7784.
149. Traylor, T. G., Nolan, K. B. and Hildreth, R.; Polyvalent Porphyrins. Properties of Tetrakis(3,5-di-tert-butyl-4-hydroxyphenyl)porphyrin(1-P) and Its Fe(III) and Zn(II) Derivatives. *J. Am. Chem. Soc.* 1983; **105**: 6149-6151.
150. Andersson, A., Johansson, N., Broems, P., Yu, N., Lupo, D. and Salaneck, W. R.; Fluorine tin oxide as an alternative to indium tin oxide in polymer LEDs. *Adv. Mater.* 1998; **10**: 859-863.
151. Hagfeldt, A. and Grätzel, M.; Light-Induced Redox Reactions in Nanocrystalline Systems. *Chem. Rev.* 1995; **95**: 49-68.
152. Savenije, T. J., Moons, E., Boschloo, G. K., Goossens, A. and Schaafsma, T. J.; Photogeneration and transport of charge carriers in a porphyrin p/n heterojunction. *Physical Review B: Condensed Matter* 1997; **55**: 9685-9692.
153. Gregg, B. A., Fox, M. A. and Bard, A. J.; Photovoltaic Effect in Symmetrical Cells of a Liquid Crystal Porphyrin. *J. Phys. Chem.* 1990; **94**: 1586-1598.
154. Savenije, T. J., Koehorst, R. B. M. and Schaafsma, T. J.; Photoinduced Unidirectional Electron Transfer in a Porphyrin Heterojunction. *Chem. Phys. Lett.* 1995; **244**: 363-370.

155. Savenije, T. J. and Goossens, A.; Hole transport in porphyrin thin films. *Phys. Rev. B: Condens. Matter Mater. Phys.* 2001; **64**: 115323/115321-115323/115329.
156. Hummelen, J. C., Knight, B. W., LePeq, F., Wudl, F., Yao, J. and Wilkins, C. L.; Preparation and Characterization of Fulleroid and Methanofullerene Derivatives. *J. Org. Chem.* 1995; **60**: 532-538.
157. Theander, M., Inganaes, O., Mammo, W., Olinga, T., Svensson, M. and Andersson, M. R.; Photophysics of Substituted Polythiophenes. *J. Phys. Chem. B* 1999; **103**: 7771-7780.
158. Cook, S., Ohkita, H., Kim, Y., Benson-Smith, J. J., Bradley, D. D. C. and Durrant, J. R.; A photophysical study of PCBM thin films. *Chem. Phys. Lett.* 2007; **445**: 276-280.
159. Campos, L. M., Mozer, A. J., Guenes, S., Winder, C., Neugebauer, H., Sariciftci, N. S., Thompson, B. C., Reeves, B. D., Grenier, C. R. G. and Reynolds, J. R.; Photovoltaic activity of a PolyProDOT derivative in a bulk heterojunction solar cell. *Sol. Ener. Mater. Sol. Cells* 2006; **90**: 3531-3546.
160. Wamser, C. C., Bard, R. R., Senthilathipan, V., Anderson, V. C., Yates, J. A., Lonsdale, H. K., Rayfield, G. W., Friesen, D. T., Lorenz, D. A., Stangle, G. C., van Eikeren, P., Baer, D. R., Ransdell, R. A., Golbeck, J. H., Babcock, W. C., Sandberg, J. J. and Clarke, S. E.; Synthesis and Photoactivity of Chemically Asymmetric Polymeric Porphyrin Films Made by Interfacial Polymerization. *J. Am. Chem. Soc.* 1989; **111**: 8485-8491.
161. Drew, C., Liu, X., Ziegler, D., Wang, X., Bruno, F. F., Whitten, J., Samuelson, L. A. and Kumar, J.; Metal Oxide-Coated Polymer Nanofibers. *Nano Letters* 2003; **3**: 143-147.
162. Yamabi, S. and Imai, H.; Fabrication of Rutile TiO₂ Foils with High Specific Surface Area via Heterogeneous Nucleation in Aqueous Solutions. *Chem. Lett.* 2001; **3**: 220-221.
163. Yamabi, S. and Imai, H.; Crystal Phase Control for Titanium Dioxide Films by Direct Deposition in Aqueous Solutions. *Chem. Mater.* 2002; **14**: 609-614.
164. Stathatos, E., Lianos, P., Zakeeruddin, S. M., Liska, P. and Graetzel, M.; A Quasi-Solid-State Dye-Sensitized Solar Cell Based on a Sol-Gel Nanocomposite Electrolyte Containing Ionic Liquid. *Chemistry of Materials* 2003; **15**: 1825-1829.

165. Mozer, A. J., Sariciftci, N. S., Lutsen, L., Vanderzande, D., Osterbacka, R., Westerling, M. and Juska, G.; Charge transport and recombination in bulk heterojunction solar cells studied by the photoinduced charge extraction in linearly increasing voltage technique. *Appl. Phys. Lett.* 2005; **86**: 112104/112101-112104/112103.
166. Lungenschmied, C., Dennler, G., Neugebauer, H., Sariciftci, S. N., Glatthaar, M., Meyer, T. and Meyer, A.; Flexible, long-lived, large-area, organic solar cells. *Sol. Ener. Mater. Sol. Cells* 2007; **91**: 379-384.